Application of Novel Nanoscale Materials and Advanced Electrochemical Techniques in Heterogeneous Catalysis and Fabrication of Combinatorial Material Libraries by Bipolar Electrodeposition

by

Sridevi Ramakrishnan

A dissertation submitted to the Graduate Faculty of
Auburn University
in partial fulfillment of the
requirements for the Degree of
Doctor of Philosophy

Auburn, Alabama
December 12, 2011

Key words: Polyoxometalates, Fuel cells, Carbon nanotubes, Bipolar Electrodeposition.

Approved by

Curtis Shannon, Chair, Professor of Chemistry and Biochemistry
Vince Cammarata, Associate Professor of Chemistry and Biochemistry
Jeffrey Fergus, Professor of Materials Research and Education Center
Wei Zhan, Assistant Professor of Chemistry and Biochemistry

Abstract

The advancements in the electrochemical technologies combined with the introduction of novel materials makes our lives a lot better. This work has two major divisions: (1) development of better electrocatalysts for fuel cells and (2) application of bipolar technique in combinatorial material library synthesis.

Chapters 1 gives a brief introduction of polyoxometalates, an inorganic molecule capable of conducting multi-electron, proton and oxygen and so used as electrocatalyst for many redox reaction. It also gives a short account on carbon nanotubes (CNTs), an excellent supporting material for electrocatalysts, with high surface area, high electrical conductance and excellent mechanical strength. Finally it deals with the methods to establish lateral potential gradient on a conductive surface. The methods mainly include bipotentiostat and bipolar technique. Lateral potential gradient helps to make the combinatorial materials library on a single substrate.

Chapter 2 deals with synthesis of Dawson and transition metal substituted Dawson type polyoxometalates, their characterization, redox properties and electrocatalytic activity towards oxygen reduction reaction (ORR). Results show that all these POMs are hydrolytically stable at low pH and electrocatalytically active towards ORR in 0.1M perchloric acid medium. The Dawson compounds follow the following trend in ORR electrocatalytic activity: Dawson , Co-Dawson < Ru-Dawson < Fe-Dawson.

Chapter 3 deals with bimetallic synergy between transition metal substituted Dawson type POMs and noble metals electrodes such as gold, palladium and platinum for

ORR. In this case the transition metal in POM helps to cleave the O-O bond in dioxygen and the noble metal surface is good at reducing the cleaved oxygen atoms to water. The bond strength between the transition metal substituted in Dawson and oxygen atom should be high enough to cleave O=O bond of dioxygen and at the same time it should allow the transfer of cleaved oxygen atom to the noble metal surface. So, the ORR potential shift on gold electrode with transition metal substituted POM taken in 0.1M perchloric acid medium depends on the free energy of formation of bulk metal oxide of corresponding substituted transition metal in the POM. The maximum ORR potential shift obtained was about +200 mV compared to pure gold surface. It occurred with 0.2 mM Ru-Dawson in 0.1M perchloric acid medium. With palladium electrode Dawson and Fe-Dawson gave a negative ORR shift. Ru- and Co- Dawson gave positive ORR potential shift. The maximum ORR potential shift obtained on Pd was +100 mV with 0.2 μM Co-Dawson. On platinum surface all Dawson type POMs except Co-Dawson gave negative potential shift due to surface poisoning. Co-Dawson at 0.2 μM gave a positive shift of about +25 mV compared to pure Pt. Less adsorbing Keggin type POM with Co substitution gave a maximum shift of about +54mV on Pt surface which is comparable with other bimetallic electrocatalysts.

Chapter 4 deals with the ORR electrocatalytic activity of oxidized MWNT and oxidized MWNT-Co-Dawson adduct prepared by sonication method. Compared to glassy carbon, oxidized MWNT gave a 200 mV positive shift in ORR $E_{1/2}$ potential. Co-Dawson treated oxidized MWNT gave another 200mV positive shift. Though the absence of Co-Dawson redox peaks in the Co-Dawson treated oxidized MWNT under deoxygenated condition indicates the decomposition of Co-Dawson during the process of sonication

with oxidized MWNT, due to the significant positive shift in ORR potential, we further studied the kinetics of ORR on the oxidized MWNT-Co-Dawson adduct. 12 hr sonication with Co-Dawson has doubled the ORR kinetic current of the oxidized MWNT.

Chapter 5 deals with the formation and characterization of one-dimensional chemical composition gradients of CdS on Au surfaces using bipolar electrodeposition. When an external electric field is applied across an electrically floating Au electrode immersed in a bipolar electrochemical cell, a position-dependent interfacial potential difference is generated along the length of the Au. This potential gradient can be used to induce variations of chemical composition within thin films electrodeposited onto the Au bipolar electrode (BPE). Thin films formed by bipolar electrodeposition represent continuous one-dimensional solid-state material libraries and were screened using resonance Raman microscopy and Auger electron spectroscopy. As predicted from simple thermodynamic considerations, we observed three distinct deposition zones scanning from the cathodic pole to the midpoint of the BPE: (i) CdS+Cd, (ii) stoichiometric CdS, and (iii) elemental S. Bipolar electrodeposition can be used to generate material libraries rapidly and without direct electrical contact to the substrate using extremely simple instrumentation.

Chapter 6 gives the summary of this research work and a few directions for further studies.

Acknowledgements

I would like to express my sincere gratitude to my advisor Dr Curtis Shannon for his continuous guidance, constant motivation and generous support. I greatly appreciate his patient and persistent trials on the research activities. I would like to appreciate all my committee members Dr Vince Cammarata, Dr Jeffrey Fergus, Dr Wei Zhan for their valuable suggestions that helped my research work. I would like to thank Dr Minseo Park for being the outside reader for my dissertation.

I would like to thank Dr. Thomas Albrecht-Schmitt and his group for helping in powder XRD characterization and Mr Tom Carrington for helping with other analytical techniques. I also thank all the graduate students and faculty members who helped me in the course of my Ph.D studies.

I give my special thanks to my lab members Dr Anand Sankarraj, Dr Tsunghsueh Wu, Dr Junxua Xin, Dr. Hongxia Zhang, Dr Chaokang Gu, Mrs Weiping Li, Ms Rajakumari Ramaswamy, Mrs Sanghapi Ndzesse Sanghapi, Mrs Tanyu Wang and Ms Yajiao Yu for their support and useful discussion.

I would like to thank the ever sweet staff of the Chemistry and Biochemistry department for their great service.

I would like to thank all my friends and mentors who supported me during the course my academic life. I would like to give my special thanks to my parents and other family members for their great support and encouragement in my academic life.

Table of Contents

List of Tables

List of Figures

Chapter 1

INTRODUCTION

1.1 Beauty of Electrochemistry:

The beauty of electrochemistry is reflected in its theoretical simplicity and practical application in that it solves so many real-world problems. The development of electrochemistry began in the 18th and19th centuries. Michael Faraday and John Daniell gave impetus to its growth by their fundamental studies[1]. Now, we are enjoying the ripening period of well established electrochemical science and technology. Various applications of electrochemical technology include power sources (batteries and fuel cells), electrosynthesis of aesthetic and protective coating, corrosion prevention, electrochemical sensors, purification of materials, and the fabrication of micro or nanostructures for electronic application. Major advantages of electrochemical technologies are cost effective and eco-friendliness. Combined with introduction of suitable materials and techniques, contribution of electrochemical technology has a great impact on the growth of human community.

My research focus is on

- Designing better electrocatalysts for fuel cell applications and
- Preparation of combinatorial material library using bipolar electrochemistry.

1.2 Designing Better Catalysts for Fuel Cell Applications:

Fuel cell technology is one of the promising energy sources that can solve the problems of depleting fossil fuels and global warming[2]. The focus of this study is on proton exchange membrane fuel cell (PEMFC) which can be operated at low temperatures such as <90° C and can be used for the vehicles[3]. In a PEMFC, anode and cathode are separated by a proton exchange membrane and connected to leads using an external circuit. The anode compartment is fed by hydrogen gas and the cathode compartment is fed by air or oxygen gas. The electrode reactions are

Anode half-cell: $H_2 \longrightarrow 2H^+ + 2e^-$ $E^0 = 0.00V$ vs NHE

Cathode half-cell: $O_2 + 4H^+ + 4e^- \longrightarrow H_2O$ $E^0 = 1.23V$ vs NHE

Overall reaction: $H_2 + ½\ O_2 \longrightarrow H_2O$ $E^0_{cell} = 1.23V$

Protons are conducted from anode to cathode by the proton exchange membrane (PEM) and the electron flow from anode to cathode through external circuit under the potential difference supplies power to the load.

In any electron transfer reaction, whether chemical or electrochemical, the reactants have to cross the activation energy barrier for the reaction to complete. Different ways of helping reactants to cross the activation energy barrier are supplying heat energy or changing the chemical environment of the reactants or combining both[4,5]. High heat is neither cost effective nor compatible in many cases. Under these situations changing the chemical environment of the reactants using a catalyst is useful. A catalyst increases the reaction rate without undergoing any change. Catalytic reactions can be of two types: homogeneous and heterogeneous[5]. In homogeneous catalysis, both the reactant and the catalyst are in single phase. In heterogeneous, the reactant and the catalyst are in different

phases. Since in a fuel cell electrochemical half reactions occur at the interface of electrode(e^- conductor) and electrolyte (ion conductor), the catalyst is present on the electrode surface and a heterogeneous catalytic reaction occurs on both anode and cathode. Pt nanoparticles immobilized on Vulcan® carbon have been widely used as an electrocatalyst in fuel cells for both anode and cathode.

However, the high cost of Pt and the insufficient kinetics of cathode reaction on Pt surface[6,7], have driven scientists to find ways to improve the catalytic efficiency of the Pt catalyst or to make an alternate catalyst for the cathode reaction, i.e, the oxygen reduction reaction (ORR). Though the ORR elementary steps are not well established, two major steps are proposed here[6]. The first is breakage of the O-O bond, followed by reduction of the 'O' atom to produce water. Bimetallic catalysts have been introduced by many people in which the base metal does the O-O bond breaking and the noble metal reduces 'O' to water. In bimetallic catalysts, the base metal can dissolve in the electrolyte. To avoid this issue, the base metal has to be held in a stable skeleton.

Polyoxometalates (POMs) are a new class of compounds which have many suitable properties for acting as a catalyst. When these POMs are substituted with transition metals and adsorbed on the surface of a noble metal, they make the ORR process facile. They act as a stable skeleton in which the transition metal atoms can be held. For the purposes of this study, we also tried to immobilize Co-substituted POM (Co-POM) on multi walled carbon nanotubes (MWNT) and tested its ORR catalytic property.

The subsequent sections describe POM structure and its redox and electrocatalytic properties as well as the development in the field of carbon nanotubes (CNT) and their application in electrocatalysis.

1.2.1 Introduction to Polyoxometalates (POMs):

POMs are early transition metal oxygen anion clusters. The history of our knowledge of them goes back to the first report by Berzelius in 1826[8]. Oxo anions of metals from Groups 5 and 6 such as W, Mo, V, and Cr cluster together when the pH is lowered and form the POMs[9,10]. If a foreign element is included in the POM structure, it is called heteropolyanion (HPA). These HPA have tunable redox properties and structural stability upon redox activity[11]. This makes them suitable for electrocatalysis. Though there are a variety of HPA structures, the most studied structures for electrocatalysis are Keggin and Wells-Dawson named after the scientists who revealed their crystal structures.

(i) Structure of Keggin and Wells-Dawson Type HPAs:

Keggin has a highly symmetrical structure as shown in Figure 1.1[12]. Its general formula is $XM_{12}O_{40}^{n-}$. "X" represents heteroatom and a range of non-metallic or metallic elements such as Si, P, Ge, Zn, Fe, and Cu have been found to act as heteroatoms[11]. P, Si, Ge, and As are the most commonly occurring hetero atoms. "M" represents addenda atoms. Metals from Groups 5 and 6 such as W, Mo, V and Cr have the ability to act as addenda atoms. As shown in Figure 1.1, the Keggin type HPA has a central XO_4 tetrahedron surrounded by four M_3O_{13} triads. Each oxygen atom of the central tetrahedron is associated with an M_3O_{13} unit. Each octahedron represents a metal atom in the center of the octahedron, and each corner represents an oxygen atom in the structure. The oxygen atoms can be categorized as terminal, edge sharing and corner sharing according to their position in the HPA structure. Also, these HPAs have structural isomers depending upon the rotation of the M_3O_{13} unit about the central tetrahedron unit.

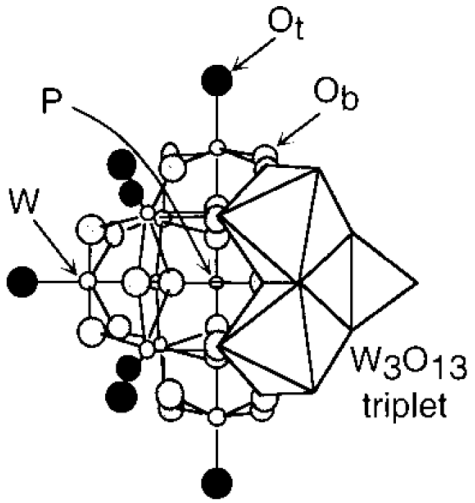

Figure 1.1 Structure of Keggin HPA: $PW_{12}O_{40}^{3-}$.

(Reprinted with permission from Ref . 12

Copyright © 1998, American Chemical Society)

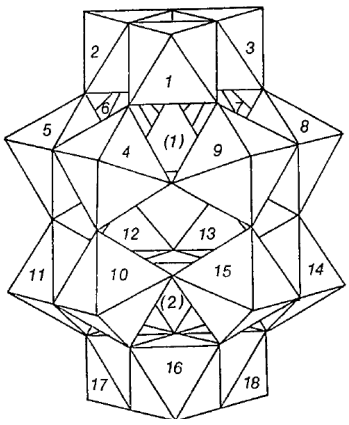

Figure 1.2 Structure of Wells-Dawson HPA: $X_2M_{18}O_{62}^{n-}$.

(Reprinted with permission from Contant, R.; Abbessi, M.; Canny, J. *Inorg. Chem.* **1997**, *36*, 4961-4967.

Copyright © 1997, American Chemical Society)

A Wells-Dawson[13] HPA has a general formula of $X_2M_{18}O_{62}^{n-}$ where "X" is a heteroatom and M is an addenda atom similar to the Keggin type. Its structure consists of two heteroatoms stacked one on top of the other, and each end is composed of an M_3O_{13} cap with two six-metal belts circling the molecule as shown in Figure 1.2.

Among the range of Keggin and Wells-Dawson type HPAs, phosphotungstates, silicotungstates, phosphomolybdates and silicomolybdates are considered good electrocatalysts due to their high stability and ease of preparation[11].

When the pH of the HPA aqueous solution is raised to a defined level, one or more MO units are removed from the HPA cluster and the resulting structure is called a lacunary HPA. These vacant sites can be filled with transition metals to get transition metal substituted HPAs (TM-substituted HPAs)[11]. The sixth coordinate of the transition metal is provided by the solvent molecule. Substitution of the transition metal provides a method to combine the property of a specific transition metal with the favorable properties of HPAs such as high structural stability and multiple electron transferability. TM-substituted HPAs can be considered stable inorganic analogues of organic metal complexes which are easily susceptible to decomposition due to oxidation of the organic structure.

(ii) Redox Properties of HPAs:

HPAs undergo reversible one or two electron reduction to give 'heteropoly blue'[11]. Further irreversible multiple reduction leads to decomposition of the HPAs. The electron acceptors are the addenda atoms, and the accepted electrons are delocalized among the addenda atoms if they all are identical. Reduction of HPAs makes them more negatively charged and increases the basicity of the reduced HPAs. So, at low pH the HPA reduction is accompanied by protonation and, thus, HPA redox activity is highly pH dependent.

Figure 1.3 shows the electrochemical behavior of HPAs with respect to pH. At low pH series of $2e^-$, transfer occurs accompanied by protonation. At high pH, the $2e^-$ transfer splits into two $1e^-$ transfers without any protonation. At low pH, the redox potential varies with pH at a slope of ~59mV/pH characteristics of equal number of electron and proton transfer.

The redox potential is also dependent on the type of addenda atom and the charge on the heteroatom[14]. Heteropoly molybdates undergo reduction at more negative potentials than the heteropoly tungstates. The valence of the heteroatom determines the charge on the HPAs. The redox potential decreases to more negative potential with increase in the HPA charge. Figure 1.4 shows the dependence of the first e^- transfer potential on the charge of the Keggin type HPA.

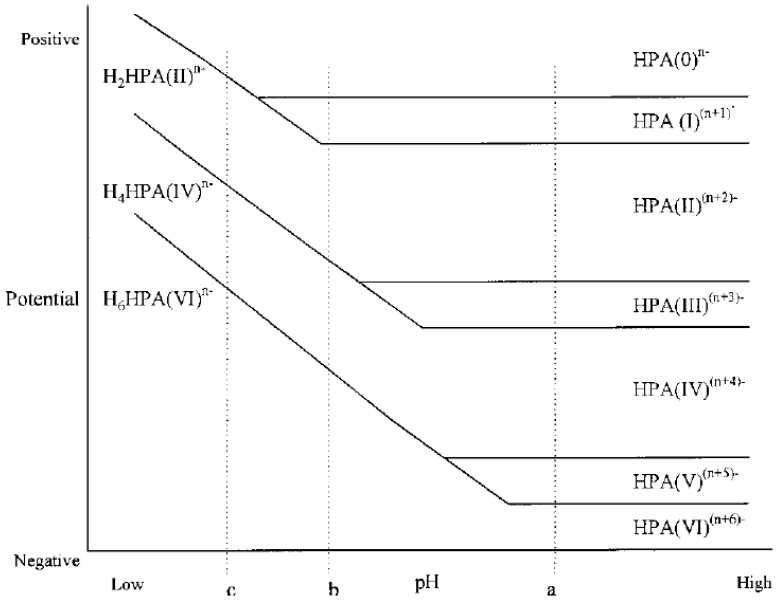

Figure 1.3 Electrochemical behavior of HPAs with respect to pH.

(Reprinted with permission from Ref . 11

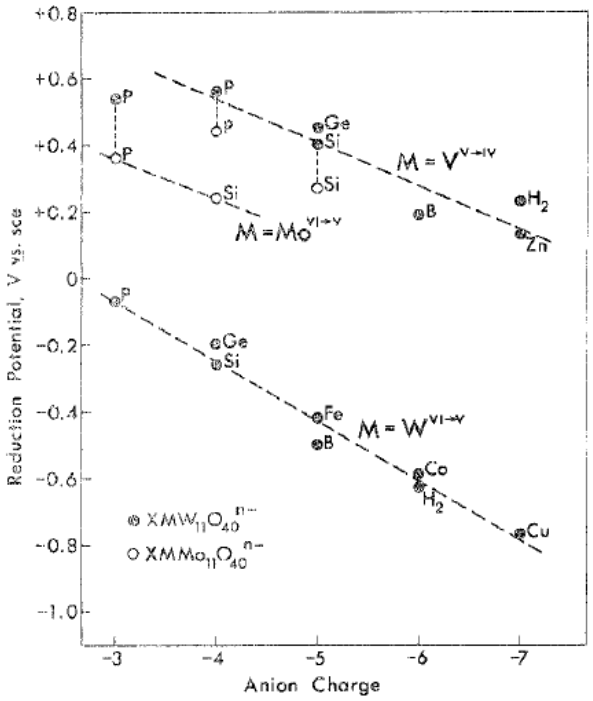

Figure 1.4 Dependence of reduction potential on the anion charge of Keggin type HPA. (Reprinted with permission from Ref . 14

Copyright © 1975, American Chemical Society)

In my studies, Keggin and Wells-Dawson type phosphotungstates were used as co-catalysts for an oxygen reduction reaction (ORR) on noble metal electrodes under low pH a condition which exists in proton exchange membrane fuel cells (PEMFC). Facile preparation of phosphotungstates, their structural stability at low pH and their higher positive redox potential compared to most other HPAs[11] qualify them suitable for ORR catalyst.

The following scheme represents the redox activity of Keggin type phosphotungstate at low pH[11]:

$$\alpha\text{-}PW_{12}O_{40}^{3-} + e^- = \alpha\text{-}PW_{12}O_{40}^{4-}$$

$$\alpha\text{-}PW_{12}O_{40}^{4-} + e^- = \alpha\text{-}PW_{12}O_{40}^{5-}$$

$$\alpha\text{-}PW_{12}O_{40}^{5-} + 2\,e^- + H^+ = \alpha\text{-}HPW_{12}O_{40}^{6-}$$
$$0 < pH < 3$$

Keggin phosphotungstates undergo reversible two $1e^-$ reductions followed by one $2e^-$ reduction at low pH.

The following scheme represents the redox activity of Wells-Dawson type phosphotungstates at low pH[11]:

$$P_2W_{18}O_{62}^{6-} + e^- = P_2W_{18}O_{62}^{7-}$$

$$P_2W_{18}O_{62}^{7-} + e^- = P_2W_{18}O_{62}^{8-}$$

$$P_2W_{18}O_{62}^{8-} + 2e^- + 2H^+ = H_2P_2W_{18}O_{62}^{8-}$$

$$H_2P_2W_{18}O_{62}^{8-} + 2e^- + 2H^+ = H_2P_2W_{18}O_{62}^{8-}$$
$$0 < pH < 3$$

Wells-Dawson type phosphotungstates undergo reversible two $1e^-$ reductions followed by two $2e^-$ reductions at low pH. Further irreversible reduction leads to decomposition of the molecule.

In TM-substituted HPAs, the transition metal also undergoes redox activity along with the ligated HPA structure[11].

(iii) Electrocatalytic Properties of HPAs:

Certain unique properties of HPAs such as high hydrolytic and thermal stability of most of their redox states, tunable redox potentials, flexibility to substitute desired transition metals in their structure, the possibility of multiple electron transfer make them suitable for electrocatalysis[11]. Especially the ability to undergo multiple electron transfer

is very important for catalyzing reactions that involve multiple electron transfer such as nitrate reduction, oxygen reduction, etc.

HPAs act as mediators for the electron transfer between the electrode material and the reactants[11]. Scheme 1.1 represents the redox mediating property of the HPAs.

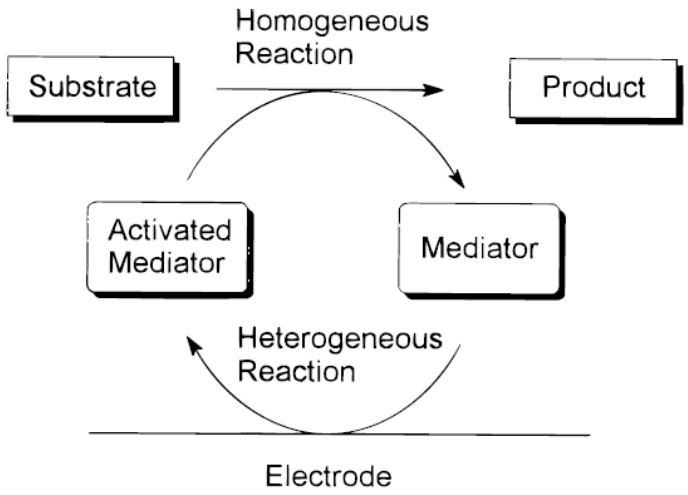

Scheme 1.1 Redox mediating property of the HPAs

(Reprinted with permission from Ref . 11

Copyright © 1998, American Chemical Society)

For example, in electrocatalyzing a reduction reaction, the HPA accepts electrons from the electrode and becomes an activated reduced form of HPA. The activated reduced HPA donates the accepted electron to the reactant or substrate in order to form the product. Now the activated reduced form HPA has been oxidized to its original state and is ready for the next catalytic cycle. In the cases where the reactant has poor interaction with the electrode material, redox mediating action of the HPA increases the reaction rate.

Initially, homogeneously dissolved HPAs in solution were used as redox mediators between the electrode and the reactant[11]. Later, several immobilization techniques were developed to concentrate the HPA on the electrode surface[11]. It improves the contact between the electrode and the HPAs and thus the turn over frequency of the reaction is increased.

So far HPAs have been applied for electrocatalytic reduction of nitrate, chlorate, bromate, oxygen, and peroxide[11]. These all are involved multiple electron transfers.

Chapter 2 describes the synthesis, characterization and the electrocatalytic properties of the Dawson type phosphotungstate and its transition metal substituted compounds on ORR and Chapter 3 describes the synergetic effect of TM-substituted HPAs with noble metal surface (bimetallic effect) on ORR.

1.2.2 Introduction to Carbon Nanotubes (CNT):

Immobilizing the electrocatalyst on a high surface area conducting material provides several advantages over simply keeping the electrocatalyst in solution phase. Immobilization of the electrocatalyst on the support ensures a good electrical contact between the electrocatalyst and the electrode material which increases the frequency of electron transfer between the reactant and the electrode material via the electrocatalyst. Carbon nanotubes have been used as supporting materials due to their desirable properties such as high surface area, high electrical conductivity, significant mechanical strength, required chemical inertness, being insoluble in many solvents, flexibility to functionalize its surface.

CNTs were first observed by Wiles and Abrahamson in 1978 as a thick mat of fine fiber on a graphite anode following low current arc operation in nitrogen at

atmospheric pressure[15]. These fibers had a diameter of 4 to 100 nm and a length of 15 microns. In 1991, the Japanese electron microscopist Sumio Iijima rediscovered these fibers, and they are now called CNTs. CNTs are primarily divided into two categories: single walled nanotubes (SWNTs) and multi-walled nanotubes (MWNTs)[16].

A SWNT is a tubular structure of a rolled up graphene sheet along any of the three axes as shown in Figure 1.5 (A). The rolled up structures along various axes are shown in Figure 1.5 (B,C,D). The chirality of the SWNT depends upon the axis along which the graphene sheet was rolled up. The chirality and the diameter of the nanotube determine its conductivity. Figure 1.5 (D) shows the structure of a MWNT. It has a few layers of concentric carbon rolls as opposed to SWNTs. The diameter of a SWNT is typically about 1nm and the smallest reported diameter is 0.4nm. A MWNT has a diameter of about 2 to 100 nm. A SWNT can be considered a single macromolecule whereas a MWNT can be viewed as a mesoscale graphite system[16]. The ends of the CNTs look like hemispheres. Inclusion of pentagonal bonding structure between five carbon atoms among the hexagonal network of the grapheme structure leads to the formation of the hemispherical structure and leads to closing of the CNT during its growth.

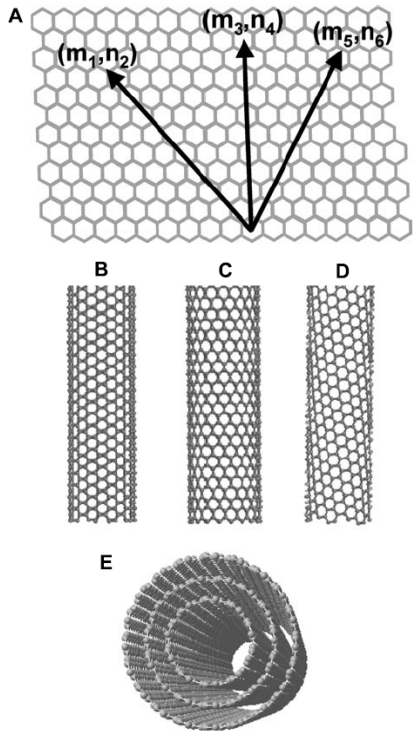

Figure 1.5 Schematic of the honeycomb structure of a graphene sheet (A). SWNTs can be formed by folding the sheet along the shown lattice vectors leading to armchair (B), zigzag (C), and chiral (D) tubes, respectively. The graphene sheets rolled up into concentric cylinders form MWNTs (E).

(Reprinted from reference 16 with permission from Springer)

(i) Methods of CNT Preparation[16]:

Commonly used methods for the CNT preparation are arc-discharge method, laser ablation method, and chemical vapor deposition.

The arc-discharge method is the first used method to produce CNTs. In this method, applying a dc arc voltage between two graphite electrodes separated by a one millimeter gap in an inert atmosphere under low pressure leads to evaporation at the anode and deposits some carbon material at the cathode. The deposit at the cathode

contains MWNTs. The drawback of this method is removal of non-nanotube carbon material and metal nanocluster is more expensive than production of CNTs.

Laser ablation method is especially well-suited for producing SWMTs. In this method, the carbon target is coated with a metal catalyst inside a quartz furnace and a laser beam of CO_2 is irradiated on the target. The carbon target vaporizes into carbon and grows into SWNTs on the metal nanocluster. The Ar carrier gas takes away the SWNTs and collects them in a separate container. The advantage of this method is that it produces high quality SWNTs. However, this method is expensive as it uses a laser.

Chemical vapour deposition (CVD) is a widely used method for large scale production of both MWNTs and SWNTs. The first two methods have no control over location and alignment during CNT growth. CVD, on the other hand, avoids this problem. It used metal or metal oxide or alloy nanocluster aligned on a substrate kept at 500-1000°C as "seed" to initialize the growth of the CNTs. Hydrocarbon vapour such as methane is used as the carbon source, and it thermally decomposes to carbon at high temperature, then grows into CNTs on the surface of metal nanoclusters. Type of hydrocarbon, type of catalyst and growth temperature are the key parameters in this technique that controls the CNT growth.

Ni, Fe, Co, CoMo, and FeO_x are the most used catalysts. The size of the nanotubes can be controlled by the size of the nanocluster used. Cheung, et al. have used various size Fe nanoclusters to produce CNTs with various diameters[17]. Figure 1.6 shows the growth of the CNT on the metal cluster and the size dependence of CNT on the size of the metal nanocluster.

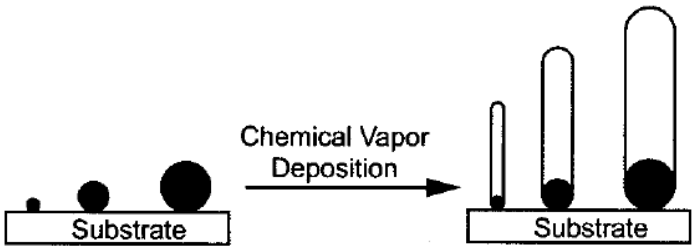

Figure 1.6 Schematic depicting the use of different diameter iron nanocluster catalysts for the controlled diameter synthesis of carbon nanotubes.

(Reprinted with permission from Ref . 17

(ii) Characterization Techniques for As-prepared and Modified CNTs:

The electronic and mechanical properties of the as-prepared and purified CNTs can be evaluated using morphological and structural characterization techniques. The three-dimensional morphology of CNTs deposited on a flat conducting substrate such as HOPG[18] or Au[19] can be obtained from a scanning tunneling microscopy (STM) image. Figure 1.7 shows the STM image of a CNT on a flat HOPG substrate.

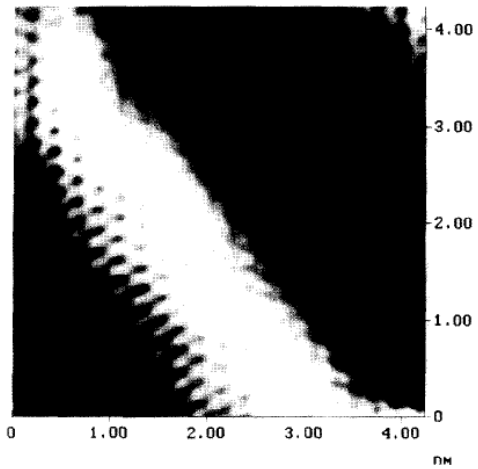

Figure 1.7 Atomic resolution STM image of a carbon tube with a diameter of 35 Å on a flat HOPG substrate.

(Reprinted from reference 18 with permission from Elsevier)

Gommes, et al. have obtained the outer and inner radii of MWNTs by transmission electron microscopy (TEM) imaging. They have also calculated the linear electron absorption coefficient of CNTs[20] using the same method of TEM imaging. Figure 1.8 shows a typical TEM image of MWNTs.

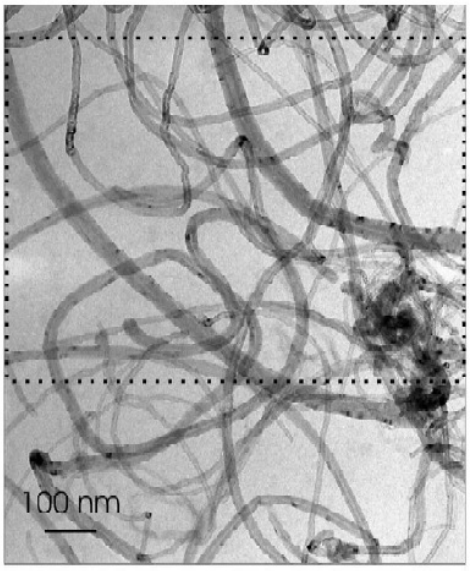

Figure 1.8 Typical TEM image of MWNTs.

(Reprinted from reference 20 with permission from Elsevier)

Infrared spectroscopy is helpful for determining impurities remaining from synthesis or molecules capped on the CNT surface. This technique can also be used to study the structural modification and nature of compounds added to the CNTs[21]. Figure 1.9 shows the infrared transmission spectrum of unmodified MWNT(a), carboxylated MWNT(b), 2,9,16,23-tetra amino manganese phthalocyanine (TAMnPc) modified carboxylated MWNT(c) and TAMnPc (d) for comparision.

The band at 3419 cm^{-1} for unmodified MWNT corresponds to O–H stretching from the carboxyl and hydroxyl attached to the open ends of MWNT produced during purification in refluxing nitric acid. Oxidation treatment in the H_2SO_4/HNO_3 (3:1 v/v) mixture provided –COOH groups terminated MWNT and so it leads to appearance of bands at 3409, 1708 and 1200 cm^{-1}, corresponding to O–H stretching, C=O stretching in carboxyl and C–O stretching in carboxylic and phenolic groups respectively. When

carboxyl-terminated MWCNT were further reacted with TAMnPc, the C=O stretching band from –COOH group at 1708 cm^{-1} disappeared and the C=O stretching from –CONH– group at 1629 cm^{-1} appeared. The new peaks were at 1598, 1124, 1018 and 756 cm^{-1}, which were characteristics of manganese phthalocyanine. Two broad peaks around 3425 and 3342 cm^{-1}, correspondeding to the dissociation of N–H stretching band from TAMnPc, disappeared in the spectra of MWCNT–TAMnPc. These results indicate that TAMnPc had been attached onto the MWCNT successfully. Thus Infrared spectroscopy is an excellent tool for monitoring the structural and chemical modification done on CNTs.

Infrared spectroscopy can also be used to study the catalytic properties of CNTs[22].

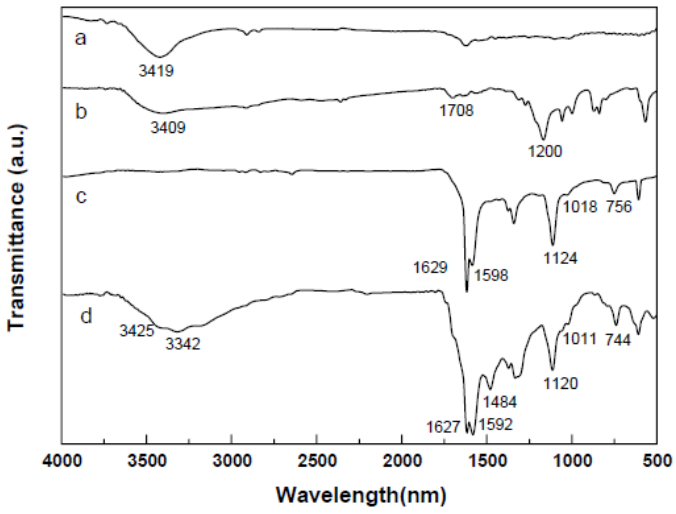

Figure 1.9 FTIR spectra of (a) MWCNT, (b) MWCNT–COOH, (c) MWCNT–TAMnPc, and (d) TAMnPc.

(Reprinted from reference 21 with permission from Elsevier)

CNTs are Raman active and this technique is one of the most powerful tools for characterization of CNTs since it doesn't need sample preparation and is nondestructive. Metallic and semiconductor SWNTs exhibit different Raman line shapes. This allows the two types to be distinguished[23]. SWNTs have three main Raman bands- (1) radial breathing mode (RBM) (Figure 1.10 (a)) appearing between 120 cm^{-1} and 250 cm^{-1} for SWNTs having diameter between 1nm and 2nm. (2) Tangential modes (G band) at around 1580 cm^{-1} and (3) the disorder induced D band at around 1300 cm^{-1}.

The G-band splits into two sub-bands: G^+ and G^-. G^+ corresponds to the atomic displacements along the tube axis, and G^- corresponds to the atomic displacement along the circumferential direction as shown in Figure 1.10 (b).

The lineshape of the G^- band distinguishes the metallic and semiconducting SWNTs. As shown in Figure 1.11, for semiconducting SWNTs the lineshape is sharp and it is characterized by Lorentzian, but for metallic SWNTs the lineshape is broad and asymmetric and it is characterized by Breit–Wigner–Fano (BWF). The line broadening is considered to be due to the presence of free electrons in the metallic SWNTs.

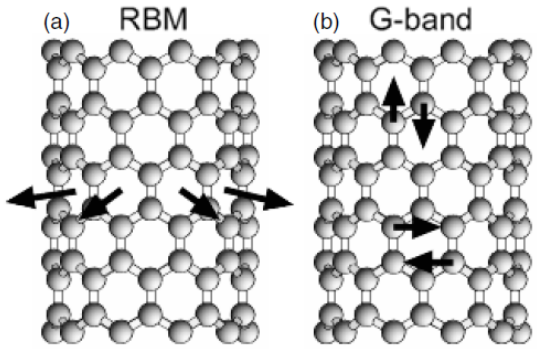

Figure 1.10 Schematic representation of atomic vibrations for (a) the RBM and (b) the G band modes of SWNTs.

(Reprinted from reference 23 with permission from Institute of Physics Publishing Ltd.)

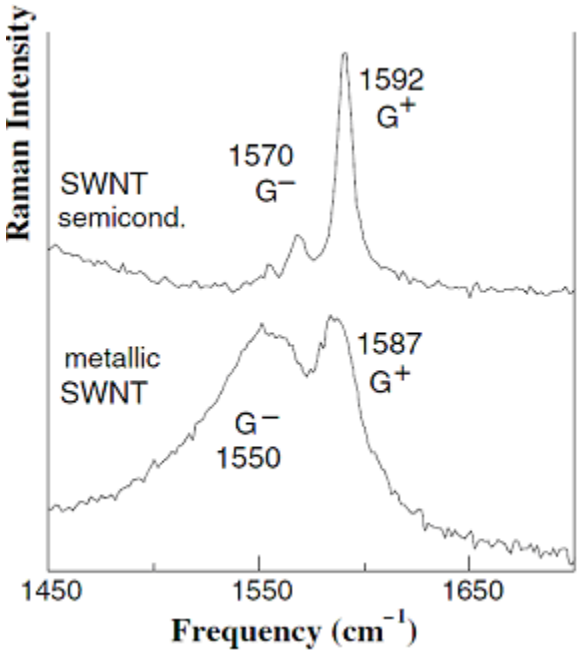

Figure 1.11 G-band lineshape of semiconducting and metallic SWNTs.

(Reprinted from reference 23 with permission from Institute of Physics Publishing Ltd.)

Elemental analysis on CNTs can be done by calibrated energy dispersive X-ray (EDX)[24].

(iii) Applications of CNTs:

CNTs have been applied as electrode materials in the field of sensors and electrocatalysis, hydrogen storage materials, conductive materials, strengthen materials, tips in scanning probe microscopy, functional materials in emission devices, supercapacitors, nanoelectronic devices, and field-effect transistors.

CNTs have been used as supporting material for metal nanoparticles, biomacromolecules, and other functional materials in the field of sensors and

electrocatalysis. Here, the purified CNTs were modified by the active materials through chemical or physical means. As the first step, the CNT side wall or end carbon atoms were oxidized to carboxylate functional groups and then further modification was done. There were a variety of oxidizing processes along with functionalization of the CNTs described in the literature.

Kim, et al. have prepared a colloidally stable gold nanoparticles-functionalized MWNTs by means of electrostatic interaction among the negatively charged MWNTs, positively charged gold nanoparticles, and a bilayer of polyelectrolytes sandwiched between the MWNT and the gold nanoparticle layers[25].

Catalase has also been adsorbed on MWNT and has been used for ORR and peroxide reduction. The K_m value for peroxide reduction was 1.7mM, indicating that the catalase MWNTs-modified GC electrode exhibits a higher affinity for hydrogen peroxide[26].

Karina Cuentas-Gallegos, et al. have attached $Cs_xPMo_{12}O_{40}$ on the walls of oxidized surfaces of MWNTs through covalent bonds[27]. MWNT surface oxidation was carried out by acid treatment in one of the following solutions: 2.5 M HNO_3, 2.5 M HNO_3 + 0.5 M H_2SO_4, and 2.5 M H_2SO_4. These MWNT-POM hybrid structures have scope in finding applications in nanoelectronic devices and optical applications.

Song, et al. have functionalized negatively charged surface oxidized CNT with negatively charged Polyoxometalates (POMs) using positively charged polyelectrolyte poly (diallyldimethylammonium chloride) (PDDA) by electrostatic force[28]. They have used Keggin and Dawson type silicotungstate and phosphomolybdate POMs for their studies. The fabrication of PDDA-CNTs/POMs nanocomposite is shown in Scheme 1.2.

The oxidation of CNT surface was carried out by sonicating 3:1 sulfuric acid and nitric acid. Then positive PDDA is electrostatically adsorbed on negative CNT. Then negative POMs are electrostatically adsorbed on a positive PDDA wrapped on a CNT. The cyclic voltammetric studies show that the redox activities of the POMs are preserved after the immobilization on the CNT.

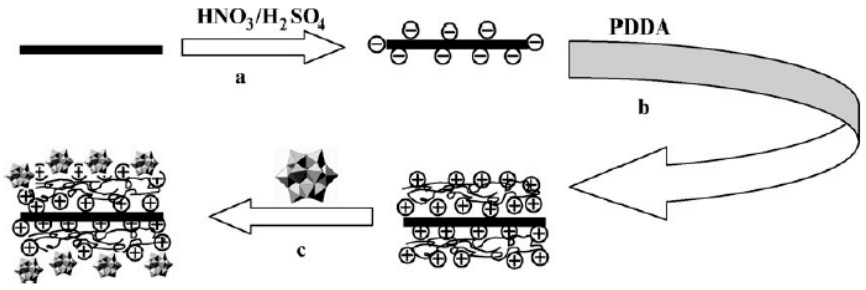

Scheme 1.2 schematic illustration of the procedures for the fabrication of PDDA-CNTs/POMs nanocomposite. (a) Ultrasonic oxidation of CNTs in a mixture of sulfuric acid and nitric acid (3:1). (b) Deposition of PDDA on negatively charged CNTs with formation of CNT-PDDA nanohybrid materials. (c) Adsorption of the POMs to functionalize PDDA-wrapping CNTs.

(Reprinted from reference 28 with permission from Elsevier)

Qu, et al. have successfully applied Co(III)-tetramethyl pyridyl porphyrin (Co-TMPyP) modified MWNT as electrocatalyst for oxygen reduction reaction (ORR)[29]. Since, Co-TMPyP is stable only at slightly acidic pH its maximum activity towards ORR was at pH 3.8 which is not suitable in real fuel cell application. But the Co-Dawson POM is stable at low pH such as pH 1. Therefore, we decided to immobilize Co-Dawson on a

purified MWNT. Chapter 4 presents the electrocatalytic activity of the acid treated MWNT-Co-Dawson adduct towards oxygen reduction reaction.

1.3 Combinatorial Material Library Preparation using Bipolar Technique:

Electrosynthesis is the synthesis of desired material from its precursors using an electrochemical reaction at the electrode-electrolyte interphase. Examples of this are the synthesis of pure metals & alloys, thin polymer films, semiconductor films by electrochemical atomic layer epitaxy (ECALE), and inorganic and organic compound electrosynthesis. Product formed on the electrode surface is sensitive to applied potential for a given temperature. This fact is useful to tune the product from a given reactant. If we can carry out the electrochemical reaction with a gradient in electrode potential, then a variety of products can be obtained in a single run. The next section will give a detailed description of methods to establish electrode potential gradients on conducting surfaces.

1.3.1 Surfaces with Gradient Chemical or Physical Properties:

Most of the naturally occurring events or matters undergo a "gradual change" as opposed to an "abrupt change" in their properties with respect to time or space. More important, some of the physiological functions in our body are accomplished by certain chemical concentration gradient existing across biological cell walls or within the cell components. Scientists have tried to mimic the chemical gradient in the biological systems on man-made substrates for scientific studies. The surfaces with biomolecular gradient produced notable applications in biological fields such as cell adhesion and motility[30]. Aside from biomolecules, a thin film of copper metal with spatially varying thickness has been deposited on a gold electrode by establishing an in-plane electric field gradient[31]. This led to the idea of depositing two components with different redox

potentials under the same condition to make varying compositions in a single run. Bringing down the possible combinations of two components on the same substrate in a single run makes the analysis of the deposited materials less time consuming given advanced locally probing techniques such as micro Raman spectroscopy and scanning electron microscopy.

1.3.2 Gradient Surfaces by Electrochemical Methods:

This method has the advantage of tuning the properties of the electrodeposited material by several factors such as composition and concentration of the electrolyte components, electrode potential, and operating temperature. Here the material gradient is obtained by establishing electrode potential gradient. Electrode potential gradient can be established in two ways: (i) by using a bipotentiostat or (ii) by using a simple power supply.

(i) Obtaining Potential Gradient using a Bipotentiostat:

Terrill et. al. have produced chemical potential gradient in alkanethiol adsorbed on a thin 50nm gold film in a 0.5M KOH/5mM octanethiol in methanol solution using a bipotentiostat. This is based on the fact that an in-plane current, i, passing through a thin gold film (5 nm ≤ thickness ≤ 80 nm) of resistivity, $\rho(l)$, and cross section, A, produces an in-plane potential, $V(x)$[32]. The magnitude and position of the in-plane potential relative to a solution reference couple can be tuned by adjusting the magnitude of the current, i, and the potentiostat voltage offset, V_0, respectively. The spatial distribution of the in-plane potential can be calculated using Equation 1.1.

$$V(x) = V_0 + \int_0^x \frac{i\rho(l)}{A}\,\mathrm{d}l \tag{1.1}$$

The electrochemical potential gradient on the substrate is then transformed into a chemical potential gradient of octanethiol, because octanethiol undergoes reductive desorption and oxidative adsorption on gold electrode surface. In Figure 1.12 in the middle panel, the cyclic voltammogram shows the reductive desorption of octanethiol from gold at $V <$ -0.8 V vs Ag/AgCl. A current was passed through the thin gold film in 0.5M KOH/5mM octanethiol in methanol to create a potential gradient of 15 mV/mm. It leads to a gradient desorption of octanethiol in the left side of the gold electrode. Octanethiol molecules are hydrophobic. If the free gold sites created by the desorption of octanethiol are backfilled by thiol molecules with a hydrophilic end group, then a gradient of hydrophobicity will be established. By analyzing the gradient in hydrophobicity using Sessile drop water contact angle measurement, we can image the chemical gradient on the gold substrate. So, after the desorption of octanethiol in a gradient manner the substrate was taken out and washed with pure solvent for a very short time and the free gold sites created by the desorption of octanethiol are backfilled by mercaptopropionic acid (MPA) by soaking the gold substrate in 5 mM MPA methanolic solution for 2 minutes. The chemical gradient was analyzed by Sessile drop water contact angle measurement. Figure 1.12 bottom panel shows the chemical gradient on gold substrate after desorption of octanethiol with potential gradient and backfilling of MPA. The top panel shows the cosine function of the Sessile drop water contact angles with respect to position on the gold substrate. Electrode potential and its position on the gold substrate are matched on the top and the middle panel. We can clearly see the variation in the contact angle in the region from -600 to -1000 mV vs Ag/AgCl. This is the region where the octanethiol undergoes reductive desorption under the control of

electrode potential. The contact angle is almost constant where there is no gradient of molecules, i.e. either octanethiol or MPA alone is present.

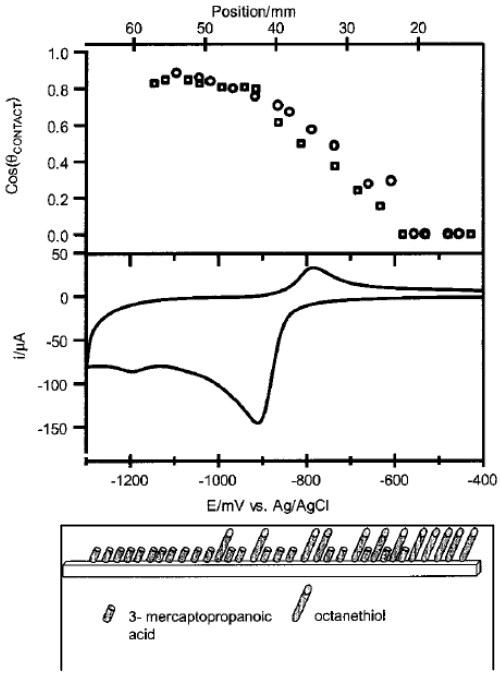

Top panel

Middle panel

Bottom panel

Figure1.12 Top panel: Sessile drop water contact measurement on the chemical gradient of octanethiol and MPA on the gold thin film with respect to position on the gold thin film of 60mm length.

Middle panel: Cyclic voltammogram of octanethiol reductive desorption and oxidative adsorption in 0.5M KOH/5mM octanethiol in methanol solution. The electrode potentials on the x-axis in the middle panel are matched with the positions on the gold thin film indicated by the x-axis in top panel.

Bottom panel: The schematic representation of the gold thin film after gradient desorption of octanethiol and backfilling of MPA.

(Reprinted with permission from Ref . 32

These results indicates successful establishment of an in-plane potential gradient on a thin gold film using a potetiostat. The 200 mV early start of octanethiol desorption on top panel compared to the onset of thiol desorption potential in the cyclic voltammmogram (presented in the middle panel), which was acquired at a faster scan rate (100mV/second), indicates that there is a kinetic barrier to octanethiol desorption from gold substrate. The gradient in reductive desorption of thiol molecules from thin gold film have also been visualized using fluorescent nanospheres covalently bound to the backfilled functional thiol molecules[33]. As a biological application, the chemical gradient of counterpropagating –COOH and -OH terminated thiol molecules was used to make the gradient of extracellular matrix protein, fibronectin on a gold substrate. The protein was attached to the –COOH terminals using the carbodiimide coupling chemistry and the –OH groups retard the non-specific adsorption of proteins on them[30].

Not only reductive desorption of thiol, but also metal deposition can be carried out with the in-plane potential gradient. Balss et al. have spatiotemporally controlled the copper deposition on a thin gold film by manipulating the in-plane potential gradient based on Equation 1.1[31]. Changing the potentiostat voltage offset, V_0, from one value to another while keeping the other parameters the same will spatially shift the potential window on the gold electrode.

Figure 1.13 illustrates how the potential window can be spatially shifted on a thin gold film electrode. The bottom of the figure shows the cyclic voltammogram of copper deposition and dissolution on gold. Spatiotemporal control of copper deposition was carried out from a 0.5 mM $CuSO_4$/0.1 M K_2SO_4 solution on the gold thin film. Initially the electrode potential window was set to be in the anodic region where there is no

copper deposition occurs on gold. Then the potential window was moved in the cathodic direction with 50mV increment until ~75% of the gold electrode was covered by copper. For each 50mV potential increment the copper deposition was carried out for 30s on bare gold substrate and the surface plasmon reflectance (SPR) images were collected at the position of the bare gold resonance. Four intermediate sample images were given in Figure 1.13. The positions of the electrodes were matched up with the potential window shown in the cyclic voltammogram given at the bottom of the figure. The grayscale code for gold and copper is shown at the right side. The brightest indicates copper and the darkest indicates gold. The four sample SPR images shows that as the potential window moves in the cathodic direction, the length of copper deposition increases as expected. These results prove the flexibility of controlling the potential gradient on an electrode with respect to space and time.

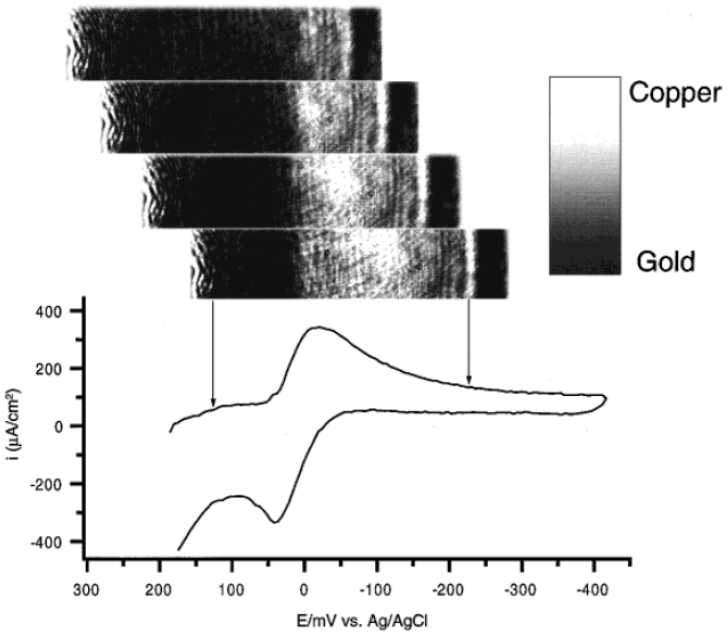

Figure 1.13. Top: Surface Plasmon Reflectance (SPR) images of gold substrate with spatially controlled copper deposition with constant shift in the potential window in the cathodic direction for each image (from top electrode image to bottom one). The SPR was set at the position of the bare gold resonance.

Bottom: cyclic voltammogram of copper deposition and dissolution on gold.

(Reprinted with permission from Ref . 31

Copyright © 2001, American Chemical Society)

Apart from sorption phenomena, electrochemical reactions have also been demonstrated with in-plane potential gradient. Hydrogen peroxide oxidation to oxygen was carried out on a thin gold film with in-plane potential gradient and the size of the oxygen gas bubble was found to depend on the potential as shown in Figure 1.14[31]. The photograph was taken after 20 minutes of oxidation of an aqueous solution of 10mM

hydrogen peroxide in 0.1 M K_2SO_4 on a gold electrode with established in-plane potential gradient as shown in the figure.

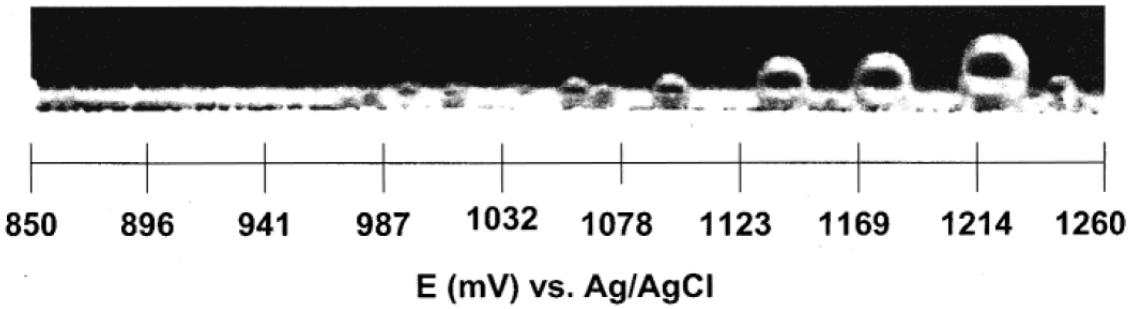

Figure 1.14. Size of the oxygen gas bubble increases with increasing positive potential on a thin gold film electrode in 10 mM hydrogen peroxide aqueous solution with 0.1 M K_2SO_4.

(Reprinted with permission from Ref . 31

According to the Butler-Volmer Equation (Equation 1.2), the electrochemical reaction rate, k_b, is an exponential function of overpotential, η.

$$k_b = k^0 e^{(1-\alpha)nf\eta} \tag{1.2}$$

where k^o is the intrinsic rate constant (i.e. rate constant at zero overpotential), α is the transfer coefficient and $f = F/RT$. The reaction rate increases when the overpotential increases. Oxygen evolution from aqueous solution of hydrogen peroxide starts from ~ +1050 mV vs Ag/AgCl. Increasing the potential positive with respect to this potential will increase the rate of oxygen evolution and will lead to a larger size oxygen gas bubble. As expected, the size of oxygen gas bubble increases with increasing positive

potential although the size of the gas bubble is dependant on some other factors (such as local temperature) as well.

(ii) Potential Gradient using a Power Supply (Bipolar Technique):

In contrast to controlling the galvani potential of the metal electrode while keeping the solution potential constant as we saw in section 1.3.2 (i), here the solution potential is manipulated between two driver electrodes using a power supply while the galvani potential of the metal is not disturbed. A conducting substrate floating in the solution parallel to the applied electric field between the driver electrodes will have a gradient of electrode-electrolyte interfacial potential though the galvani potential of the floating metal body is the same at all points. If the applied electric field between the two driver electrodes exceeds a threshold value then anodic and cathodic processes start to occur on the two sides of the floating conducting body with a charge balance[34]. The anodic reactions occur on the side which is near to the negative driver electrode and the cathodic reactions occur on the side which is near to the positive driver electrode in order to maintain the electroneutrality in the electrolyte. Since, both the anodic and the cathodic processes occur on the same substrate, the floating body is called bipolar electrode. The Figure 1.15 is the schematic representation of the bipolar electrode setup.

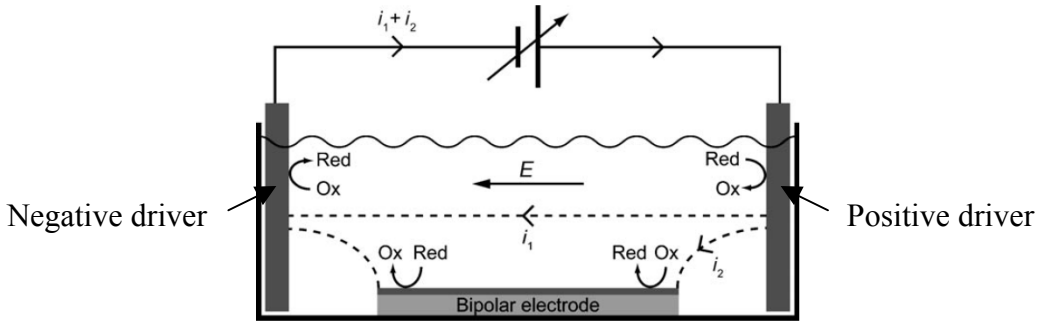

Figure 1.15 Schematic representation of a bipolar electrode setup. The dotted lines show the current paths arising from electrochemical reactions taking place in the cell.

(Reprinted from reference 34 with permission from Wiley.)

The notable difference between establishing potential gradient using a bipotentiostat and a power supply is that no wire connection is required for the bipolar electrode. But, similar kind of tasks can be achieved here also.

Ulrich et al. have made a gradient by counterpropagating mixed molecules of HS-C_2H_4-(O-C_2H_4)$_6$-OCH_3 (mPEG) and HS-C_2H_4-(O-C_2H_4)$_8$-COOH (aPEG) on a gold substrate[34]. They started with mPEG self assembled monolayer (SAM) covered gold bipolar electrode. The mPEG SAM was desorbed in a gradient manner and aPEG was backfilled to get the molecular gradient. Then the –COOH groups of the aPEG were activated and lysozyme protein was attached. With each step the substrate was analyzed by imaging null-ellipsometry (here null-ellipsometry which doesn't need detector calibration and has minimized detector error is used to image the 2 dimensional surface) with the to find the thickness of the layers. Figure 1.16 shows the imaging null-ellipsometry results. Line 1 shows the thickness of the SAM after the reductive

desorption of the mPEG from the gold bipolar electrode. The gradient region spanned about 0.3 mm from 0.4 mm to 0.7 mm on the x-axis. Line 2 was taken after backfilling with aPEG. Line 3 shows the layer thickness after protein immobilization on aPEG. 2.4 nm is the dimension of the protein lysozyme and 0.6 nm thickness increase on mPEG may be due to some non-specific adsorption of the protein on mPEG.

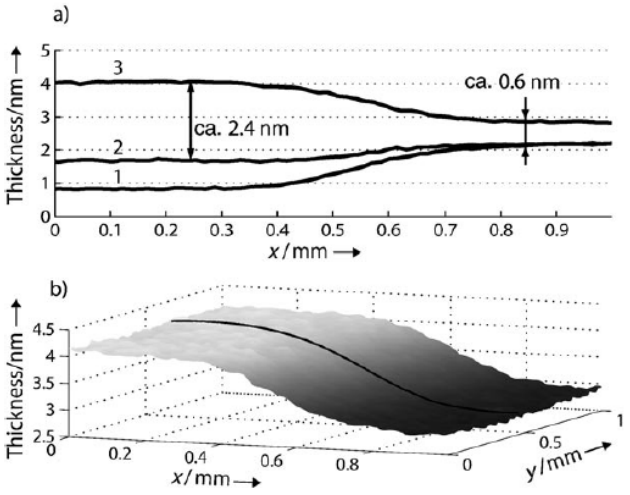

Figure 1.16 a) Line profiles, obtained from imaging-null-ellipsometry measurements, in which the thicknesses of the gradients observed after the different preparation steps are shown. Line 1 exhibits the result of the desorption of mPEG, line 2 shows that obtained after backfilling with aPEG, and line 3 represents the resulting protein gradient.
b) Thickness map of the protein gradient (the line shows the region from which the line profile was taken).

(Reprinted from reference 34 with permission from Wiley.)

Duval et al. have developed a model for characterizing the bipolar electrochemistry using an aluminium bipolar electrode in KNO_3 background electrolyte[35]. Ulrich et al. have demonstrated the potential and current distribution on a bipolar electrode using a

ferrocyanide/ferricyanide redox couple with the help of imaging surface plasmon resonance(iSPR) technique[36]. iSPR response changes with the change in the refractive index of the medium interacting with the gold substrate from where the iSPR signal is collected. The refractive index of the medium is dependent on its components. So when the ferrocyanide/ferricyanide redox couple is taken in the supporting electrolyte medium and a electrode potential gradient is established along the length of the gold bipolar substrate (from which iSPR signal is collected), then we can expect the iSPR signal to vary according to the variation in the concentration of the redox species. The concentration of the oxidized species, ferricyanide, and the reduced species, ferrocyanide, changes on the bipolar electrode with the established potential gradient. This is illustrated in Figure 1.17 (A). The magnitude of iSPR response change increases with an increase in current passed in through the electrolyte. A positive driver electrode was placed on the right side and a negative driver electrode was placed on the left side. 10 mM potassium ferrocyanide and 10 mM potassium ferricyanide were taken in 500 mM potassium nitrate supporting electrolyte. Thus, cathodic reduction of ferricyanide to ferrocyanide occurred on the left side of the bipolar with increasing rate towards the left end of the bipolar electrode. Similarly, on the right side of the bipolar electrode, oxidation of ferrocyanide to ferricyanide occurred with the rate increasing towards the right end of the bipolar electrode. This clearly indicates that from the equilibrium potential that was initially established the electrode potential increases positively towards the right end of the bipolar electrode and increases negatively towards the left end of the bipolar electrode. The saturation of the iSPR signal near the extreme ends of the bipolar electrode at higher currents is due to the mass transfer limitation of the redox species. In Figure 1.17 (B) the

measured iSPR response (dots) taken from a gold electrode in contact with the above mentioned medium under the condition of applied potential indicated in the x-axis in a three electrode setup is given along with the cyclic voltammogram of ferri/ferrocyanide redox reaction on the gold electrode. The solid line is the iSPR response calculated from Nernst equation.

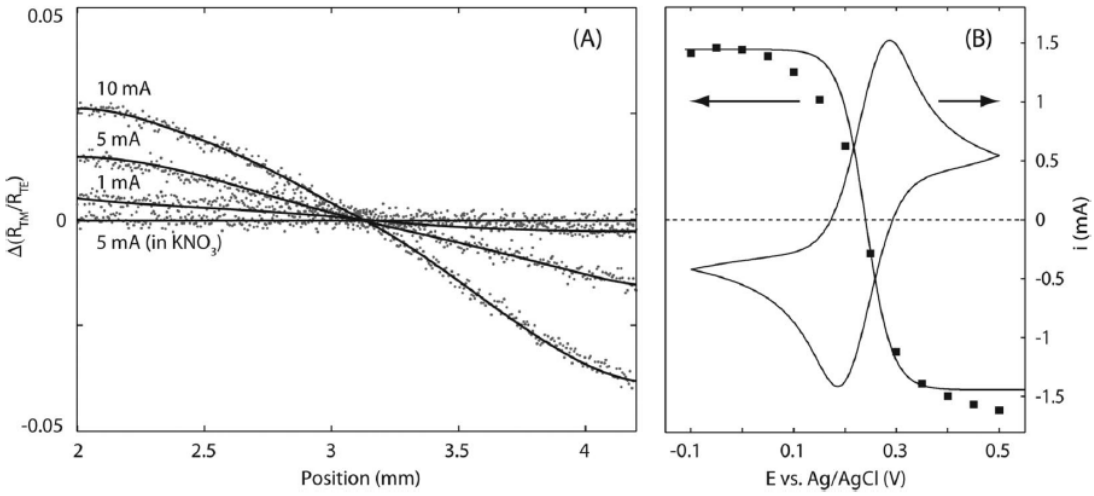

Figure 1.17. (A) The iSPR response for different currents passed through the electrolyte, simultaneously showing the regions of the reduction (left side) and oxidation (right side) reactions. (B) The SPR response for different potentials when the sensor surface acted as a working electrode in a three-electrode setup. The solid line was calculated using the Nernst equation. In both parts (A) and (B), 10 mM $K_4[Fe(CN)_6]$ $\cdot 3H_2O$ and 10 mM $K_3[Fe(CN)_6]$ were used as a redox couple together with 500 mM KNO_3 as supporting electrolyte, and the scan rate used to obtain the cyclic voltammogram was 50 mV/s.

(Reprinted with permission from Ref . 36

A bipolar electrode has been successfully applied for biosensors by Crooks and his co-workers[37]. Figure 1.18 shows the experimental scheme for detecting DNA by the bipolar electrode. The probe DNA was immobilized on the cathodic end of the gold bipolar electrode. A platinum nanoparticle (Pt-NP) was attached to the top end of the complementary target DNA and was incubated with the immobilized probe DNA. Hybridization of the target DNA with the probe DNA will bring the Pt-NPs onto the surface of the gold bipolar electrode. Since Pt-NP are highly electrocatalytic towards oxygen reduction reaction (ORR), then ORR can be used as a mean of detecting the hybridization of the DNA pair. ORR occurring on the left end of the bipolar electrode can be coupled with an anodic reaction on the right end of the same electrode as shown in Figure 1.18. Since bipolar electrode is wireless the authors decided to detect the magnitude of the cathodic or anodic reactions on the bipolar by visual means. So, they carried out oxidation of $Ru(bpy)_3^{2+}$ and tri-*n*-propylamine (TPrA) on the anodic side to get electrochemiluminescence (ECL). The results were illustrated in Figure 1.19. Figure 1.19 (c) shows that when the target DNA is hybridized with probe DNA and a sufficient voltage difference, E_{tot}, is applied between the driver electrodes there is a signal of ECL. Figure 1.19 (d) shows that there is no ECL prior to hybridization of complementary DNA even when sufficient voltage is applied between the driver electrodes. Increasing E_{tot} from 16.0 V to 20.0 V increases the cathodic and anodic reaction rate on the bipolar electrode and so the ECL intensity increases in (d). This indicates the way to signal enhancement.

Chapter 5 describes the application of this bipolar technique in material library synthesis.

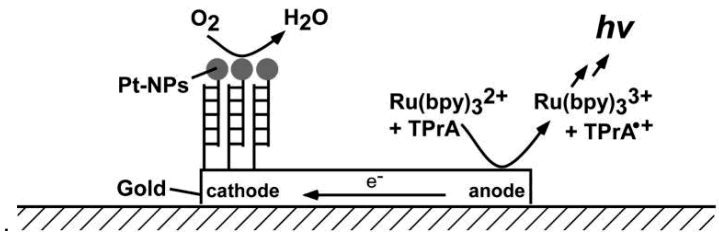

Figure 1.18 Experimental scheme for DNA detection using bipolar setup (reference 37)

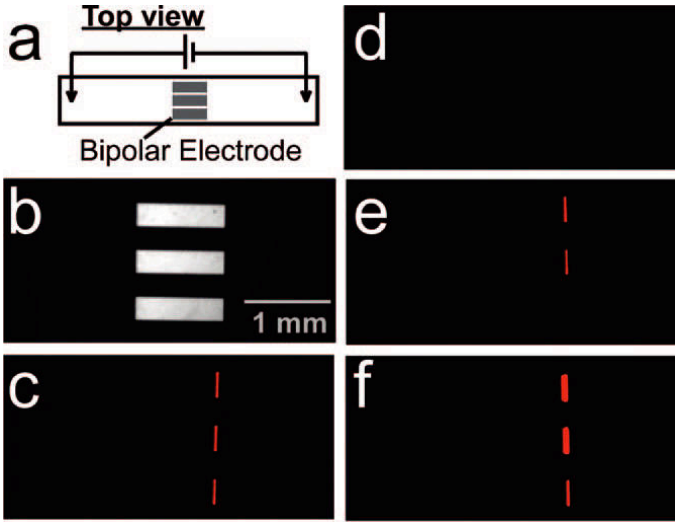

Figure 1.19 (a) Top-view representation of the DNA detector using bipolar technique (b) Optical micrograph of the bipolar electrode configuration used to obtain the ECL data in the other panels of this figure. False-color luminescence micrographs show (c) the ECL emitted at E_{tot} = 16.0 V when complementary target DNA functionalized with Pt-NPs is hybridized to probe DNA present on the electrode surface; (d) no ECL emitted at 16.0 V prior to hybridization; (e) the ECL emitted at 16.0 V when only the top two electrodes of the device are exposed to the labeled target; and (f) the ECL emission at E_{tot} = 22.0 V for the device in (e).

(Figure 1.18 and 1.19 are reprinted with permission from Ref . 37

References:

(1) Rieger, P. H. *Electrochemistry*, 2nd Ed., New York, **1994.**

(2) Stolten, D. *Hydrogen and Fuel Cells: Fundamentals, Technologies and Applications*, Weinheim, **2010**.

(3) Zhang, J. *PEM Fuel Cell Electrocatalysts and Catalyst Layers: Fundamentals and Applications*, London, **2008.**

(4) Nelson, D. L.; Cox, M. M. *Lehninger Principles of Biochemistry, Fourth Ed.*, New York, **2005**.

(5) Bockris, J. O. *Comprehensive Treatise of Electrochemistry,* Vol. 7. Plenum publisher, **1983**.

(6) Fernandez, J. L.; Walsh, D. A.; Bard, A. J. *J. Am. Chem. Soc.* **2005**, *127*, 357-365.

(7) Walsh, D. A.; Fernandez, J. L.; Bard, A. J. *J. Electrochem. Soc.* **2006**, *153*, E99-E103.

(8) Hill, C. L. *Chem. Rev.* **1998**, *98*, 1-2.

(9) Baker, L. C. W.; Glick, D. C. *Chem. Rev.* **1998**, *98*, 3-49.

(10) Atkins, P.; Overton, T.; Rourke, J.; Weller, M.; Armstrong, F. *Inorganic Chemistry*, 4th Ed., New York, **2006**.

(11) Sadakane, M.; Steckhan, E.; *Chem. Rev.* **1998,** *98,* 219-237.

(12) Mizuno, N.; Misono, M; *Chem. Rev.* **1998,** *98,* 199-217.

(13) Dawson, B.; *Acta Cryst.* **1953**, *6*, 113-126.

(14) Altenau, J. J.; Pope, M. T.; Prados, R. A.; So, H. *Inorg. Chem*. **1975**, *14*, 417-421.

(15) Banks, C. E.; Compton, R. G. *Analyst* **2006**, *131*, 15–21.

(16) Merkoci, A. *Microchim Acta* **2006**, *152*, 157–174.

(17) Cheung, C. L.; Kurtz, A.; Park, H.; Lieber, C. M**.** *J. Phys. Chem. B* **2002,** *106,* 2429-2433.

(18) Sattler, K. *Carbon* **1995**, *33*, 915-920.

(19) Hassanien, A.; Tokumoto, M. *Carbon* **2004**, *42*, 2649-2653.

(20) Gommes, C.; Blacher, S.; Masenelli-Varlot, K.; Bossuot, C.; McRae, E.; Fonseca, A.; Nagy, J. B.; Pirard, J. P. *Carbon*, **2003**, *41*, 2561.

(21) Yang, Z.; Chen, H.; Cao, L.; Li, H.; Wang, M. *Mater. Sci. Eng. B* **2004**, *106*, 73-78.

(22) Wang, S.; Zhu, W.; Liao, D.; Ng, C.; Au, C. *Catal. Today* **2004**, *93*, 711.

(23) Jorio, A.; Pimenta, M.; Souza-Filho, A.; Saito, R.; Dresselhaus, G.; Dresselhaus, M. *New J Phys.* **2003**, *5*, 139.1-139.17. doi: 10.1088/1367-2630/5/1/139

(24) Chen, J.; Rao, A. M.; Lyuksyutov, S.; Itkis, M. E.; Hamon, M. A.; Hu, H.; Cohn, R. W.; Eklund, P. C.; Colbert, D. T.; Smalley, R. E.; Haddon, R. C. *J Phys Chem B*, **2001**, *105*, 2525.

(25) Kim, B.; Sigmund, W. M. *Langmuir* **2004,** *20,* 8239-8242.

(26) Salimi, A.; Noorbakhsh, A.; Ghadermarz, M. *Analytical Biochemistry* **2005**, *344*, 16–24.

(27) Karina Cuentas-Gallegos, A.; Martínez-Rosales, R.; Rincón, M. E.; Hirata, G. A.; Orozco, G. *Optical Materials* **2006**, *29*, 126–133.

(28) Song, Y.; Wang, E.; Kang, Z.; Lan, Y..; Tian, C. *Materials Research Bulletin* **2007**, *42*, 1485–1491.

(29) Qu, J.; Shen, Y.; Qu, X.; Dong, S. *Electroanalysis* **2004**, *16*, 1444-1450.

(30) Plummer, S. T.; Wang, Q.; Bohn, P. W. *Langmuir* **2003,** *19,* 7528-7536.

(31) Balss, K. M.; Coleman, B. D.; Lansford, C. H.; Haasch, R. T. Bohn, P. W. *J. Phys. Chem. B* **2001,** *105,* 8970-8978.

(32) Terrill, R. H.; Balss, K. M.; Zhang, Y.; Bohn, P. W. *J. Am. Chem. Soc.* **2000,** *122,* 988-989.

(33) Plummer, S. T.; Bohn, P. W. *Langmuir* **2002,** *18,* 4142-4149.

(34) Ulrich, C.; Andersson, O.; Nyholm, L.; Bjorefors, F. *Angew. Chem. Int. Ed.* **2008**, *47*, 3034 –3036.

(35) Duval, J.; Mieke Kleijn, J.; van Leeuwen, H. P. *J. Electroanal. Chem.* **2001**, *505*, 1–11.

(36) Ulrich, C.; Andersson, O.; Nyholm, L.; Bjorefors, F. *Anal. Chem.* **2009,** *81,* 453–459.
(37) Chow, K.-F.; Mavré, F.; Crooks, R. M. *J. Am. Chem. Soc.* **2008**, *130*, 7544–7545.

Chapter 2

SYNTHESIS, STRUCTURAL AND ELECTROCHEMICAL CHARACTERIZATION OF TRANSITION METAL SUBSTITUTED DAWSONS AND THEIR ELECTROCATALYTIC ACTIVITY TOWARDS OXYGEN REDUCTION REACTION

2.1 Introduction:

The synthesis and characterization of transition metal substituted POMs (TM-substituted POMs), especially Dawson and Keggin type POMs, has been well established and the contribution of scientists to the due to the interesting catalytic properties of these POMs[1]. Baker[2] found that TM-substituted Keggin type POMs are analogous to metal porphyrins. Unlike porphyrins, the ligating tungsten framework in Keggin is nonoxidizable and is stable during the catalytic process. Consequently, the required transition metal can be substituted in this stable framework for a specific catalytic process. Though the synthesis of TM-substituted POMs had already been established, their application in catalysis similar to metal porphyrins was first shown by Katsoulis and Pope[3,4] in a non-aqueous solution. Later electrocatalytic properties of POMs were demonstrated in an aqueous solution[5,6]. The challenges associated with the synthesis and characterization of POMs are (1) the need to achieve the purity of the compounds, (2) the location of the substituent and (3) the identity of the ligand present in the sixth coordination site of the substituted metal[7]. To overcome these challenges an accurate

characterization of the prepared compounds is required. In compounds prepared in aqueous solutions the sixth coordinate will be a water molecule bonded to the substituted metal with the lone pair of its oxygen atom.

During the catalytic process the sixth coordination ligand is replaced by the reactant and the POM-ligated transition metal does its catalytic conversion of reactant to product with the help of the multi electron transfer and proton conduction properties of the tungsten framework. Unsubstituted and TM-substituted Dawson and Keggin type POMs are catalytically active towards many reactions such as nitrite reduction[8-10], hydrogen peroxide reduction[11,12], oxygen reduction[13], bromate reduction[14], chlorate reduction[15], etc. For this study we prepared Wells-Dawson type phosphotungstate, its α_2-mono lacunary compound (where a W-O unit is removed from the cap), and a series of α_2-transition metal substituted Dawson compounds according to established procedures given in the literature[16-20]. Scheme 2.1(A) represents the preparation of the Wells-Dawson compound and Scheme 2.1(B) represents the preparation of α_2-mono lacunary compound and α_2-transition metal substituted Dawson compounds. The prepared compounds have been characterized by FTIR, Raman spectroscopy, UV-Visible absorption spectroscopy, and Energy Dispersive X-ray spectroscopy (EDX). Their redox properties and electrocatalytic properties towards oxygen reduction reaction were studied in 0.1M $HClO_4$ (pH = 1).

Scheme 2.1 (A) Preparation of Wells-Dawson

$$18\ WO_4^{2-} + 2HPO_4^{2-} + 34\ H^+$$

Refluxing
For 4hr

$$[PW_{18}O_{62}]^{6-} + 18H_2O$$

Wells-Dawson

Scheme 2.1 (B) Preparation of α_2-lacunary Dawson compound and α_2-TM-substituted Dawson compound:

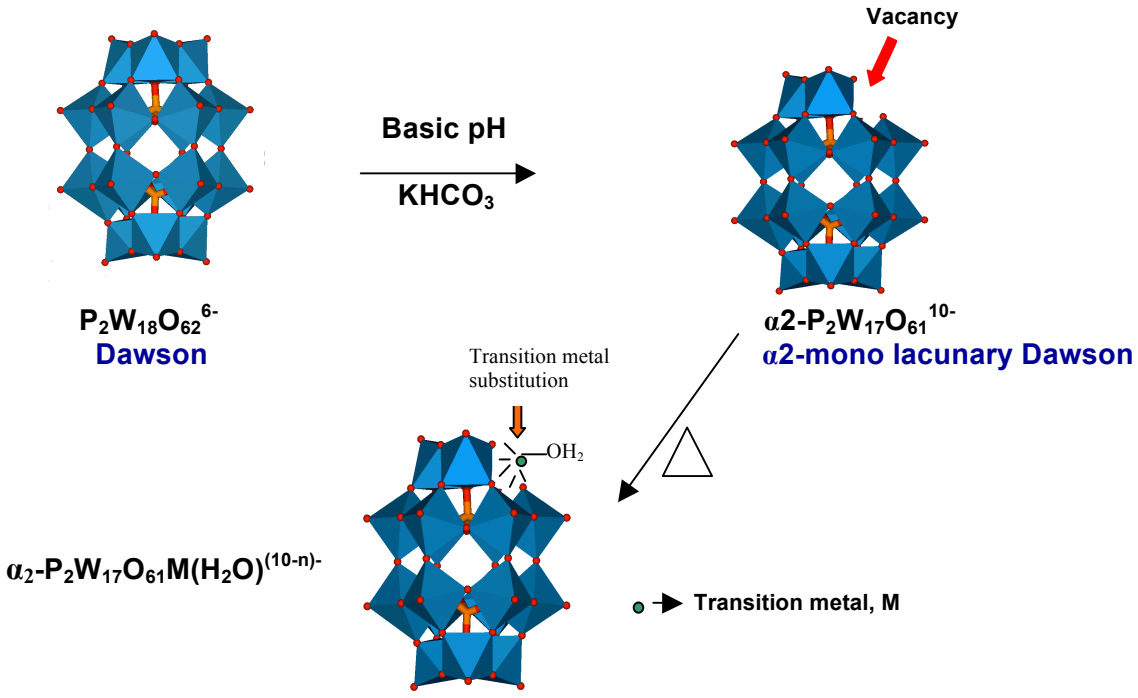

2.2 Materials and Methods:

Chemicals:

Millipore-Q purified distilled water (18MΩ) was used throughout. All of the chemicals were of high-purity grade and were used as received without further purification. Wells-Dawson and TM-substituted Dawson were prepared according to published methods.

Equipment and Apparatus:

UV-Vis spectra were recorded on a Perkin Elmer spectrometer. All FTIR analysis was done on POM loaded transparent KBr pellets on a Shimadzu spectrometer. All FTIR spectra were collected with 32 scans. Raman scattering was excited using the 514 nm output (ca. 20 mW) from an air-cooled argon ion laser (model 163-C42, Spectra-Physics Lasers, Inc.). Raman spectra were collected and analyzed using a Renishaw InVia Raman microscope system and associated software. Electrochemical measurements were carried out in a home-built three-electrode glass cell with a Pt counter electrode and an Ag/AgCl(sat) reference electrode. The Ag/AgCl(sat) electrode was isolated from the working electrode using a salt bridge and all potentials are referred to Ag/AgCl(sat) unless otherwise mentioned. The electrochemical circuit was controlled using a BAS Epsilon electrochemical workstation. The supporting electrolyte was 0.10 M $HClO_4$ prepared using 18.2 MΩ deionized water. Oxygen reduction measurements were carried out in saturated O_2 solutions.

2.3 Synthesis of Wells-Dawson and TM-substituted Dawsons:

2.3.1 Preparation of α-isomer of Wells-Dawson, $K_6[P_2W_{18}O_{62}].14H_2O$:[16]

Twenty five (25) g of $Na_2WO_4.2H_2O$ was dissolved in a mixture of 50 mL of DI water and 21 mL of 85% orthophosphoric acid. The reaction mixture was then refluxed for 4 hr and then cooled to room temperature. After cooling, 10 g of ammonium chloride were added and stirred 10 minutes to precipitate the product. A pale yellow salt was formed. The salt was separated by filtration. The salt was then dissolved in 60 mL of DI water and precipitated again with 10 g of ammonium chloride (10 minutes stirring with added ammonium chloride). The precipitated salt was filtered through a coarse frit by suction. The precipitate was then washed with a solution of 2.5 g ammonium chloride in 10 mL of DI water for 10 minutes, after which the precipitate was redissolved in 25 mL of warm water (~45°C). Four (4) g of KCl were added to the cold solution. Potassium salt of the Wells-Dawson anion was removed by filtration and then redissolved in 25 mL of hot water (~80°C). Then the solution was cooled to 15°C. White needles of triacontatungstopentaphosphate were removed by filtration. The filtrate was refluxed for 6 hr to get a solution of pure α-isomer. To this solution 2.5 g of KCl was added to precipitate the potassium salt of the α-isomer. The precipitate was filtered on a sintered glass frit and air dried for 3 days.

2.3.2 Preparation of Wells-Dawson α_2-mono Lacunary, $K_{10}[\alpha_2\text{-}P_2W_{17}O_{61}].20H_2O$:[17]

Six (6) g of α-isomer of Wells-Dawson, $K_6[P_2W_{18}O_{62}].14H_2O$, was dissolved in 15 mL of DI water. A solution of 1.5 g $KHCO_3$ in 200 mL of DI water was added to Wells-Dawson aq. solution and stirred for 1 hr. The formed precipitate is redissolved in 37.5 mL

hot DI water (95°C). Snow-like crystals that appeared on cooling to ambient temperature are filtered after 3 hr, dried under suction for 3 hr and air-dried for 2-3 days.

2.3.3 Preparation of Co-substituted Dawson, $K_8[\alpha_2\text{-}P_2W_{17}O_{61}Co^{II}.OH_2].16H_2O$:[18]

0.51 g of Wells-Dawson Lacunary, $K_{10}[\alpha_2\text{-}P_2W_{17}O_{61}].20H_2O$, in 2 mL of DI water at 90°C was stirred vigorously and 0.0336 g of $Co(NO_3)_2.6H_2O$ in 0.4 mL of DI water was added to form dark-red solution. Stirring was continued for 15 minutes. Then 0.3 g powdered KCl was added and cooled to room temperature. The formed light-red crystals were recrystallized from boiling water, washed with cold water and dried in air for one or two days.

2.3.4 Preparation of Fe-substituted Dawson, $K_7[\alpha_2\text{-}P_2W_{17}O_{61}Fe^{III}.OH_2].19H_2O$:[19]

52.8 mg $Fe(NO_3)_3.9H_2O$ was dissolved in 1.413 mL of water. To this solution, 0.56 g $K_{10}[\alpha_2\text{-}P_2W_{17}O_{61}].20H_2O$ was added by stirring at 30°C. Then the reaction mixture was left at 60°C overnight. Yellow crystals appeared and it was filtered and dried in air.

2.3.5 Preparation of Ru-substituted Dawson, $K_7[\alpha_2\text{-}P_2W_{17}O_{61}Ru^{III}.OH_2]$:[20]

This experiment was done under Ar atmosphere to avoid formation of dimer of Ru-substituted Dawson. 0.8 g $K_{10}[\alpha_2\text{-}P_2W_{17}O_{61}].20H_2O$ was dissolved in hot (90°C) water (Solution-1). 0.05 g $RuCl_3.xH_2O$ was dissolved in 3.333 mL H_2O (Solution-2). Solution-2 was added to Solution-1 slowly with vigorous stirring. The resulting mixture was maintained at 90°C with slow stirring for ca. 1hr. The reaction mixture was then cooled to 50°C. The dimer formed a brown precipitate and it was removed by filtration. To the lukewarm filtrate a solution of 0.1118 g KCl in 3.333 mL H_2O was added. Black precipitate was obtained, washed with DI water and recrystallized from MeCN.

2.4 Structural Characterization:

2.4.1 Elemental Analysis:

The prepared POMs were analyzed by Energy dispersive X-ray spectroscopy (EDX) to check the substitution of transition metals in the lacunary Dawson. The results are presented in Figure 2.1. The EDX spectrum of Dawson proves the presence of W ($M_{\alpha 1}$ at 1.775 keV, L1 at 7.388 keV, $L_{\alpha 1}$ at 8.398 keV, $L_{\alpha 2}$ at 8.335 keV, $L_{\beta 1}$ at 9.672 keV, $L_{\beta 2}$ at 9.962 keV and $L_{\gamma 1}$ at 11.286 keV), P ($K_{\alpha 1}$ at 2.014 keV, $K_{\alpha 2}$ at 2.013 keV and $K_{\beta 1}$ at 2.139 keV) and K ($K_{\alpha 1}$ at 3.314 keV, $K_{\alpha 2}$ at 3.311 keV and $K_{\beta 1}$ at 3.59 keV). The EDX spectrum of Co- or Fe- or Ru-substituted Dawson indicates the presence of corresponding transition metals: Co ($K_{\alpha 1}$ at 6.930 keV and $K_{\alpha 2}$ at 6.915 keV) or Fe ($K_{\alpha 1}$ at 6.404 keV and $K_{\alpha 2}$ at 6.391 keV) or Ru ($L_{\alpha 1}$ at 2.559 keV, $L_{\alpha 2}$ at 2.554 keV and $L_{\beta 1}$ at 2.683 keV). The larger peak of Ru is an added effect from the Cl signal ($K_{\alpha 1}$ at 2.622 keV and $K_{\alpha 2}$ at 2.621 keV) present in KCl. So, The K signal is also larger.

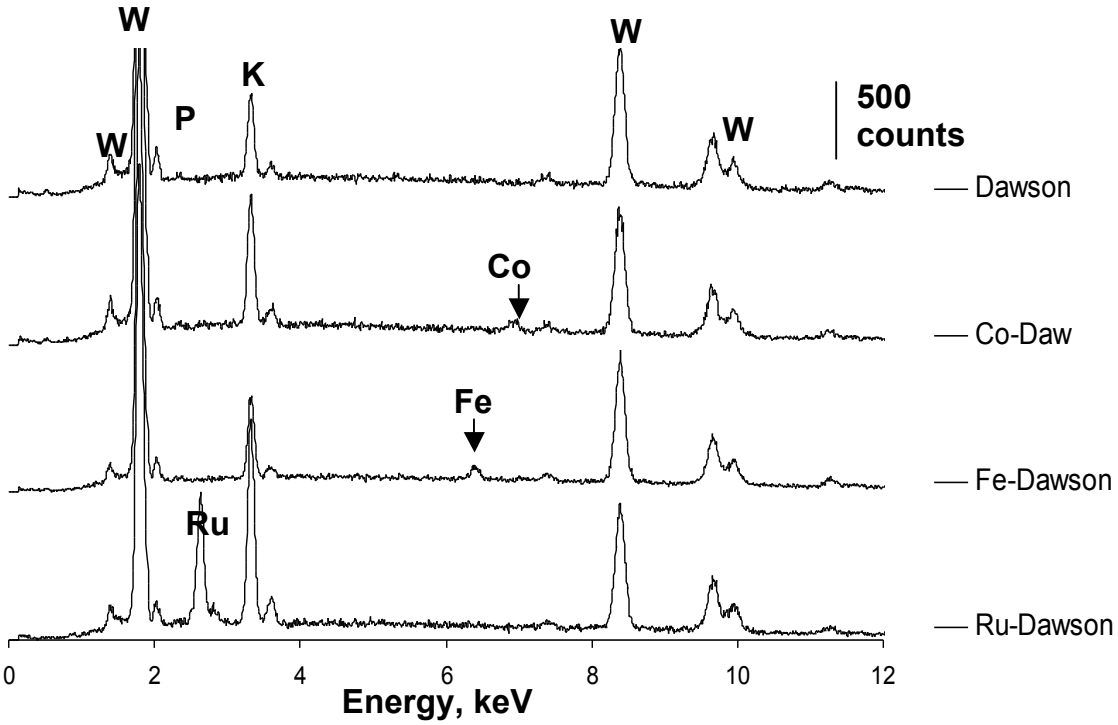

Figure 2.1 EDX spectra of Dawson and TM-substituted Dawson

2.4.2 Vibrational Spectroscopic Studies:

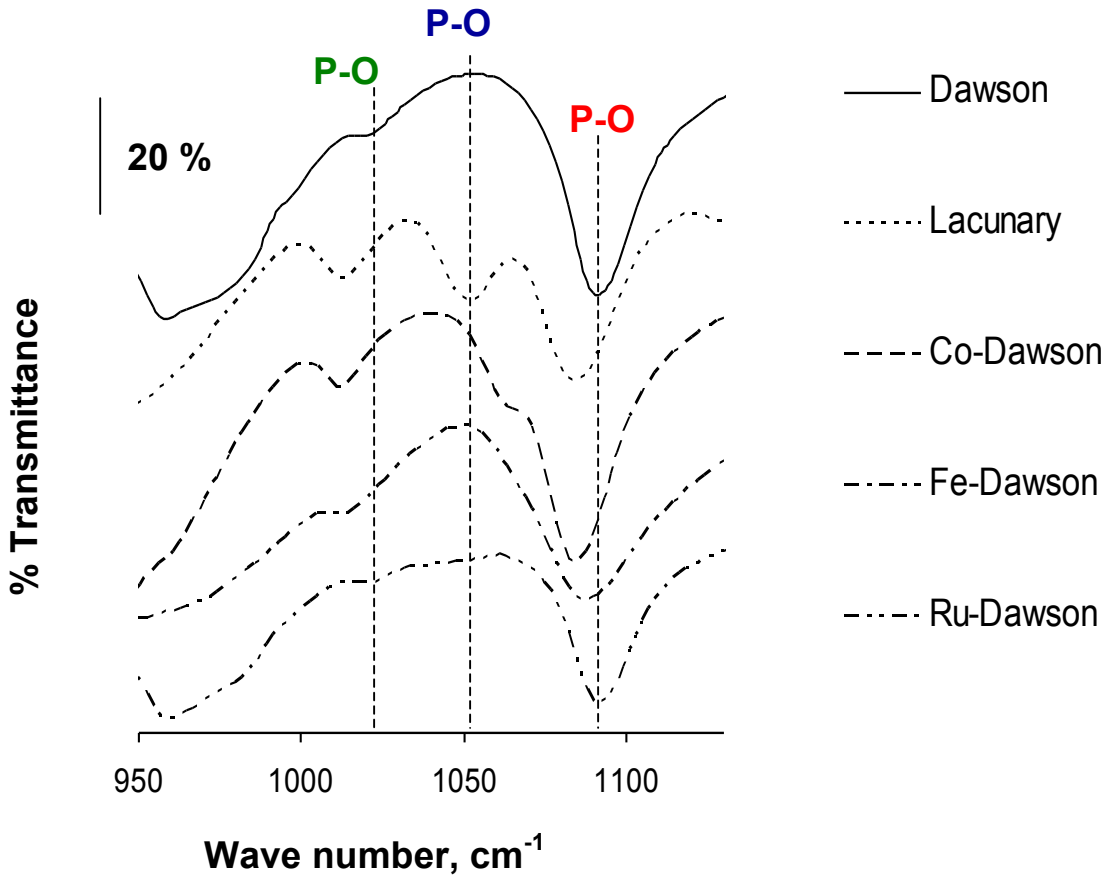

Figure 2.2a Phosphate vibrational region of FTIR spectra of unsubstituted and TM-substituted Dawson compounds

Table 2.1 P-O symmetric and asymmetric stretches from Figure 2.2a

	Dawson	Lacunary	Co-Daw	Fe-Daw	Ru-Daw
P-O (Sym)	1020	1012	1012	1012	1020
P-O (Asym)	1092	1084	1084	1088	1092
P-O (Asym)	-	1051	1063	-	-

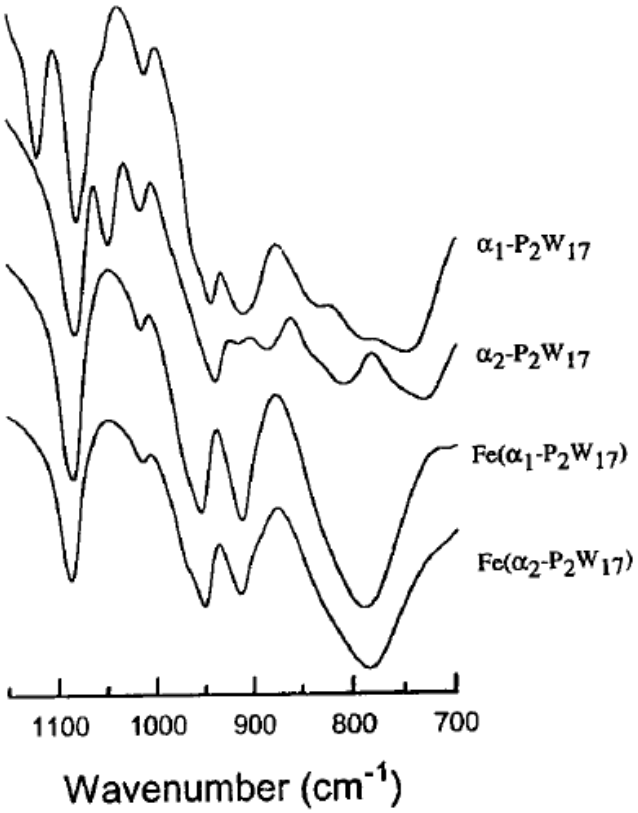

Figure 2.2b Comparison of α_1- and α_2-mono lacunary Dawson compound

(Reprinted with permission from Ref . 19

Copyright © 1997, American Chemical Society)

The vibration spectral region of phosphate shows variations with substitutions of transition metals in the Wells-Dawson structure. Figure 2.2a shows the FTIR spectra of Dawson and TM-substituted Dawsons and Table 2.1 compiles the P-O symmetric and asymmetric stretches from Figure 2.2a. The symmetric phosphate stretch at 1020 cm^{-1} and the asymmetric phosphate stretch at 1092 $cm^{-1}$of Dawson are consistent with the literature[19]. In lacunary Dawson structure the symmetry of the molecule is reduced and so the position of the phosphate symmetric and/or asymmetric stretch changes. Figure 2.2b from Reference 19 distinguishes the α_1- and α_2-mono lacunary Dawson compounds

by FTIR. Examining Figure 2.2b, the strong IR absorption of the prepared lacunary compound at 1051 cm^{-1} confirms that it is an α_2-mono lacunary compound. For the TM-substituted Dawson compounds, the obtained spectra agree with the literature[18-20] confirming that the right compounds were prepared. The terminal $W=O_t$ vibrational region of the Raman Spectra of Dawson compounds[21,22], shown in Figure 2.3, shows a similar trend as in FTIR.

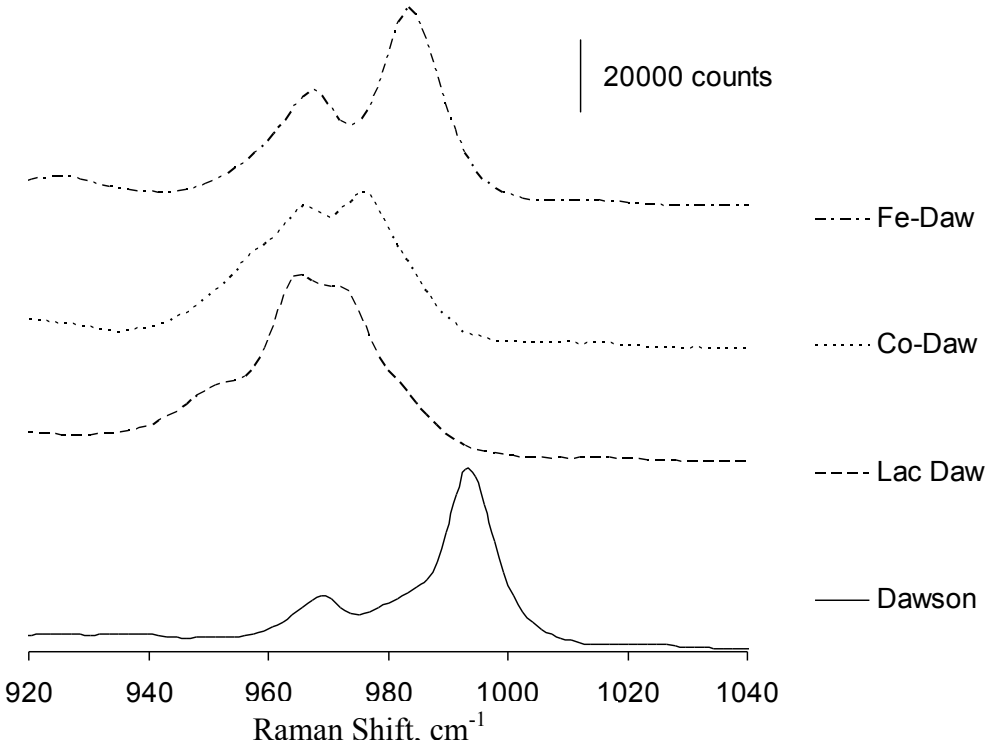

Figure 2.3 Raman spectra of Dawson and TM-substituted Dawsons.

Multiple peaks curve fitting was done with OriginPro 8.5.1 and the following results were obtained:

	Dawson	lac-Daw	Co-Daw	Fe-Daw
$W=O_t$ (asymmetric)	968	966	964	966
$W=O_t$ (asymmetric)	982			
$W=O_t$ (symmetric)	994	975	977	984

2.4.3 UV-Vis Spectroscopy:

The absorption spectra of Wells-Dawson and TM-substituted Dawson are given in Figure 2.4. The metal-ligand charge transfer (MLCT) between tungsten and oxygen occurs below 400nm in Dawson and lacunary Dawson. In TM-substituted Dawson the MLCT band of the substituted transition metal appears in the visible region, with the exception of Fe-Dawson. Co-O MLCT band occurs at 543 nm and for Ru-O it occurs at 424 nm agreeing with the literature[18,20]. For Fe-O, MLCT occurs in the near UV region and so it is not distinguishable from the W-O MLCT band[19].

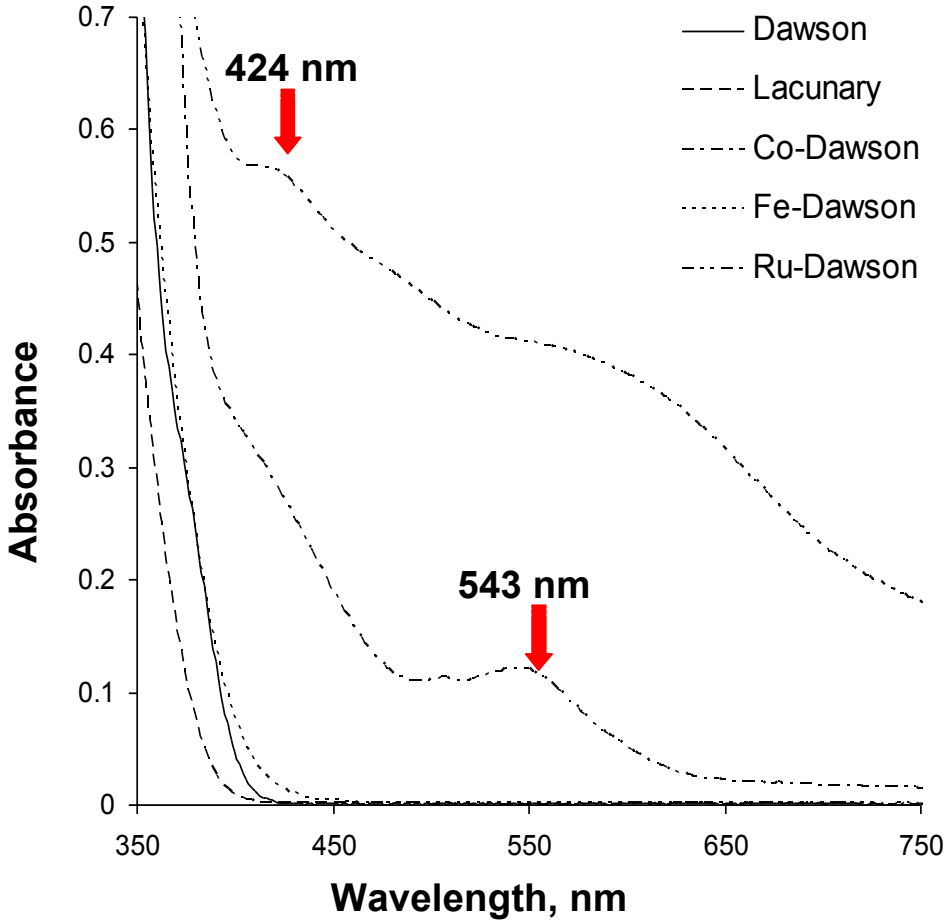

Figure 2.4 Absorption spectra of Wells-Dawson and TM-substituted Dawson

2.4.4 Powder XRD:

Figure 2.5 shows powder XRD pattern of Dawson and it is comparable with the one in the Powder XRD library.

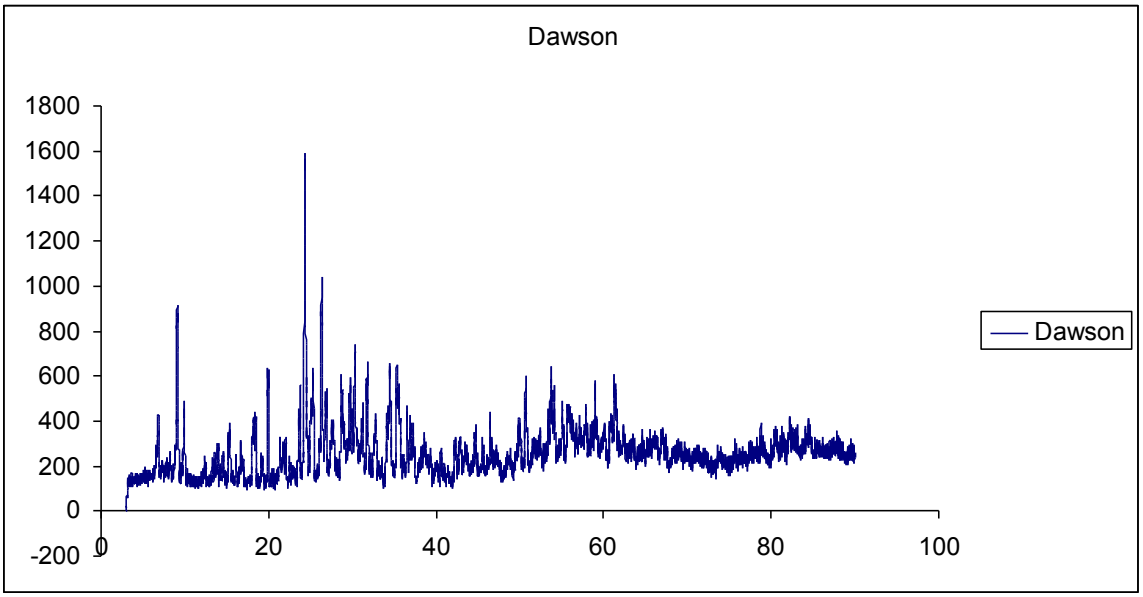

Figure 2.5 Powder XRD pattern of Dawson

2.5 Redox Properties of POMs:

The redox properties of the prepared Wells-Dawson and TM-substituted Dawsons were studied in 0.1 M $HClO_4$ (pH 1). We got three redox peaks for Wells-Dawson at pH 1 as shown in Figure 2.6: (I) 1 e^- reduction at -0.009 V, (II) 1 e^- reduction at -0.180 V and (III) 2 e^- reduction at -0.447 V. Our electrochemical results are comparable with the one obtained at pH 0[1]. The first two 1 e^- reductions are not involved in protonation and so their positions are not affected by pH. The third 2 e^- reduction, however, is accompanied by the addition of $2H^+$. Consequently, the position of the third redox peak on the potential scale will be pH-dependent according to the Nernst Equation, so that at pH 1 this redox

pair shifts to more negative potentials. The following scheme will represent the reduction process of Dawson anion in this study:

$$P_2W_{18}O_{62}^{6-} + e^- = P_2W_{18}O_{62}^{7-}$$

$$P_2W_{18}O_{62}^{7-} + e^- = P_2W_{18}O_{62}^{8-}$$

$$P_2W_{18}O_{62}^{8-} + 2e^- + 2H^+ = H_2P_2W_{18}O_{62}^{8-}$$

In lacunary Dawson, formed when an octahedral unit (one W along with a terminal oxygen atom) is removed from the cap position of the Wells-Dawson molecule, the first two one e^- reductions of Dawson merge together into one 2 e^- reduction under the operating conditions. This merged peak is named here as I' ($E_{1/2}$ = -0.111 V) as shown in Figure 2.6. The third redox peak of Dawson ($E_{1/2}$ = -0.447 V) shifts to a more positive direction in lacunary Dawson. This shift indicates that the reduction process becomes easier in lacunary Dawson than in Dawson. It could be due to the pK_a change resulting from the anion charge increase by the removal of one $[W\text{-}O]^{4+}$ unit. A more negative charge on the lacunary Dawson($P_2W_{17}O_{61}^{10-}$) compared to Dawson($P_2W_{18}O_{62}^{6-}$) may lead to higher pK_a (pK_a= 4.5), i.e, a greater affinity to accept and hold protons than Dawson(pK_a= 0.7)[23]. Usually 2 e^- reductions in POM are accompanied by protonation. So, ready acceptance of protons by lacunary Dawson leads to its being more readily reduced than Dawson.

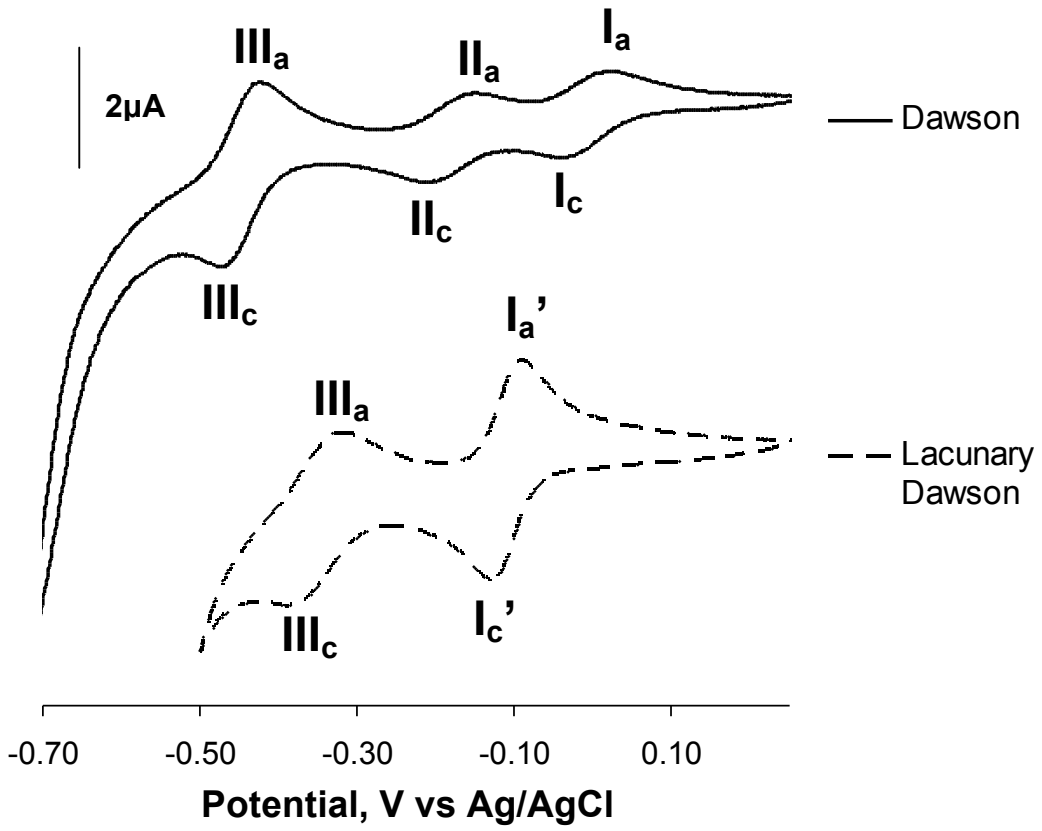

Figure 2.6 Comparison of redox properties of Dawson and lacunary Dawson. 0.2 mM POM in Ar purged 0.1M $HClO_4$ on GC electrode (area = 0.07 cm^2). Scan rate= 10mV/s.

Table 2.2 Redox pairs of Wells-Dawson:

Redox Pair	# of e^-	$E_{1/2}$, V vs Ag/AgCl
I	1	- 0.009
II	1	- 0.180
III	2	- 0.447

Table 2.3 Redox pairs of Lacunary Dawson:

Redox Pair	# of e^-	$E_{1/2}$, V vs Ag/AgCl
I'	2	- 0.111
III	2	- 0.358

Another possible explanation for this potential shift and for the merging of the first two peaks in lacunary Dawson, as given in the literature,[19] is that the molecular frame distortion is associated with the α_2 vacancy.

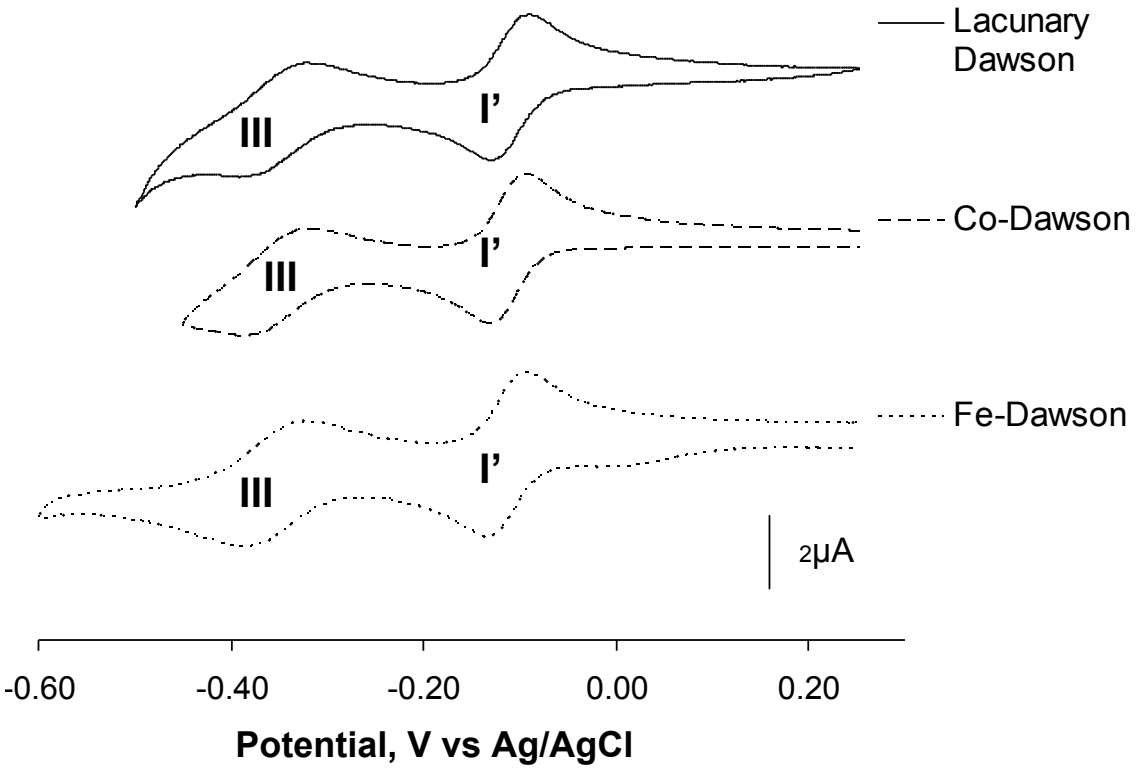

Figure 2.7 Comparison of redox properties of Co-Dawson and Fe-Dawson with lacunary Dawson. 0.2 mM POM in Ar purged 0.1M $HClO_4$ on GC electrode (area = 0.07 cm^2). Scan rate= 10mV/s.

Table 2.4 Comparison of redox pairs of Co- and Fe-Dawsons with Lacunary Dawson:

Compound	$E_{1/2}$ for I' ($2e^-$)	$E_{1/2}$ for III ($2e^-$)
Dawson		- 0.447
Lacunary Dawson	- 0.111	- 0.358
Co-Dawson	- 0.113	- 0.351
Fe-Dawson	- 0.115	- 0.358

$E_{1/2}$ values are given in V vs Ag/AgCl

Co(II) substitution in lacunary Dawson shifted the redox peak-I' only a little (2mV) towards a more negative potential and redox peak-III towards a more positive potential by 7mV. Substitution of Fe(III) in lacunary Dawson shifted the redox peak-I' by 4mV towards a more negative potential. Also, weak Fe(III)/Fe(II) redox peaks appear merging with the first tungsten frame redox peaks[19]. The redox behavior of Ru-Dawson resembles Wells-Dawson rather than lacunary Dawson as shown in Figure 2.8. But, there are some potential differences between the $E_{1/2}$ values of Ru-Dawson and Wells-Dawson redox pairs as shown in Table 2.5. Inset of Figure 2.8 shows Ru(IV)/Ru(III) redox peaks of Ru-Dawson.

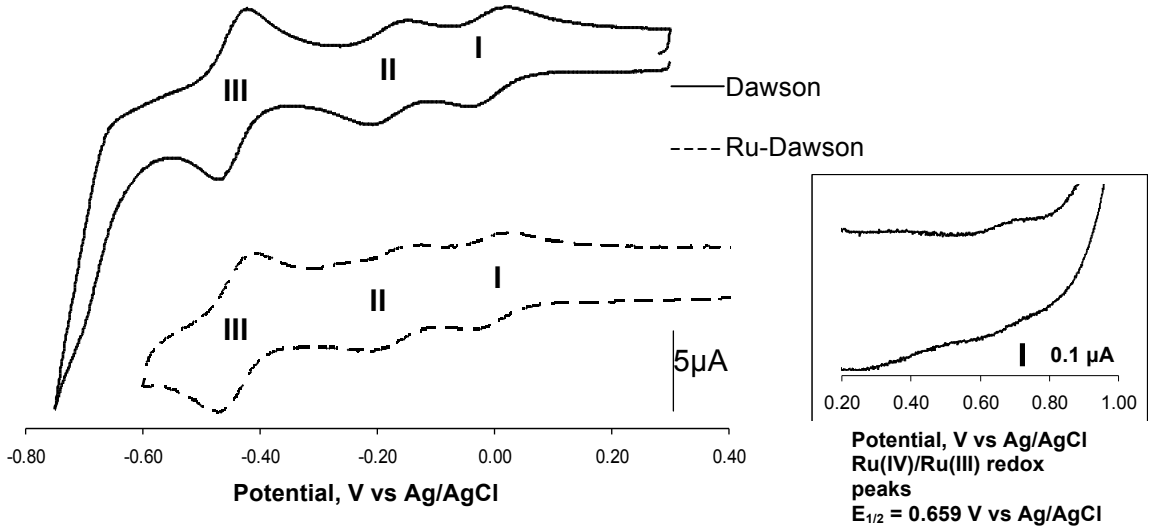

Figure 2.8 Comparison of redox properties of Ru-Dawson with Wells-Dawson. 0.2 mM POM in Ar purged 0.1M $HClO_4$ on GC electrode (area = 0.07 cm^2). Scan rate= 100 mV/s

Table 2.5 Comparison of redox pairs of Ru-Dawson with Wells-Dawson:

	$E_{1/2}$ for I ($1e^-$)	$E_{1/2}$ for II ($1e^-$)	$E_{1/2}$ for III($2e^-$)
Dawson	-0.009	-0.180	-0.447
Ru-Dawson	-0.005	-0.173	-0.442

$E_{1/2}$ values are given in V vs Ag/AgCl

2.6 Electrocatalytic Activity towards Oxygen Reduction Reaction (ORR):

Following the studies on the redox properties of the Dawson series, we studied their electrocatalytic activity towards oxygen reduction reaction (ORR) which is the cathodic reaction in fuel cells. The results are presented in Figure 2.9. The POM was dissolved in O_2 saturated 0.1M $HClO_4$ supporting electrolyte at a concentration of 0.2 mM and Glassy carbon (which is not a good catalyst for ORR) was chosen as the working electrode, Pt mesh as the counter electrode, and Ag/AgCl as the reference electrode. Only the cathodic

polarization curves are given in Figure 2.9. The order of electrocatalytic activity is as follows (the shift in $E_{1/2}$ potential with respect to bare GC is given in parentheses for each compound): Bare GC < GC+Dawson (34 mV) < GC+Co-Dawson (37 mV) < GC+Ru-Dawson (43 mV) < GC+Fe-Dawson (102 mV). The results show that (i) all the POMs are catalytically active towards ORR though the extent varies and (ii) TM-substituted Dawsons are more active than unsubstituted Dawson. The electrocatalysis of the oxygen reduction reaction coexists with the first $2e^-$ transfer in the case of unsubstituted Dawson, the second $2e^-$ transfer in the case of Co-Dawson and Fe-Dawson. Though Fe-Dawson has a slightly more negative $E_{1/2}$ value for second $2e^-$ transfer than Co-Dawson, the ORR catalytic activity of Fe-Dawson is higher than that of Co-Dawson. In Ru-Dawson ORR occurs with the first two $1e^-$ transfer with very slow kinetics and the kinetics slightly increases with the first $2e^-$ transfer. This clearly shows that the redox properties of the HPAs and the substituted metals determine the electrocatalytic properties of the HPAs.

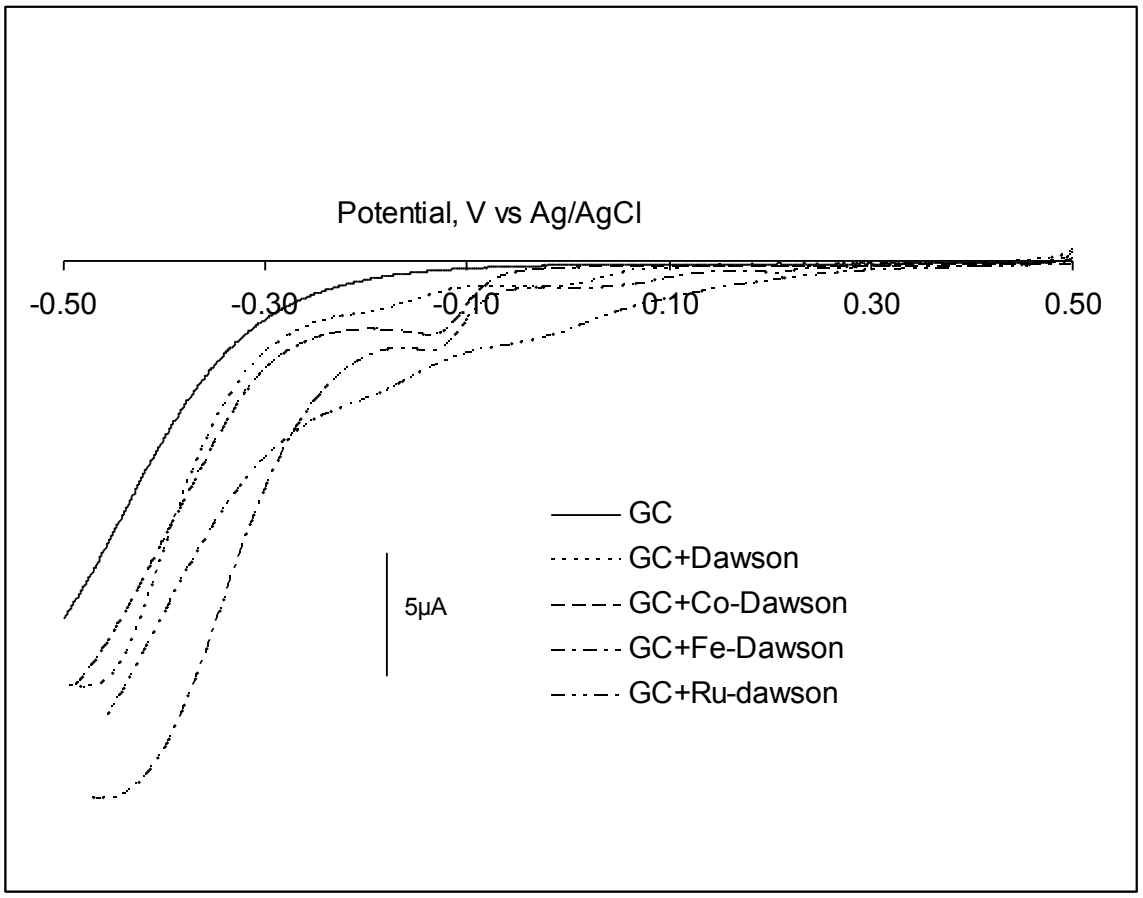

Figure 2.9 Comparison of polarization curves for ORR at unsubstituted and different transition metal substituted Wells-Dawson POM solutions at GC (3.0mm Dia) electrode in 0.1M $HClO_4$ solution (pH=1). Pt mesh acts as counter electrode and Ag/AgCl as reference electrode. Scan rate: 10mV/s.

2.7 Conclusion:

Unsubstituted and TM-substituted Dawson compounds were synthesized according to the established procedures and they were well characterized to confirm their identity. The tetrahedral distortion of phosphate group inferred from the FTIR studies correlate well with the redox properties of the prepared compounds. FTIR studies show that

lacunary Dawson, Co-Dawson, and Fe-Dawson have more distortion in the tetrahedral phosphate group and so their redox properties are well deviated from that of Dawson. But, Ru-Dawson has a FTIR spectrum similar to Dawson and its redox properties are also comparable with that of Dawson. Secondly, the redox properties of the prepared HPAs and the substituted transition metals in the HPAs determine their electrocatalytic ability towards ORR as described in section 2.6.

References:

(1) Sadakane, M.; Steckhan, E.; *Chem. Rev.* **1998,** *98,* 219-237.

(2) Baker, L. C. W. Plenary Lecture. *Proc. XV Int. Conf. Coord. Chem*., *15th* 1973.

(3) Katsoulis, D. E.; Pope, M. T. *J. Am. Chem. Soc.* **1984**, *106*, 2737.

(4) Katsoulis, D. E.; Pope, M. T. *J. Chem. Soc., Chem. Commun.* **1986**, 1186.

(5) Toth, J. E.; Anson, F. C. *J. Am. Chem. Soc.* **1989**, *111*, 2444.

(6) Keita, B.; Belhouari, A.; Nadjo, L.; Contant, R. *J. Electroanal. Chem.* **1995**, *181*, 243.

(7) Contant, R.; Abbessi, M.; Canny, J. *Inorg. Chem.* **1997**, *36*, 4961-4967.

(8) Dong, S.; Xi, X.; Tian, M. *J. Electroanal. Chem*. **1995**, *385*, 227.

(9) Keita, B.; Belhouari, A.; Nadjo, L.; Contant, R. *J. Electroanal.Chem*. **1995**, *381*, 243.

(10) Toth, J. E.; Anson, F. C. *J. Am. Chem. Soc*. **1989**, *111*, 2444.

(11) Toth, J. E.; Melton, J. D.; Cabelli, D.; Bielski, B. H. J.; Anson, F. C. *Inorg. Chem*. **1990**, *29*, 1952.

(12) Dong, S.; Liu, M. *J. Electroanal. Chem*. **1994**, *372*, 95.

(13) Keita, B.; Nadjo, L.; Haeussler, J. P. *J. Electroanal. Chem*. **1988**, *243*, 481.

(14) Cheng, L.; Zhang, X.; Xi, X.; Liu, B.; Dong, S. *J. Electroanal.Chem*. **1996**, *407*, 97.

(15) Unoura, K.; Iwashita, A.; Itabashi, E.; Tanaka, N. *Bull. Chem. Soc. Jpn*. **1984**, *57*, 597.

(16) Contant, R. *Inorg. Synth.* **1990**, *27*, 105-107.

(17) Contant, R. *Inorg. Synth.* **1990**, *27*, 107.

(18) Kharat, A. N.; Pendleton, P.; Badalyan, A.; Abedini, M.; Amini, M. M. *J. Mol.Catal. A: Chem.* **2001**, *175*, 277-283.

(19) Contant, R.; Abbessi, M.; Canny, J. *Inorg. Chem.* **1997**, *36*, 4961-4967.

(20) Liu, H.; Yue, B.; Sun, W.; Chen, Z.; Jin, S.; Deng, J.; Xie, G. *Transition Met. Chem*. **1997**, *22*, 321-323.

(21) Rocchiccioli-Deltcheff, C.; Fournier, M.; Franck, M.; Thouvenot, R. *Inorg. Chem.* **1983**, *22,* 207-216.

(22) Thouvenot, R.; Fournier, M.; Franck, R.; Rocchiccioli-Deltcheff, C. *Inorg. Chem.* **1984**, *23*, 598-605.

(23) VanPelt, C. E.; Crooks, W. J.; Choppin, G. R. *Inorganica Chimica Acta* **2003**, *346*, 215- 222.

Chapter 3

BIMETALLIC SYNERGY BETWEEN NOBLE METAL SURFACE AND ADSORBED TRANSITION METAL SUBSTITUTED POLYOXOMETALATES TOWARDS OXYGEN REDUCTION REACTION

(This work was done with the collaboration of Dr Anand Sankarraj. Synthesis and Characterization of the Dawson and Keggin type compounds used in this study were done by the author)

3.1 Introduction:

Polymer electrolyte membrane fuel cells (PEMFCs) are efficient and clean energy sources that operate at low temperatures and suitable for transportation[1-3]. Research in this field has been directed towards electrocatalysts[4,5], catalyst support materials[6,7], polymer electrolytes[8], etc. Among these, the electrocatalyst, a Pt nanoparticle, is highly expensive and either has to be replaced by an alternate material or its performance has to be improved by adding co-catalysts in order to make the PEMFCs affordable to the public. Especially the cathodic reaction, which is an oxygen reduction reaction, is kinetically sluggish in PEMFCs. Over the course of continuous trials taken by scientists to improve the oxygen reduction electrocatalyst, bimetallic catalysts were introduced by many research groups[9-14]. Walsh et al. have provided simple thermodynamic guidelines for selecting the metals to be combined together as bimetallic catalysts. They have also proved their proposal by screening the prepared bimetallic catalysts for ORR by scanning

electrochemical microscopy (SECM)[10]. According to their proposal, the oxygen reduction reaction on a metal surface can be divided into two main steps. (1) dissociative chemisorption (2) $4e^-$ reduction of dissociated oxygen atoms to water.

$$2M + O_2 \rightleftharpoons 2MO \qquad (1)$$

$$2MO + 4e^- + 4H^+ \rightleftharpoons 2H_2O + 2M \qquad (2)$$

Not all metals are the best for both steps. If we combine two metals, one good at Step 1 and another good at Step 2, then we can make the ORR facile. Figure 3.1 shows the thermodynamic guideline for a bimetallic catalyst based on Reactions (1) and (2). If a metal with high affinity for oxygen is chosen for Step 1, then it will not transfer the dissociated oxygen atom to the second metal involved in Step 2. In that case, Step 2 will not proceed. There must be a compromise when choosing the metals. The metal involved in Step 1 should be good at breaking the O=O bond, while at the same time, should allow the dissociated oxygen atoms to be transferred to the second metal. For this reason, the first metal should have not have a high negative value of Gibbs free energy for Reaction 1. The second metal, which is involved in step-2, should have reasonably positive standard potential for Reaction 2 so that it can favor reduction of dissociated oxygen atoms.

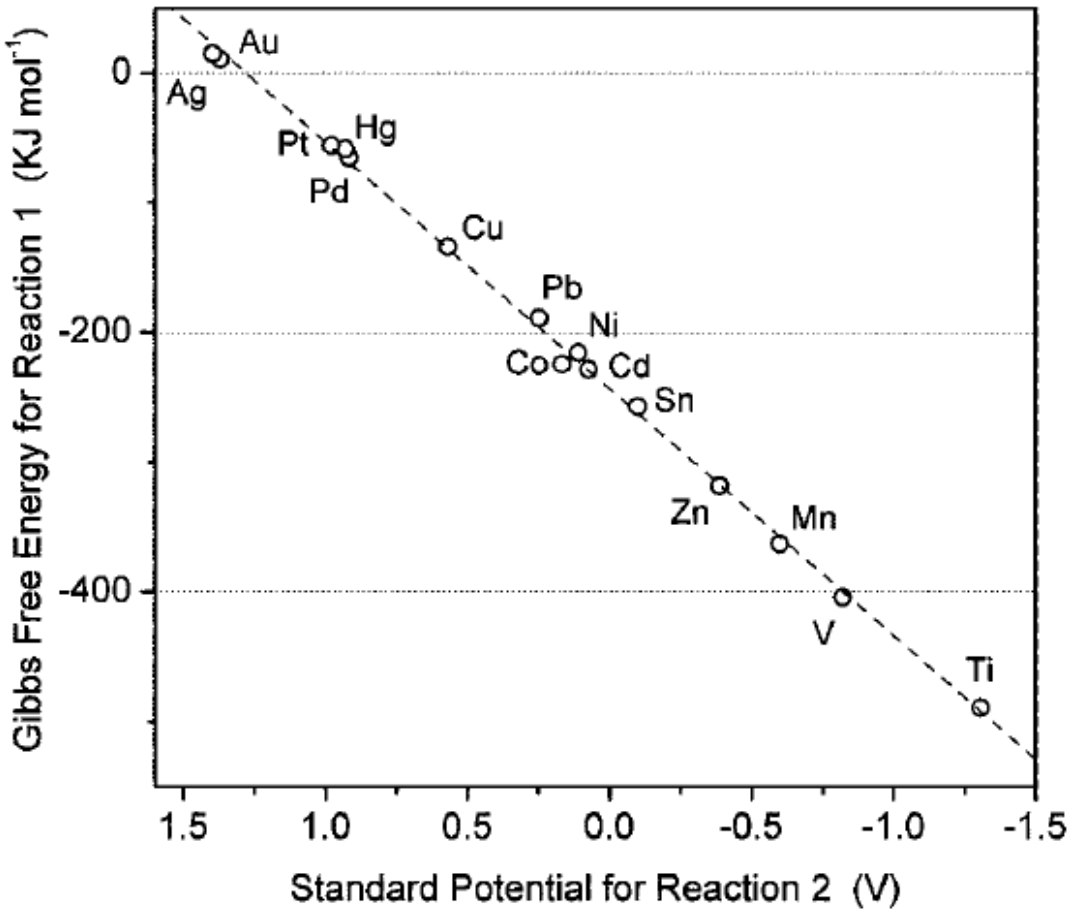

Figure 3.1 Thermodynamic guideline for bimetallic catalyst based on reactions (1) and (2).

(Reprinted from reference 10 with permission from the Electrochemical Society)

Figure 3.2 provides the schematic representation of dissociative chemisorption of oxygen molecule on a bimetallic catalyst and its reduction to water[15].

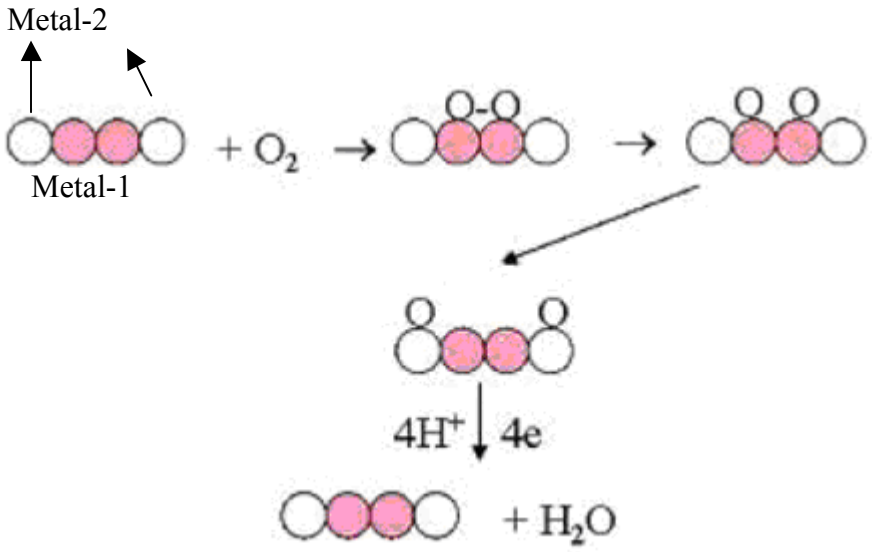

Figure 3.2 Schematic representation of dissociative chemisorption of oxygen molecule on a bimetallic catalyst and its reduction to water. (side view)

(Reprinted with permission from Ref . 15

Polyoxometalates are known for their catalytic properties due to their ability to transfer multi-electron, protons and oxygen atoms[16-19]. Many research groups have studied the oxygen reduction catalytic ability of polyoxometalates in an acidic medium using glassy carbon as well as platinum electrodes[20-22]. TM-substituted POMs adsorbed on metal electrodes which are capable of reducing oxygen can be considered bimetallic catalysts and so tried the thermodynamic guidelines given by Bard et al.[10,15] on the TM-substituted Dawson and Keggin type POM adsorbed noble metal electrodes for ORR. We chose Dawson and Keggin type POMs due to their stability at low pH which is suitable for PEMFCs applications.

3.2 Materials and Methods:

Sodium phosphotungstate hydrate, sodium tungstate and phosphoric acid were used as received from Sigma-Aldrich. $P_2W_{18}O_{62}^{6-}$ and the corresponding α_2-mono lacunary derivative were prepared using Contant's syntheses.[23,24] Co-, Fe-, and Ru-substituted Wells-Dawson compounds were prepared according to procedures in the established literature.[25-27] $PCoW_{11}O_{39}^{5-}$ was synthesized from sodium phosphotungstate following the procedure published by Weakley et al.[28] Electrochemical measurements were carried out in a home built three-electrode glass cell with a Pt counter electrode and an Ag|AgCl(sat) reference electrode. The Ag|AgCl(3M NaCl) electrode was isolated from the working electrode using a salt bridge and was calibrated against a reversible hydrogen electrode (RHE); all potentials are referenced to the RHE. The electrochemical circuit was controlled using a BAS Epsilon electrochemical workstation. The supporting electrolyte was 0.10 M $HClO_4$ prepared using 18.2 MΩ deionized water. Oxygen reduction measurements were carried out in saturated O_2 solutions.

Equipment:

Pt electrode was 1.6mm (BAS MF 2013). Au electrode was 1.6mm (BAS MF 2014), Pd electrode was 2.0mm (Alfa Aesar 99.95% metals basis), GC electrode was 3.0mm (BAS MF 2012).

3.3 Results and Discussions:

3.3.1 Bimetallic Effect of Gold with Selected Transition Metal Substituted POM:

First we applied the bimetallic synergetic hypothesis to the gold electrode with added TM-substituted Dawson type POM in oxygen saturated 0.1M $HClO_4$ supporting electrolyte. Gold was chosen as the cathode for these experiments because it is not capable of breaking the O-O bond of dioxygen as evidenced by its unfavorable free energy change for metal oxide formation which is indicated by reaction 1 in the introduction. The other metal, which is capable of breaking the O=O bond of dioxygen, is the one which is substituted in the POM skeleton. Figure 3.3 shows the cathodic linear sweep voltammograms for the oxygen reduction reaction obtained on a clean gold electrode without any added POM in the supporting electrolyte (black solid line) and with added POM in the supporting electrolyte: Dawson – blue dotted line, Fe-Dawson – blue dashed line, Co-Dawson – red dashed line, Ru-Dawson- Red dotted-dashed line. The concentration of each POM was separately optimized to maximize the shift in ORR potential shift $\Delta E^{\circ\prime}$. For Dawson, Fe-Dawson and Ru-Dawson the optimum concentration was 0.2 mM and for Co-Dawson it was 0.2 μM. The optimum concentration of each POM may depend upon their adsorption properties on the gold electrode surface.

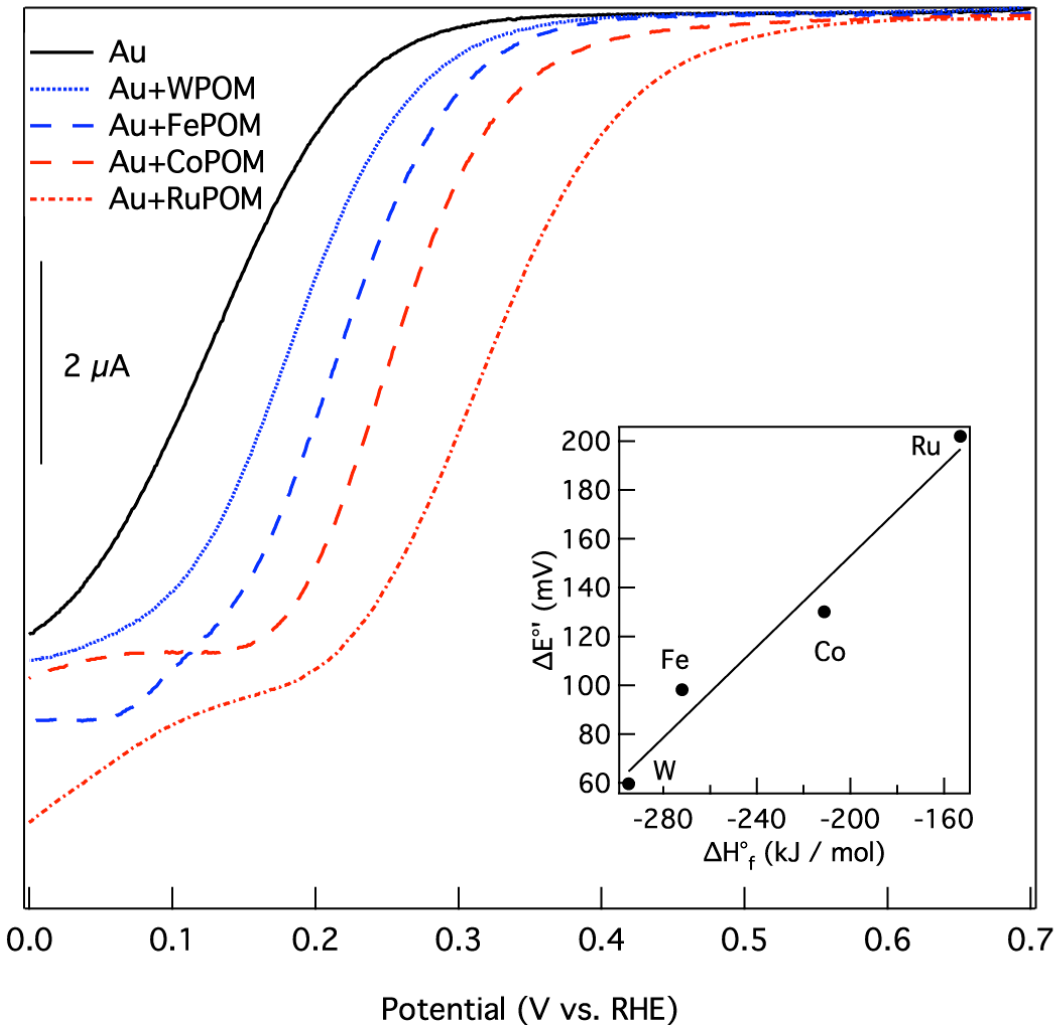

Figure 3.3 Voltammetric scans at an Au electrode immersed in O_2 saturated 0.1 M $HClO_4$. POM concentrations were [WPOM] = [FePOM] = [RuPOM] = 0.2 mM and [CoPOM] = 0.2 μM. Scan rate: 10 mV/s. Inset: Plot of maximum observed ORR potential shift, $\Delta E^{\circ\prime}$ vs ΔH°_{f} of the corresponding bulk oxide.

The trend in ORR potential shift from clean gold with the added POM correlates well with the thermodynamic stability of the bulk metal oxides of W, Fe, Co and Ru. The heat of formation (ΔH°_{f}) of bulk metal oxide[29,30] decreases in the following order: W > Fe

> Co > Ru indicating that the tungsten-oxygen bond is the strongest and the ruthenium-oxygen bond is the weakest. The stronger the metal-oxygen bond is, the more difficult to break it. Thus, further oxygen transfer to gold atoms is stopped. Therefore, the ORR potential shift is less for regular Dawson. The weaker the metal-oxygen bond is, the easier to break and transfer of the oxygen atoms to the gold surface for further reduction to water is thereby facilitated. Thus, the ORR potential shift is higher for Ru-Dawson. Since W, Fe, Co and Ru follow a decreasing order in ΔH°_{f} , the ORR potential shift follows an increasing trend with these metals substituted POMs as W < Fe < Co < Ru. This correlation is given in the inset of Figure 3.3. The maximum ORR potential shift obtained was 200mV with the Ru-Dawson.

3.3.2 Bimetallic Effect of Palladium with Selected Transition Metal Substituted POM:

When the same experiments described in section 3.3.1 were repeated with Pd cathode, which is more active towards the ORR than gold, a different trend was observed as shown in Figure 3.4. Unsubstituted and Fe-Dawson increased the overpotential for ORR compared to the clean Pd electrode with no POM added in the oxygen saturated 0.1 M $HClO_4$ electrolyte. Ru-Dawson and Co-Dawson made a positive shift in the ORR potential. But, the order is changed here, Ru-Dawson < Co-Dawson, compared to the one obtained on gold surface where Co-Dawson < Ru-Dawson. In this set of experiments, the concentration of each POM was also optimized to maximize the ORR potential shift.

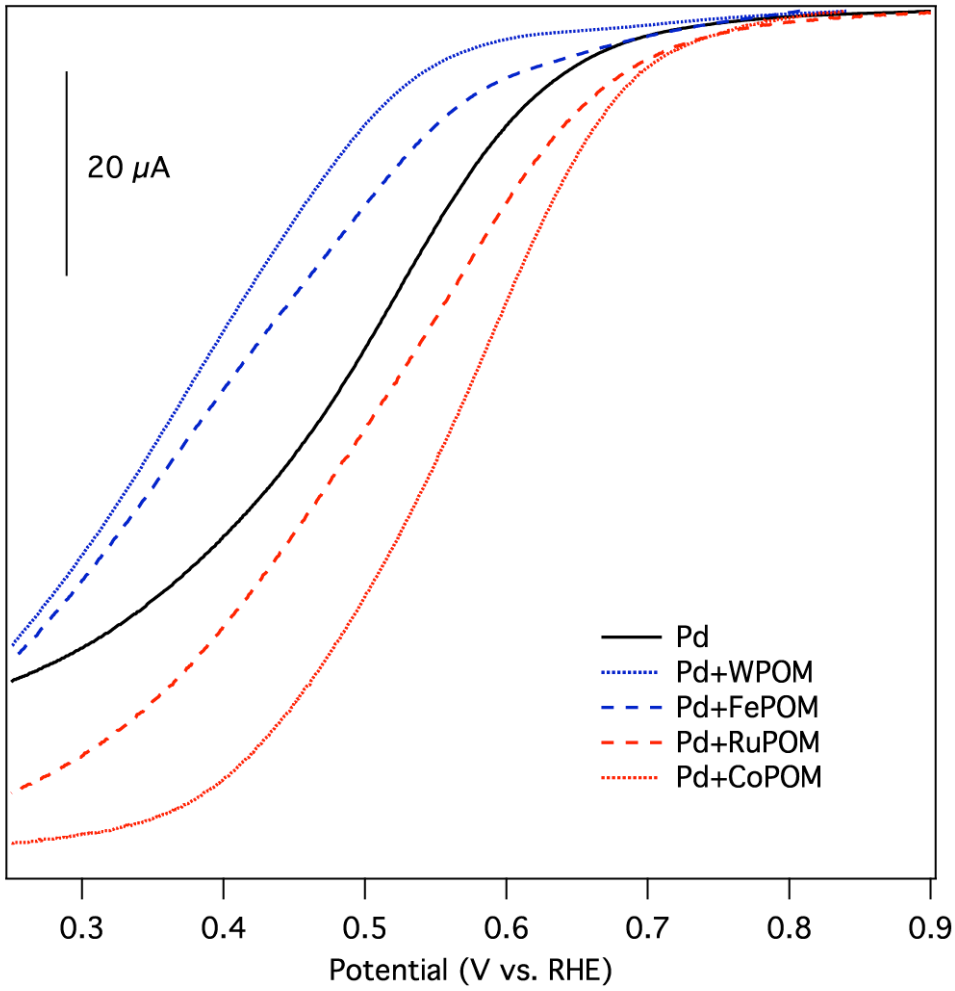

Figure 3.4 Voltammetric response of a Pd electrode immersed in O_2 saturated 0.1 M $HClO_4$. POM concentrations were [WPOM] = [FePOM] = [RuPOM] = 0.2 mM and [CoPOM] = 0.2 μM. Scan rate: 10 mV/s.

The negative ORR potential shift of unsubstituted and Fe-Dawson indicate that adsorption of these POMs on the surface of Pd electrode did not help the overall reduction of dioxygen to water. Actually, Pd itself is efficient for breaking the O-O bond in dioxygen to some extent as opposed to gold. There should always be an optimum availability of active sites for each steps of ORR mentioned above in the introduction by

Reaction 1 and Reaction 2. The nanosize molecules unsubstituted Dawson and Fe-Dawson prevent the exposure of Pd active sites by adsorbing on it, and W or Fe in the adsorbed POM molecules bind the oxygen atoms too strongly to further transfer the oxygen atoms to the Pd surface. This leads to a deviation from the optimum condition for maximized ORR potential shift. Similar observations have been reported recently in the case of phosphotungstate and phosphomolybdate anions adsorbed on Pt nanoparticles[21]. The change in the order of Ru- and Co- Dawson in the ORR potential shift may be also due to the adsorption properties of the POMs.

3.3.3 Bimetallic Effect on Pt Cathode with Transition Metal Substituted POM:

When the oxygen reduction reaction was carried out on the Pt cathode with added POMs in the oxygen saturated supporting electrolyte, negative potential shift was obtained with unsubstituted, Fe- and Ru- Dawson at all concentration tried due to unfavorable adsorption dynamics of the POM molecules on the Pt surface. When Co-Dawson was tried with various concentrations in the supporting electrolyte with Pt cathode, a trend in ORR potential shift as shown in Figure 3.5 was obtained. The 0.2 μM Co-Dawson gave a maximum shift and further increase in POM concentration gave a negative shift in ORR potential. This supports the explanation that the negative shift in ORR potential in some cases is due to the unfavorable adsorption dynamics of POM molecules. At 0.2 μM [Co-Dawson], the ORR potential was shifted 21 mV positive of that observed at a naked Pt electrode. A plot of the voltage shift as a function of concentration for the complete data set is shown in the inset to Figure 3.5.

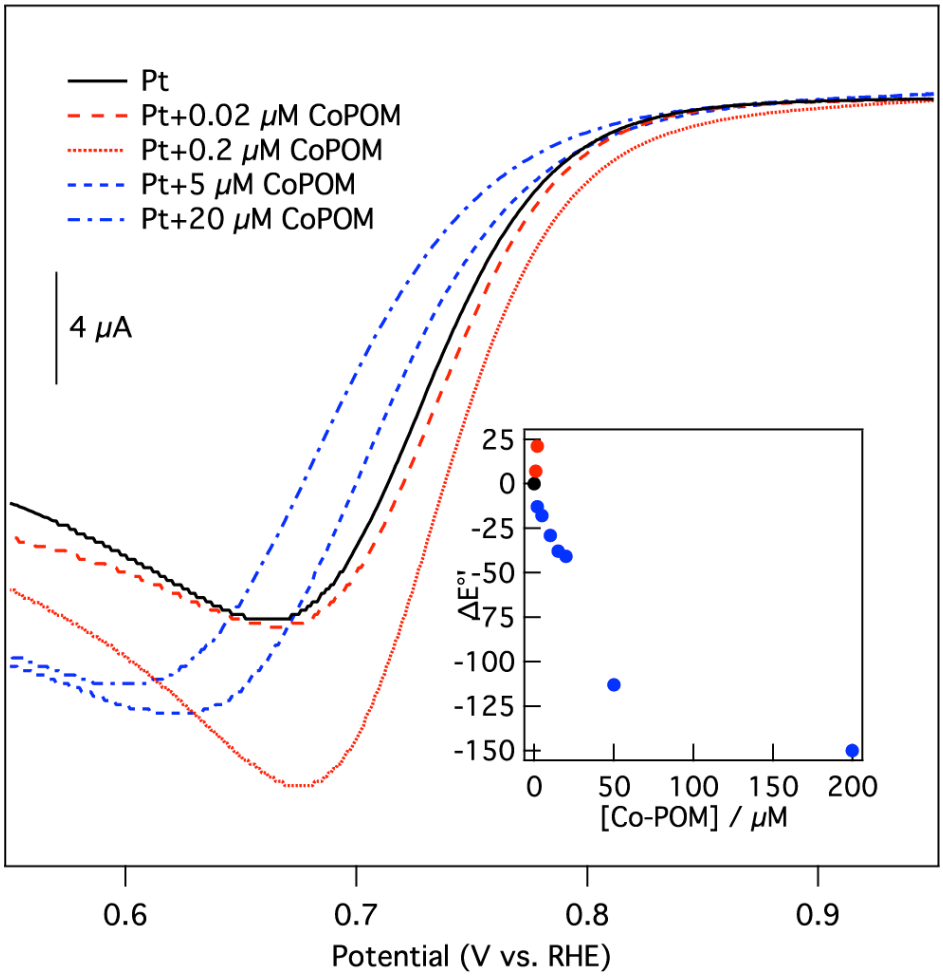

Figure 3.5 Voltammetric response of a Pt electrode in O_2 saturated 0.1M$HClO_4$ as a function of [CoPOM]. Scan rate: 10 mV/s. Inset: plot of $\Delta E^{\circ\prime}$ versus [CoPOM].

Since Keggin type POMs are less adsorbing than Dawson type POMs, we tried ORR on Pt electrode with added unsubstituted or Co-Keggin in supporting electrolyte (Figure 3.6). Unsubstituted Keggin gave a negative ORR potential shift on all concentrations tried. However, Co-Keggin gave a maximum positive ORR potential shift of 54mV at an optimum concentration of 20 μM. It supports the synergy between the Co-Keggin and Pt surface.

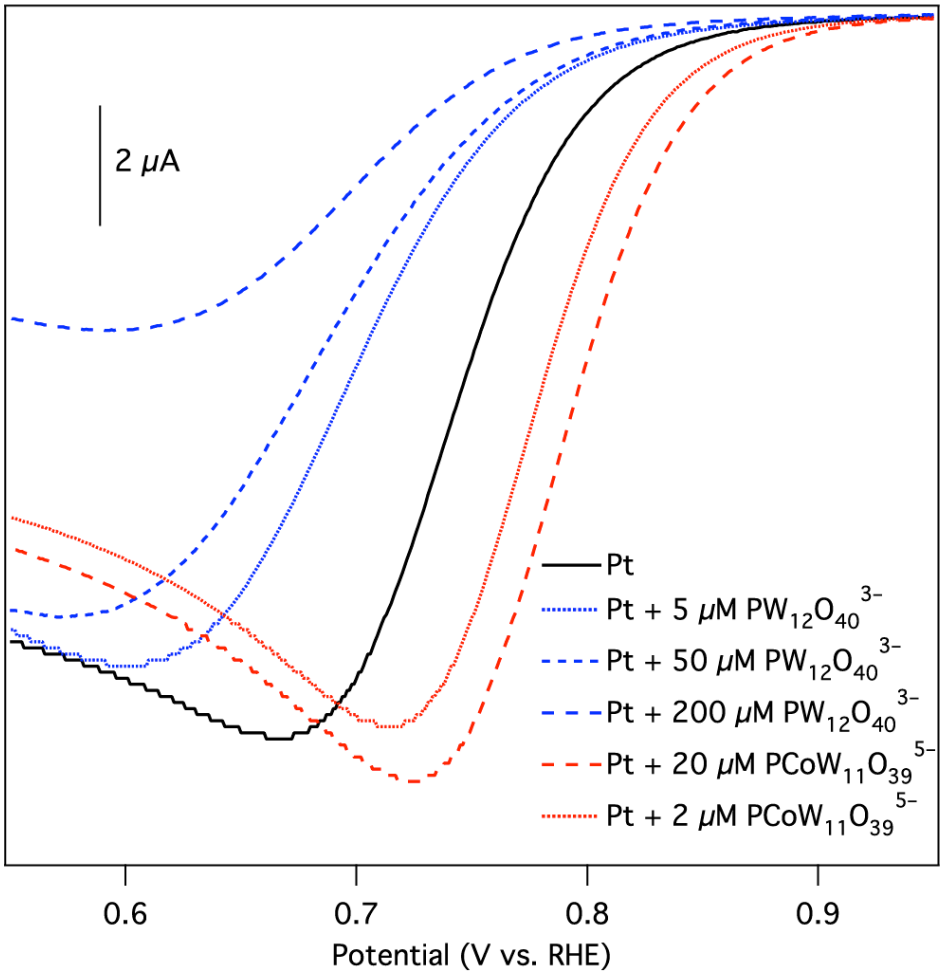

Figure 3.6 Voltammetric response of a Pt electrode in O_2 saturated 0.1 M $HClO_4$ containing the noted concentrations of $PW_{12}O_{40}^{3-}$ and $PCoW_{11}O_{39}^{5-}$ Scan rate: 10 mV/s.

3.4 Conclusion:

In conclusion, transition-metal-substituted Wells-Dawson POMs adsorbed on the surface of Au electrodes lead to positive shifts of the ORR potential by a mechanism that may be analogous to that which has been proposed for bimetallic ORR catalysts. The magnitude of the shift can be quite large (ca. 200 mV), is transition-metal-dependent, and

can be explained using simple thermodynamic concepts. In the case of more active cathode materials such as Pd and Pt, our results indicate that surface effects become increasingly important: there is an optimum concentration of POM for which catalytic activity and site blocking effects are in balance. In the case of Pd cathodes a maximum $\Delta E^{\circ\prime}$ of nearly +100 mV was observed. The best overall cathode performance was achieved using Co-Keggin in conjunction with a Pt electrode (+54 mV positive shift compared to bare Pt), and this result is comparable to the performance of bimetallic catalysts[11,31]. Finally, the approach to enhancing the performance of oxygen reduction cathodes that we have described is simple to implement and is compatible with existing fuel cell cathode materials.

References:

(1) Song, C. *Catal. Today* **2002**, *77*, 17.

(2) Li, Q.; He, R.; Jensen, J. O.; Bjerrum, N, J. *Chem. Mater.* **2003**, *15*, 4896.

(3) Gasteiger, H. A.; Kocha, S. S.; Sompalli, B.; Wagner, F. T. *Appl. Catal., B* **2005**, *56*, 9.

(4) Litster, S.; McLean, G. *J. Power Sources* **2004,** *130*, 61.

(5) Acres, G. J. K. *J. Power Sources* **2001**, *100*, 60.

(6) Wang, C.; Waje, M.; Wang, X.; Tang, J. M.; Haddon, R. C.; Yan, Y. *Nano Lett.* **2004**, *4*, 345.

(7) Bessel, C. A.; Laubernds, K.; Rodriguez, N. M.; Baker, R. T. K. *J. Phys. Chem. B* **2001**, *105*, 1115.

(8) Lee, H. C.; Hong, H. S.; Kim, Y.-M.; Choi, S. H.; Hong, M. Z.; Lee, H. S.; Kim, K. *Electrochim. Acta* **2004**, *49*, 2315.

(9) Savadogo, O.; Lee, K.; Oishi, K.; Mitsushima, S.; Kamiya, N.; Ota, K. I. *Electrochem. Commun.* **2004**, *6*, 105-109.

(10) Walsh, D. A.; Fernandez, J. L.; Bard, A. J. *J. Electrochem. Soc.* **2006**, *153*, E99-E103.

(11) Shao, M. H.; Sasaki, K.; Adzic, R. R. *J. Am. Chem. Soc.* **2006**, *128*, 3526-3527.

(12) Shao, M. H.; Huang, T.; Liu, P.; Zhang, J.; Sasaki, K.; Vukmirovic, M. B.; Adzic, R. R. *Langmuir* **2006**, *22*, 10409-10415.

(13) Shao, M. H.; Liu, P.; Zhang, J. L.; Adzic, R. *J. Phys. Chem. B* **2007**, *111*, 6772-6775.

(14) Balbuena, P. B.; Altomare, D.; Vadlamani, N.; Bingi, S.; Agapito, L. A.; Seminario, J. M. *J. Phys. Chem. A* **2004**, *108*, 6378-6384.

(15) Fernandez, J. L.; Walsh, D. A.; Bard, A. J. *J. Am. Chem. Soc.* **2005**, *127*, 357-365.

(16) Vernon, D. R.; Meng, F.; Dec, S. F.; Williamson, D. L.; Turner, J. A.; Herring, A. M. *J. Power Sources* **2005**, *139*, 141-151.

(17) Khenkin, A. M.; Weiner, L.; Wang, Y.; Neumann, R. *J. Am. Chem. Soc.* **2001**, *123*, 8531-8542.

(18) Keita, B.; Nadjo, L. *J. Electroanal. Chem.* **1987**, *217*, 287-304.

(19) Kuhn, A.; Anson, F. C. *Langmuir* **1996**, *12*, 5481-5488.

(20) Keita, B.; Mbomekalle, I. M.; Lu, Y. W.; Nadjo, L.; Berthet, P.; Anderson, T. M.; Hill, C. L. *Eur. J. Inorg. Chem.* **2004**, 3462-3475.

(21) Chojak, M.; Kolary-Zurowska, A.; Wlodarczyk, R.; Miecznikowski, K.; Karnicka, K.; Palys, B.; Marassi, R.; Kulesza, P. J. *Electrochim. Acta* **2007**, *52*, 5574-5581.

(22) Wlodarczyk, R.; Kolary-Zurowska, A.; Marassi, R.; Chojak, M.; Kulesza, P. J. *Electrochim. Acta* **2007**, *52*, 3958-3964.

(23) Contant, R. *Inorg. Synth.* **1990**, *27*, 105-107.

(24) Contant, R. *Inorg. Synth.* **1990**, *27*, 107.

(25) Kharat, A. N.; Pendleton, P.; Badalyan, A.; Abedini, M.; Amini, M. M. *J. Mol.Catal. A: Chem.* **2001**, *175*, 277-283.

(26) Contant, R.; Abbessi, M.; Canny, J. *Inorg. Chem.* **1997**, *36*, 4961-4967.

(27) Liu, H.; Yue, B.; Sun, W.; Chen, Z.; Jin, S.; Deng, J.; Xie, G. *Transition Met. Chem*. **1997**, *22*, 321-323.

(28) Weakley, T. J. R.; Malik, S. A. *J. Inorg, Nucl. Chem.* **1967**, *29*, 2935-2944.

(29) Bard, A. J., Ed. *Encyclopedia of Electrochemistry of the Elements*; Marcel Dekker: New York, 1973.

(30) Bard, A. J.; Parsons, R.; Jordan, J. *Standard Potentials in Aqueous Solutions*; Marcel Dekker: New York, 1985.

(31) Duong, H. T.; Rigsby, M. A.; Zhou, W.-p.; Wieckowski, A. *J. Phys. Chem. C* **2007**, *111*, 13460-13465.

Chapter 4

ELECTROCATALYTIC ABILITY OF Co-DAWSON TREATED MULTI WALLED CARBON NANOTUBES TOWARDS OXYGEN REDUCTION REACTION

4.1 Introduction:

Carbon nanotubes are gaining much attention in the field of electrocatalysis as supporting material due to their unique properties, such as high surface area, high electrical conductivity, significant mechanical strength, required chemical inertness, and flexibility to functionalize its surface[1-3]. Much work has been done on the modification of CNT by a variety of materials such as biomolecules[4,5], metal nanoparticles[6,7], and functional molecules[8,9]. Polyoxometalates (POMs) are nanometer scale functional molecules which can conduct protons and oxygen atoms and are involved in multielectron transfer[10-13]. CNT modified by polyoxometalates have been reported by many research groups[14-17].

Successful results by Qu et. al. on oxygen reduction reaction(ORR) electrocatalysis using a glassy carbon(GC) electrode modified with Multi-Walled Carbon Nanotubes (MWNT) and Co-Porphyrin(Co-TMPyP)[18] made us consider immobilizing the Co-Dawson, the stable inorganic analogue of Co-TMPyP, on MWNT for ORR. Their results show that when the GC electrode is modified with MWNT and then with Co-TMPyP, it leads to complete oxygen reduction to water in two 2 electron transfer steps as illustrated

by cyclic voltammogram in Figure 4.1 (e). The modification of the GC electrode with MWNT alone (b) or Co-TMPyP alone (c) or with both but in reverse order (d) catalyzes only reduction of dioxygen to hydrogen peroxide and further reduction to water is not occurring[18].

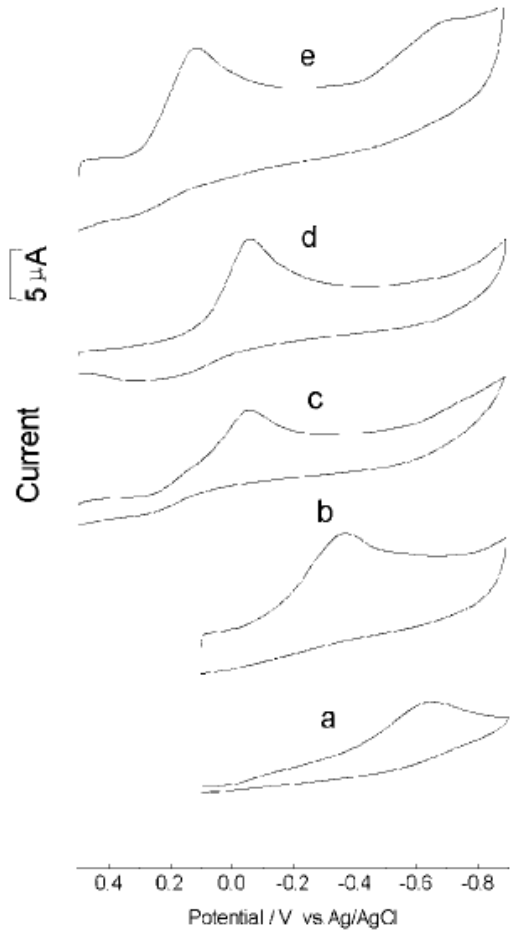

Figure 4.1 Cyclic voltammograms of O_2 reduction at different electrodes. a) blank GC electrode; b) GC/MWNTs modified electrode; c) GC/CoTMPyP modified electrode; d) GC/CoTMPyP/MWNTs; e) GC/MWNTs/CoTMPyP modified electrode. Supporting electrolyte: air-saturated 0.1 M HAc-NaAc (pH 3.8) buffer solution. Scan rate: 50mV/s . (Reprinted from reference 18 with permission from Wiley)

These results imply that the complete ORR requires the immobilization of Co-TMPyP on MWNT, not on GC. Since, Co-TMPyP is stable only at a slightly acidic pH its maximum activity towards ORR was at pH 3.8 which is not suitable in the field of PEMFC applications. Co-Dawson POM, however, is stable at low pH such as pH 1; therefore, we decided to immobilize Co-Dawson on purified MWNT and study its electrocatalytic property towards ORR. Finally we ended up with a Fe-Co bimetallic catalyst system which showed a better performance for ORR than the MWNT-Co-Dawson system.

Another notable result in Figure 4.1 is that MWNT modified GC (Figure 4.1-b) is more active than bare GC (Figure 4.1-a) towards ORR. The catalytic activity of CNTs is attributed to their ends. Depending upon the preparation method, various morphologies of MWNT include 'hollow-tube,' 'herringbone,' or 'bamboo-like,' as shown schematically in Figure 4.2[19,1].

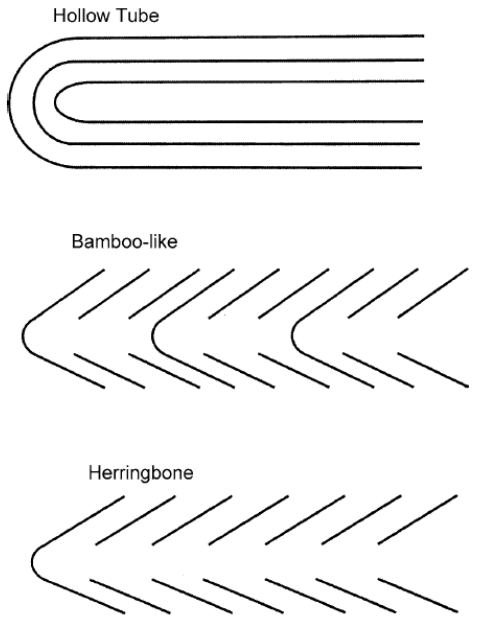

Figure 4.2 Morphological variations of MWNT

(Reprinted from reference 19 with permission from the Royal Society of Chemistry)

The ends of the MWNT are analogous to the edge-plane of a graphite structure and the tube walls of MWNT are analogous to the basal-plane of a graphite structure as illustrated in Figure 4.3[1].

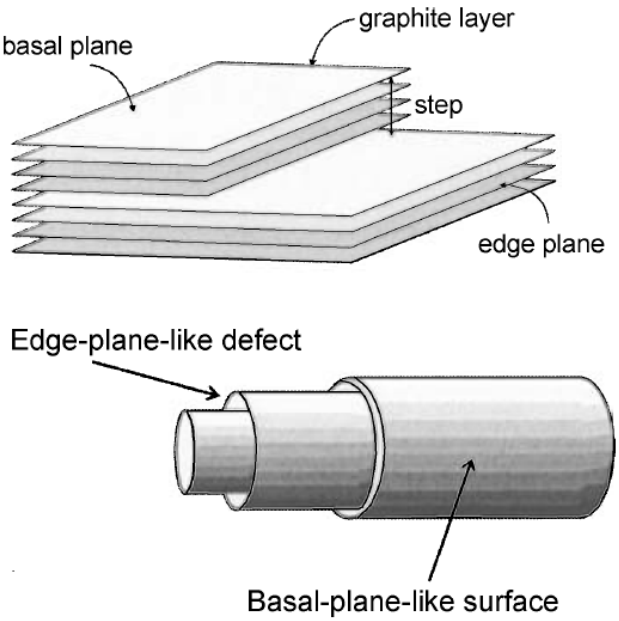

Figure 4.3 Illustration of 'edge-plane-like' and 'basal-plane-like' features of MWNT analogous to graphite structure.

(Reprinted from reference 1 with permission from Springer)

It has been shown[19] that the edge-plane is more active for electron transfer reactions than basal-plane using a quasi-reversible system, 1mM ferrocyanide in 0.1M aqueous KCl solution. Figure 4.4 shows the cyclic voltammogram of 1mM ferrocyanide in 0.1M aqueous KCl solution on various substrates: edge-plane pyrolytic graphite (EPPG), basal-plane pyrolytic graphite(BPPG) and MWNT immobilized on BPPG. The peak current of oxidation or reduction of the solution species is comparable for EPPG and MWNT

immobilized on BPPG. But, on the BPPG surface the peak current is very much smaller, implying that the catalytic activity of MWNT arises from the ends of the MWNT which resembles the edge-plane pyrolytic graphite.

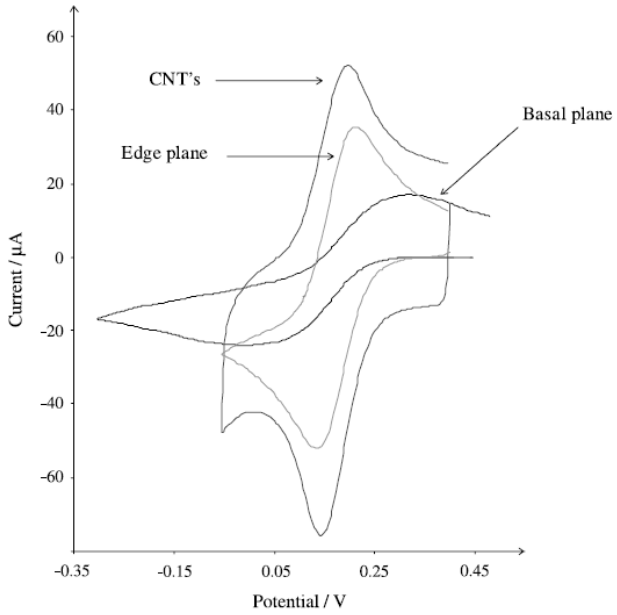

Figure 4.4 The overlaid electrochemical response of EPPG, BPPG and MWNTs abrasively immobilised on a BPPG electrode to 1mM ferrocyanide in 0.1M aqueous KCl solution.

(Reprinted from reference 19 with permission from the Royal Society of Chemistry)

4.2 Experimental Processes :

4.2.1 Functionalization of MWNT:

MWNT were purchased from Nanolabs, Inc. MWNT were made hydrophilic by refluxing 10mg MWNT in 20mL of a 1:1 (v/v) mixture of conc. sulfuric acid and conc. nitric acid with vigorous stirring at 80°C for a specific duration (30 min, 1 hr, 5 hrs or 7 hrs)[20]. After cooling, the treated MWNT suspension was diluted about 50 times with Millipore water and kept stagnant overnight. The MWNT settled down at the bottom of

the container. Then it was filtered through a 0.2 micron Teflon membrane filter and washed with Millipore water until the filtrate reached a pH of 7. The residue was then vacuum dried at room temperature. Hereafter the Acid-Treated MWNT will be denoted as AT-MWNT.

4.2.2 POM or Co^{2+} Treated AT-MWNT:

Ten (10) mg POM (Co-Dawson or lacunary Dawson) or equivalent Co^{2+} (source is $CoCl_2$) and 5mg AT-MWNT were sonicated in 10mL of Millipore water for 12 hr[16]. The MWNT-POM adduct or the MWNT-Co^{2+} adduct were then filtered through a 0.2 micron Teflon membrane filter and washed with plenty of Millipore water and vacuum dried at room temperature.

4.2.3 Characterization Techniques:

Raman Microscopy: Raman scattering was excited using the 514 nm output (ca. 20 mW) from an air-cooled argon ion laser (model 163-C42, Spectra-Physics Lasers, Inc.). Raman spectra were collected and analyzed using a Renishaw InVia Raman microscope system and associated software.

Scanning Electron Microscopy (SEM) and Energy Dispersive X-ray Spectroscopy(EDS): SEM images were collected using a JEOL JSM-7000F field-emission scanning electron microscope and analyzed using the EOS 7000F software package. EDX data were acquired using an Oxford X-Max energy dispersive X-ray spectrometer and were analyzed using the INCA software package.

4.2.4 Electrode Preparation:

Glassy Carbon was used as the substrate, Pt as the counter electrode, and Ag/AgCl as the reference electrode. All potential values were reported against the Ag/AgCl

electrode. The GC electrode was mechanically polished sequentially with 15 micron, 3 micron, and 1 micron diamond suspensions and 0.05 micron alumina paste. Each polishing step was followed by sonicating the electrode in Millipore water, methanol and again in Millipore water, each for 2 minutes. Finally, the electrode was washed with Millipore water. Next the GC electrode potential was cycled between -1000mV and 1500mV in 0.5M sulfuric acid and then an oxidizing potential of 1250mV was applied on the electrode in 1M NaOH for 5 min to remove any organic impurities from the electrode surface. The electrocatalyst was then loaded on the clean GC substrate.

AT-MWNT (0.2 mg) or its adduct with POM or Co^{2+} was dispersed in 500 µL of Millipore water by sonication. Nafion (5wt% solution in ethanol from Sigma-Aldrich) was added to the above dispersion to a final concentration of 0.1wt%. 5 µl or 20µl from this dispersion was loaded on GC substrate with an area of 0.07 cm^2(stationary electrode) or 0.28 cm^2 (Rotating Disc Electrode), respectively, and dried for at least 3 hrs under ambient conditions.

4.2.5 Oxygen Reduction Reaction (ORR) Activity Measurements:

The prepared electrode was tested for ORR in oxygen saturated 0.1M $HClO_4$ by cyclic voltammetry using Pt mesh as counter electrode and Ag/AgCl(sat) as reference electrode. Control experiments were conducted by repeating the above in the absence of oxygen in the supporting electrolyte. The electrochemical circuit was controlled using a BAS Epsilon electrochemical workstation.

4.3 Results and Discussion:

4.3.1 Optimization of Acid Treatment:

The acid treatment for functionalizing groups at the end of the MWNT is shown in Figure 4.5. The purpose of the acid treatment is to bring hydrophilic functional groups such as –COOH, $-SO_3H$ at the end of the MWNT. This will make the MWNT water dispersible. First, the time for MWNT was optimized to achieve good dispersing ability, good electrocatalytic activity, and good electrical conductivity. MWNT was treated in acid for varying times: 30 min, 1 hr, 5 hrs or 7 hrs. In the 30 min treated MWNT not enough functional groups were formed and so that was not dispersible in water. In the 7-hr treated MWNT, too long acid treatment resulted in the surface structure disruption. So, the MWNT film electrode conductivity decreased resulting in low kinetic current. The 1-hr and the 5-hr treated MWNT showed optimum performance. So, 5-hr treated MWNT was used for further studies.

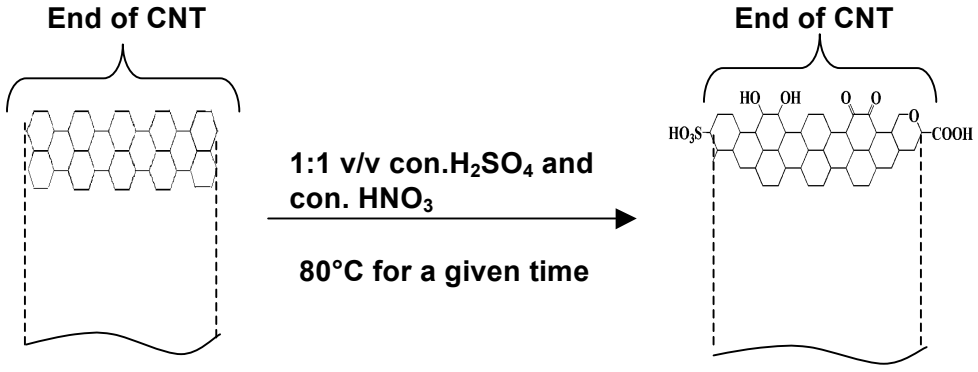

Figure 4.5 Acid treatment of MWNT for functionalization. In the acid treated MWNT (given on the right side of the arrow) both oxidized and reduced forms of quinone were given to show the important stable states of the redox functional groups on MWNT.

4.3.2 Characterization of Prepared AT-MWNT and its Co-Dawson Adduct:

(i) Raman Spectra:

Figure 4.6 shows the Raman spectra of AT-MWNT and its Co-Dawson adduct. The peak at 1350 cm^{-1} is called D-band and it corresponds to the defects in the CNT[21]. This peak position is the same for both AT-MWNT and its Co-Dawson adduct. The peak centered at around 1600 cm^{-1} is called T-band or G-band and it corresponds to the tangential modes of the carbon atoms arranged hexagonally in the graphene rolls of CNT[21]. It has two peaks because of the movement of the carbon atoms along the tube axis (higher wave number) and along the tube circumference (lower wave number)[22]. The G-band at lower wave number red shifted in AT-MWNT-Co-Dawson adduct compared to AT-MWNT by 5 cm^{-1}. It indicates the modification of AT-MWNT by Co-Dawson treatment.

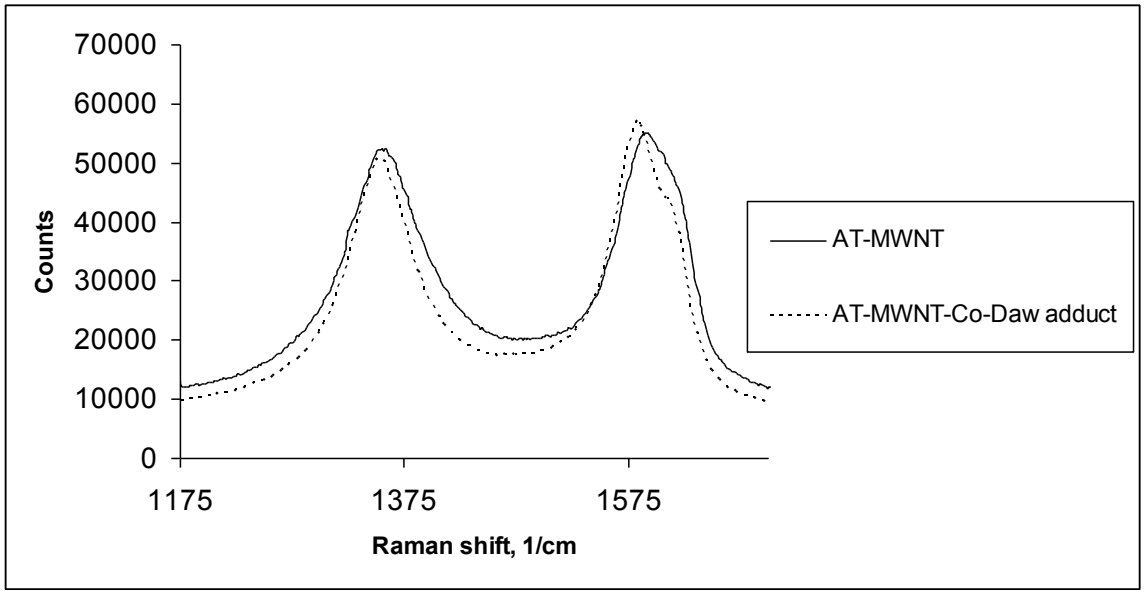

Figure 4.6 Raman spectra of AT-MWNT and AT-MWNT-Co-Dawson adduct

Model curve fitting for Raman spectra of AT-MWNT-Co-Dawson adduct using OriginPro 8.5.1:

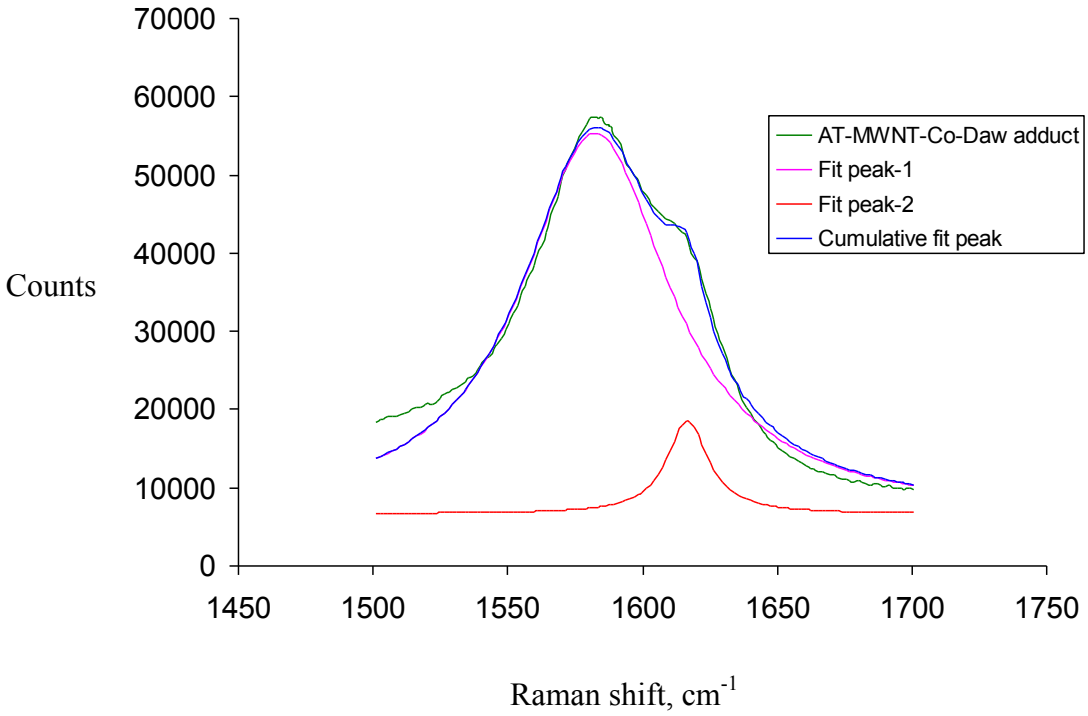

Raman Shift in cm^{-1}:

AT-MWNT	1350	1588	1618
AT-MWNT-Co-Daw	1349	1583	1617

(ii) Scanning Electron Microscopy (SEM) and Energy Dispersive X-Ray Spectroscopy (EDX):

Figure 4.7a shows the SEM obtained from the AT-MWNT- Co-Dawson adduct. The MWNTs have maintained their nanostructure after the heat treatment for 5 hrs in the mixture of 1:1 conc. sulfuric acid and conc. nitric acid and 12hr sonication. Figure 4.7b shows the EDS obtained from the MWNT and the AT-MWNT-Co-Dawson adduct. Fe

and S signals in MWNT are from the FeS catalyst used to grow the MWNT. These catalyst particles are inside the nanotubes and are not accessible to the solution (information from the Nanolabs, Inc. technical support). AT-MWNT-Co-Dawson adduct has W, Co and K signals in addition to Fe and S signals. It confirms the formation of AT-MWNT-Co-Dawson adduct.

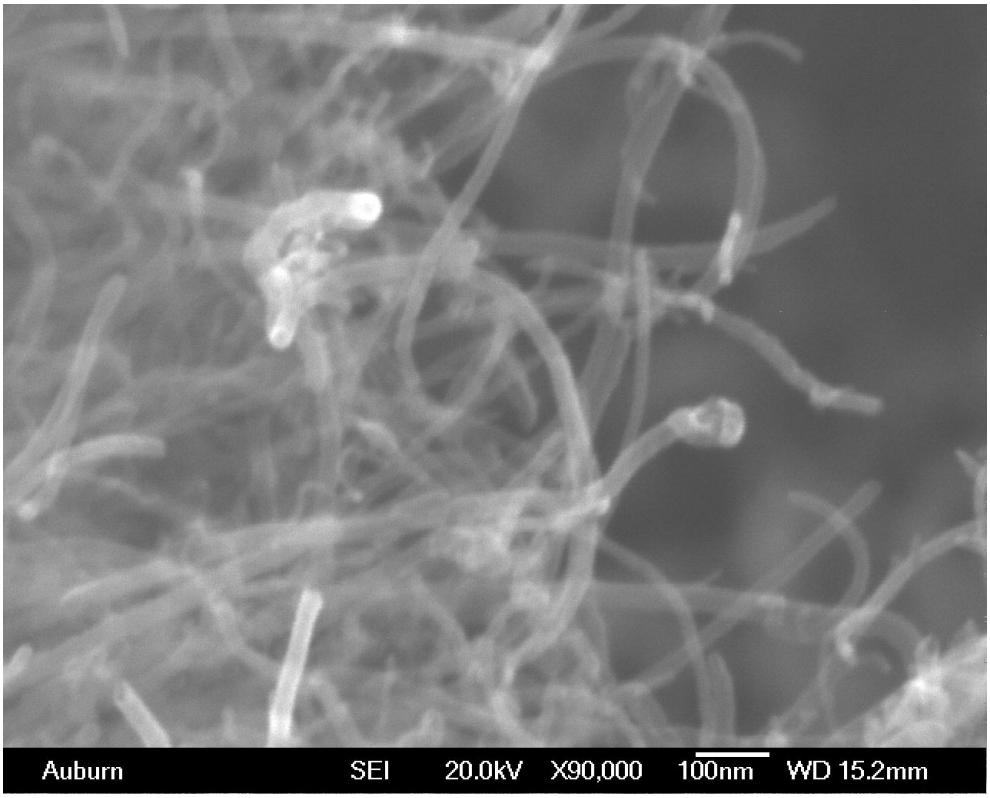

Figure 4.7a SEM image of AT-MWNT-Co-Dawson adduct

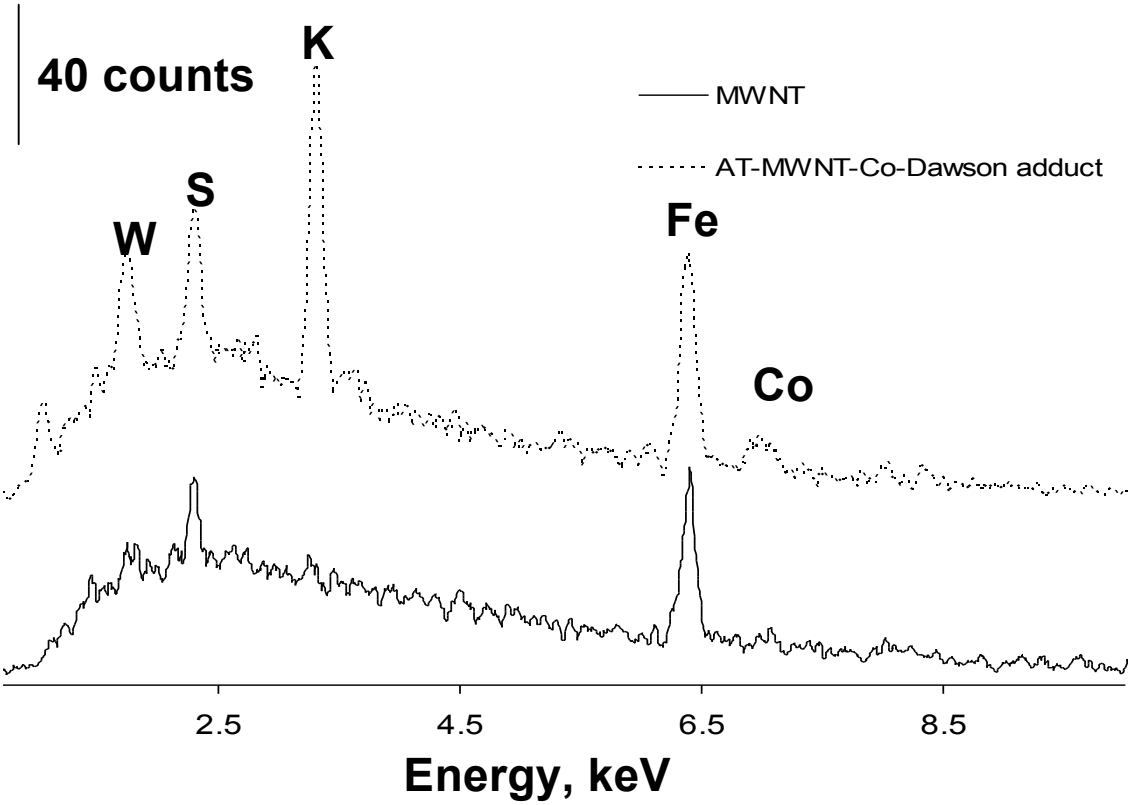

Figure 4.7b EDS of MWNT and AT-MWNT-Co-Dawson adduct

4.3.3 Electrocatalytic Activity towards ORR:

Figure 4.8 shows the results obtained on ORR activity of the AT-MWNT and the AT-MWNT-Co-Dawson adduct. The $E_{1/2}$ potential on the ORR polarization curve has been shifted by about 200mV from bare GC to AT-MWNT /GC and this 200mV positive shift can be attributed to the redox mediating activity of the quinone groups at the ends of the AT-MWNT for the oxygen reduction reaction[20]. Co-Dawson treatment on AT-MWNT makes another ~ 200mV positive shift in the $E_{1/2}$ potential on the ORR polarization curve.

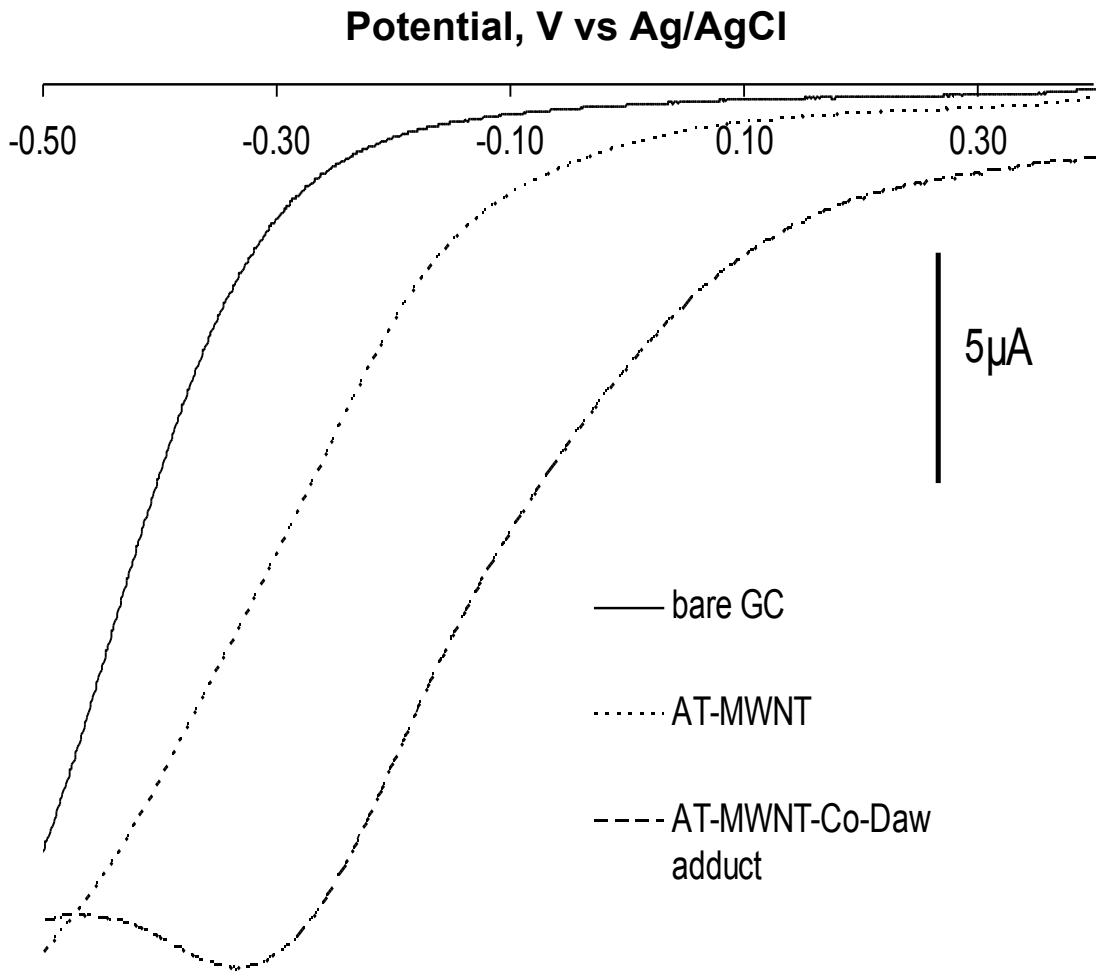

Figure 4.8 Comparison of the ORR polarization curves: The solid line represents the oxygen reduction wave for pure GC, dotted line represents AT-MWNT/GC and dashed line represents AT-MWNT-Co-Dawson adduct/GC in oxygen saturated 0.1M $HClO_4$. Scan rate 10mV/sec, GC electrode area: 0.07cm^2

Then rotating disc electrode (RDE) experiments[23] were carried out to obtain the kinetic parameters such as the kinetic current, i_K, and the number of electrons transferred per oxygen molecule, n. Figure 4.9 shows the ORR voltammograms obtained at various

electrode rotation speeds for AT-MWNT. The kinetic current, i_K, and the number of electrons transferred per oxygen molecule, n, can be calculated from the Koutecky-Levich plot made by plotting the inverse of the ORR limiting current versus the square root of the electrode rotation speed obtained from the RDE experiment. The Levich Equation (Eqn. 4.1) correlates the mass transfer limiting current, i_l, and the electrode rotation speed, ω, as follows:

$$i_l = 0.62nFAD_o^{2/3}\omega^{1/2}\nu^{-1/6} C_o^* \quad (4.1)$$

Where the following abbreviations stand for each concept:

n - Number of electrons involved

F - Faraday's constant, C/mole

A - Geometrical Area of the electrode, cm^2

D_o - Diffusion co-efficient of the electroactive species, cm^2/s

ω - Rotational speed of the electrode in rad/s

ν - Kinematic viscosity of the electrolyte, cm^2/s

C_o^* - Concentration. of the electroactive species, $mole/cm^3$

The Koutecky-Levich Equation correlates the measured ORR current, i, to its kinetic current component, i_K, and the mass transfer limited current component, i_l, by the following relation:

$$i^{-1} = i_K^{-1} + i_l^{-1} \quad (4.2)$$

Where $i_K = nFAk(E) C_o^*$

k(E) - Rate constant as a function of overpotential, cm/s

Substituting Equation 4.1 in Equation 4.2 gives

$$i^{-1} = i_K^{-1} + (0.62nFAD_o^{2/3}\omega^{1/2}\nu^{-1/6}C_o^*)^{-1}$$

$$i^{-1} = i_K^{-1} + (0.62nFAD_o^{2/3}\nu^{-1/6}C_o^*)^{-1}\omega^{-1/2}$$

Taking $\omega^{-1/2}$ in the abscissa and i^{-1} in the ordinate gives a straight line with a slope given by $m= (0.62nFAD_o^{2/3}\nu^{-1/6}C_o^*)^{-1}$

so, $n= (0.62nFAD_o^{2/3}\nu^{-1/6}C_o^* m)^{-1}$

The inverse of y-intercept gives the kinetic current, i_K.

Figure 4.10 shows the Koutecky-Levich plot made for the ORR on the AT-MWNT. The similar experiments were repeated for the AT-MWNT-Co-Dawson and kinetic parameters were extracted from the Koutecky –Levich plot.

Table 4.1 shows that the kinetic current for the AT-MWNT-Co-Dawson adduct is 1.9 times higher than that for the AT-MWNT, even though there is no significant improvement in the number of electrons transferred due to the Co-Dawson treatment. The number of electrons transferred will be four if the oxygen is reduced directly to water and two if the reduction product is hydrogen peroxide. Complete reduction of oxygen to water is preferred in fuel cells as hydrogen peroxide can damage the polymer electrolyte membrane. For both AT-MWNT and its Co-Dawson adduct, n is around three, indicating that both four electron and two electron reduction of oxygen is occurring. But, on GC the oxygen reduction is predominantly via two electron transfer.

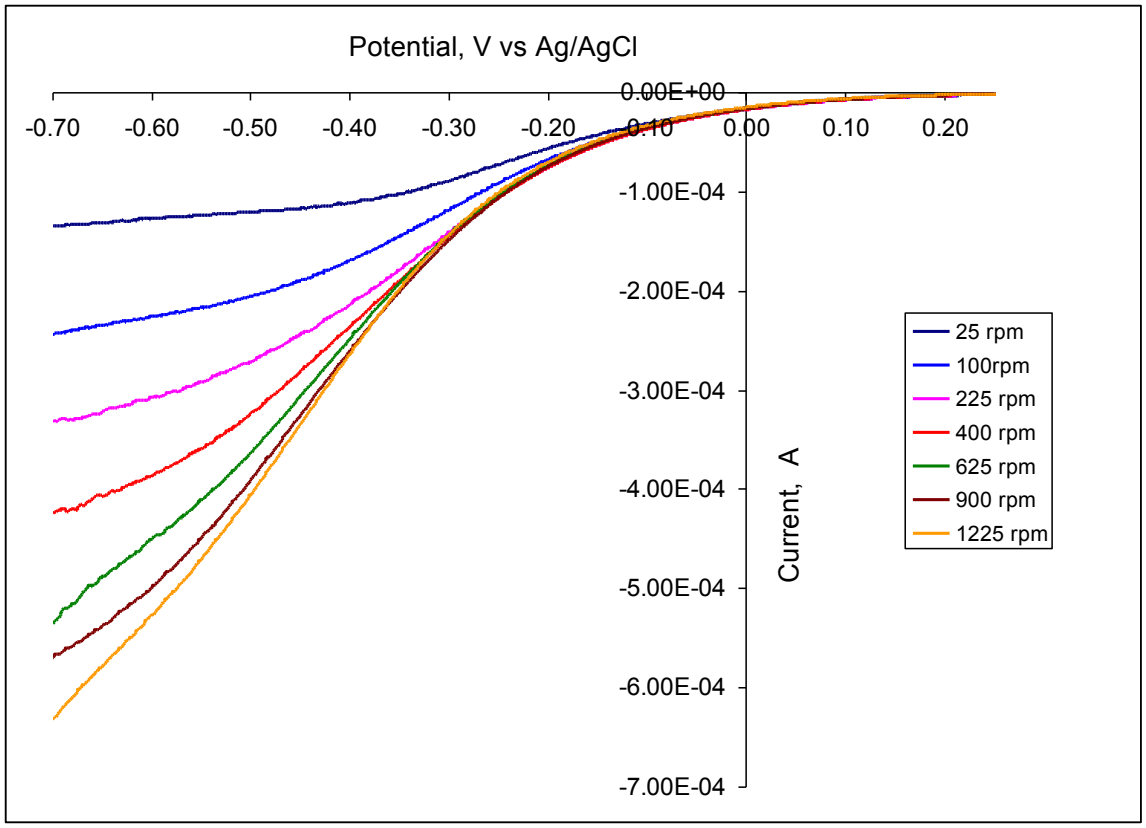

Figure: 4.9 ORR voltammogram at various electrode rotation speed for the GC electrode modified with AT-MWNT(5 hr treated in acid). Electrolyte: 0.1M $HClO_4$ saturated with O_2, scan rate:10mV/s, Electrode area = 0.28 cm^2

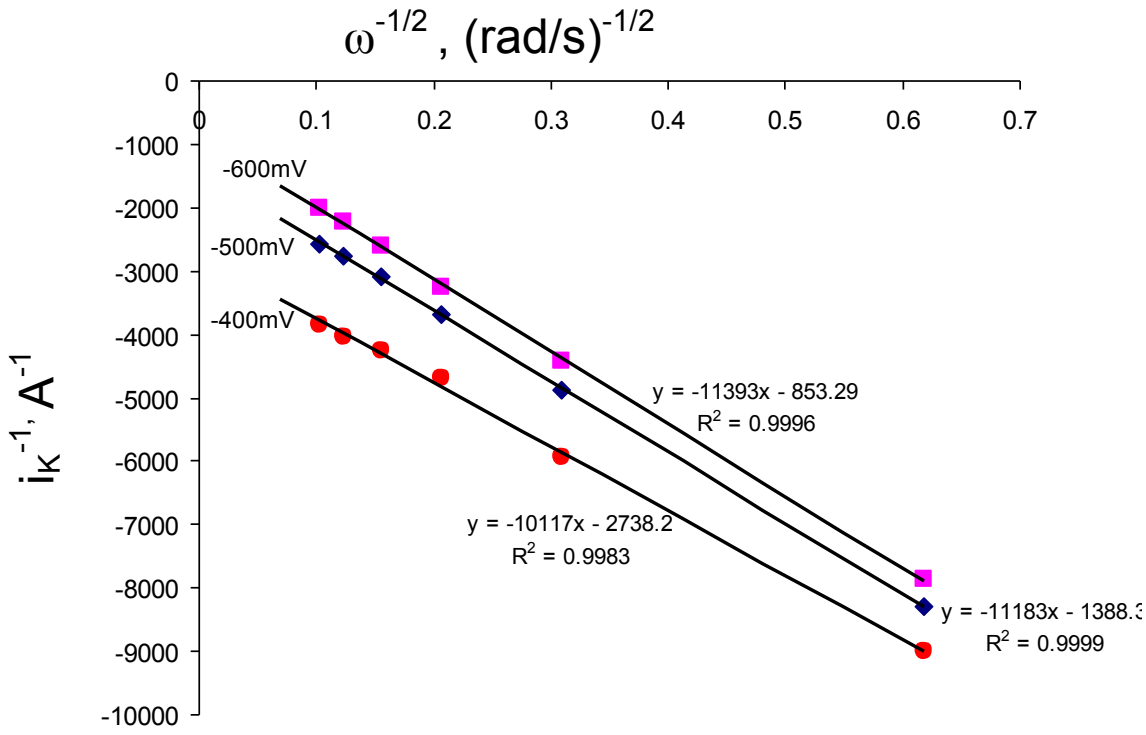

Figure 4.10 Koutecky-Levich plot made for ORR on AT-MWNT.

Table 4.1 ORR Kinetic parameters of AT-MWNT and AT-MWNT-Co-Dawson adduct obtained from Koutecky-Levich plot at -500mV vs Ag/AgCl:

	i_K, mA	n
AT-MWNT	0.72	2.8
AT-MWNT Co-Daw adduct	1.38	2.9

(Note: The number of electron transferred calculated here will not be accurate due to the internal resistance to oxygen diffusion in the MWNT film electrode caused by Nafion.)

The notable point here is that we couldn't observe the Co-Dawson redox activity in the cyclic voltammogram of the AT-MWNT-Co-Dawson adduct in the absence of oxygen. It indicates that Co-Dawson might have decomposed during the 12 hr sonication period with AT-MWNT and the decomposed products on the AT-MWNT surface act as the catalyst. To check whether this is true, AT-MWNT-Co-Dawson adduct with only 30 minute sonication was prepared and mixed with 0.1wt% Nafion and loaded on GC and tested for ORR. Figure 4.11 compares the ORR activity of 30-minute sonicated AT-MWNT-Co-Dawson adduct and AT-MWNT. The material resulting from 30-min treatment of AT-MWNT with Co-Dawson shows Co-Dawson redox peaks in the absence of oxygen, but its ORR activity is worse than that of AT-MWNT. There is no improvement due to the addition of Co-Dawson.

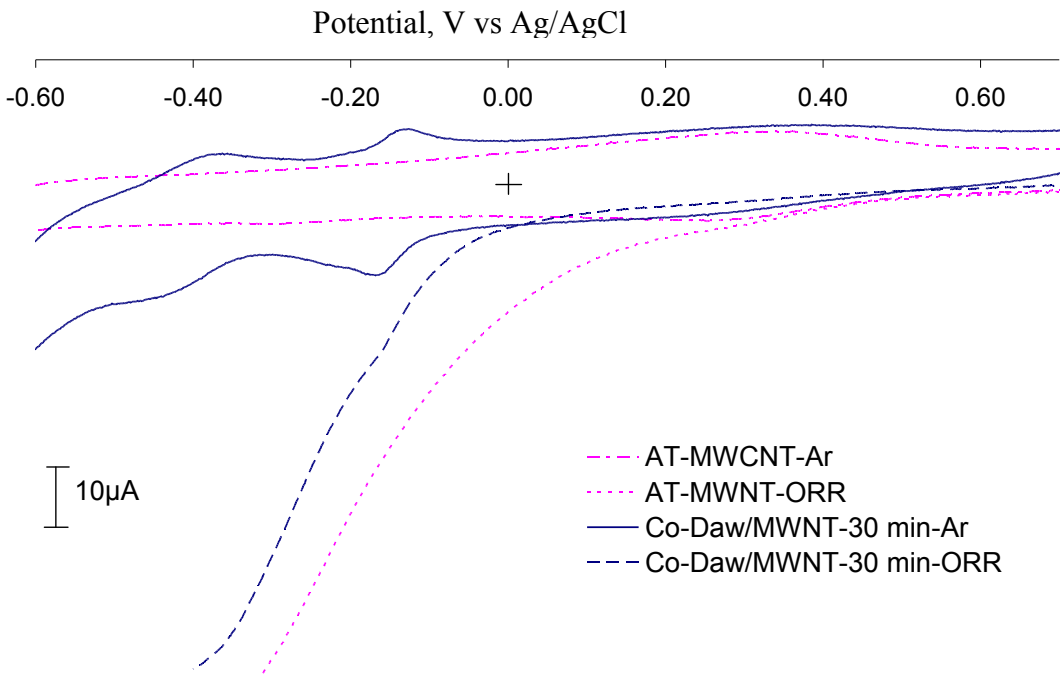

Figure 4.11 ORR on AT-MWNT and 30-min sonicated AT-MWNT-Co-Dawson adduct. Electrolyte:O_2 saturated 0.1M $HClO_4$, Scan rate 10mV/sec, GC electrode area: 0.28cm^2

To probe whether any new species has been formed from the Co-Dawson during the 12-hr sonication period, aq. Co-Dawson was sonicated for 12 hrs and its Raman spectrum was recorded before and after sonication. In Figure 4.12, the aq. Co-Dawson, both fresh and 12-hr sonicated, has two peaks, one at 970 cm^{-1} from the terminal W-O stretching mode of Co-Dawson and the other at 1640 cm^{-1} from water. The peak intensity for Co-Dawson at 970 cm^{-1} was reduced about 30% in the 12 hr treated one compared to the freshly prepared one. This implies that only a minor portion of Co-Dawson solution species decomposes during 12 hr sonication when Co-Dawson alone is sonicated. Also, the 12-hr sonicated Co-Dawson shows fluorescence whereas the freshly prepared Co-Dawson did not. The fluorescence may come from the decomposed product. To check whether the fluorescing species is aq. Co^{2+}, the Raman spectrum of equivalent aq. $CoCl_2$ was recorded. Aq. $CoCl_2$ didn't show any fluorescence. This indicates that the fluorescing species might be the decomposed part of Co-Dawson, not just Co^{2+}. The absence of Co-Dawson redox peaks in the electrochemistry of AT-MWNT-Co-Dawson adduct indicates that addition of AT-MWNT may enhance the decomposition of Co-Dawson by surface reactions.

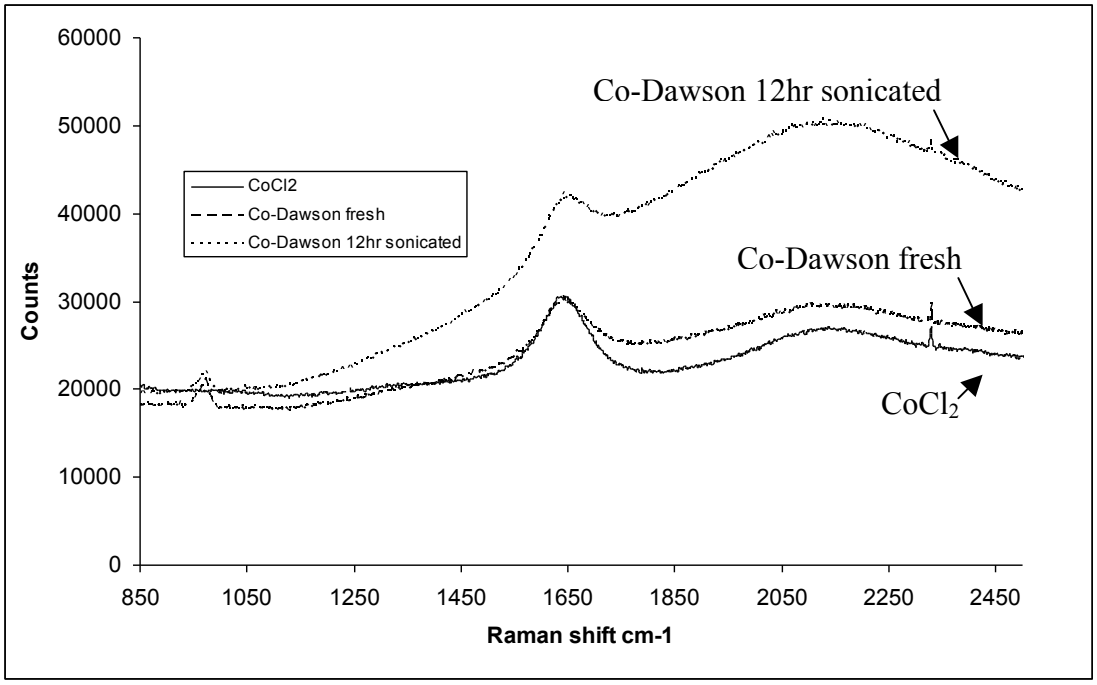

Figure 4.12 Raman spectra of aq. $CoCl_2$ and aq. Co-Dawson. Aq. $CoCl_2$ (solid line), aq. Co-Dawson Fresh (dashed line) and Co-Dawson 12hr sonicated (dotted line)

To probe whether Co^{2+} , tungstate framework, or Co containing tungstate framework is responsible for the improved activity of AT-MWNT-Co-Dawson adduct, the AT-MWNT was sonicated in Co^{2+} and in lacunary Dawson separately for 12hrs and tested for ORR (See Figure 4.13). Figure 4.13 shows that the ORR electrocatalytic activity of the AT-MWNT-Co-Dawson adduct may be attributed to both tungsten units and Co^{2+} ions adsorbed on the surface on AT-MWNT.

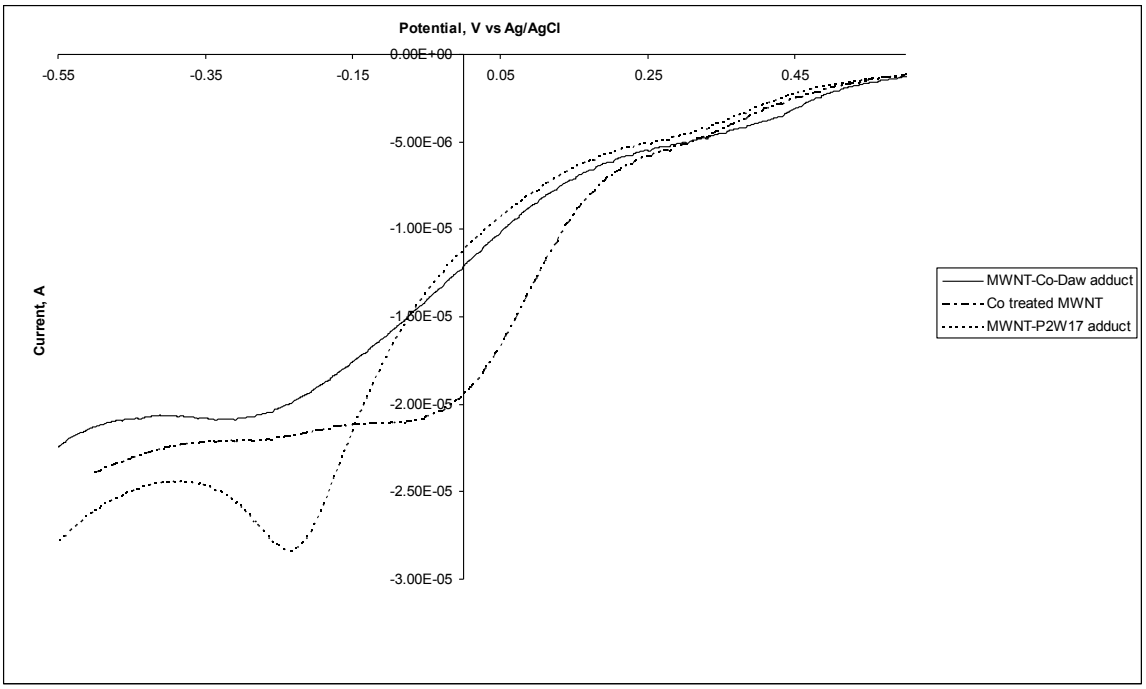

Figure 4.13 ORR polarization curves of Co(II) ions and lacunary Dawson treated AT-MWNT. Electrolyte: oxygen saturated 0.1M $HClO_4$, Scan rate:10mV/sec, GC electrode area: 0.07cm^2

4.4 Conclusion:

We successfully made an improved catalyst by sonicating Co-Dawson with acid treated MWNT. The treatment (12hr sonication) with Co-Dawson has doubled the ORR kinetic current of AT-MWNT. But, the absence of Co-Dawson redox peaks under deoxygenated condition in the MWNT-Co-Dawson adduct made by 12 hr sonication implied that Co-Dawson could be decomposed during sonication with AT-MWNT. A similar observation was made by Finke et al.[24] during their studies on benzene hydrogenation to cyclohexane using a Ru(II) containing complex, Ru(II)-(η^6-C_6Me_6)$(OAc)_2$, as the homogenous catalyst. Ru(II) was reduced to Ru metal during the catalytic process and acted as the true catalyst where as the Ru(II) complex was proved to

be catalytically inactive for the intended system. Lined up with Finke's work, this study on MWNT-Co-Dawson is an example where the true catalyst, rather than the intended one, may form during the catalyst preparation or the catalytic process and whose catalytic performance may exceed that of the intended one. However, the true catalyst could be identified through the experimental observations.

References:

(1) Wildgoose, G. G.; Banks, C. E.; Leventis, H. C.; Compton, R.G. *Microchim Acta* **2006**, *152*, 187–214.

(2) Merkoci, A. *Microchim Acta* **2006**, *152*, 157–174.

(3) Khare, R.; Bose, S. *Journal of Minerals & Materials Characterization & Engineering* **2005**, *4*, 31-46.

(4) Cai, C.; Chen, J. *Anal. Biochem.* **2004**, *332*, 75.

(5) Salimi, A.; Noorbakhsh, A.;Ghadermarz, M. *Analytical Biochemistry* **2005**, *344*, 16–24.

(6) Kim, B.; Sigmund, W. M. *Langmuir* **2004,** *20,* 8239-8242.

(7) Ismaili, H.; Lagugne-Labarthet, F.; Workentin, M. S. *Chem. Mater.* **2011**, *23*, 1519–1525.

(8) Lu, W.; Li, N.; Bao, S.; Chen, W.; Yao, Y. *Carbon* **2011,** *49*, 1699–1709.

(9) Siswana, M.; Ozoemena, K. I.; Nyokong, T. *Sensors* **2008**, *8*, 5096-5105.

(10) Vernon, D. R.; Meng, F.; Dec, S. F.; Williamson, D. L.; Turner, J. A.; Herring, A. M. *J. Power Sources* **2005**, *139*, 141-151.

(11) Khenkin, A. M.; Weiner, L.; Wang, Y.; Neumann, R. *J. Am. Chem. Soc.* **2001**, *123*, 8531-8542.

(12) Keita, B.; Nadjo, L. *J. Electroanal. Chem.* **1987**, *217*, 287-304.

(13) Kuhn, A.; Anson, F. C. *Langmuir* **1996**, *12*, 5481-5488.

(14) Karina Cuentas-Gallegos, A.;Martínez-Rosales, R.; Rincón, M. E.; Hirata, G. A.; Orozco, G. *Optical Materials* **2006**, *29*, 126–133.

(15) Song, Y.; Wang, E.; Kang, Z.; Lan, Y..; Tian, C. *Materials Research Bulletin* **2007**, *42*, 1485–1491.

(16) Pan, D.; Chen, J.; Tao, W.; Nie, L.; Yao, S. *Langmuir* **2006,** *22,* 5872-5876.

(17) Tang, Q.; Luo, X.; Wen, R. *Analytical Letters* **2005**, *38*, 1445–1456.

(18) Qu, J.; Shen, Y.; Qu, X.; Dong, S. *Electroanalysis* **2004**, *16*, 1444-1450.

(19) Banks, C. E., Davies, T. J.,Wildgoose, G. G., Compton, R. G. *Chem. Commun.* **2005,** *7*, 829-841.

(20) Jurmann, G.; Tammeveski, K. *J. Electroanal. Chem.* **2006**, *597*, 119–126.

(21) Zhang, H.; Lin, G.; Zhou, Z.; Dong, X.; Chen, T. *Carbon* **2002**, *40*, 2429–2436.

(22) Jorio A, Pimenta M, Souza-Filho A, Saito R, Dresselhaus G, Dresselhaus M. *New J Phys.* **2003**, *5*, 139.1-139.17

(23) Bard, A. J.; Faulkner, L. R. Electrochemical Methods Fundamentals and Applications, 2nd Ed. John Wiley & Sons, Inc.

(24) Widegren,J. A.; Bennett, M. A.; Finke, R. G. *J. Am. Chem. Soc.* **2003**, *125*, 10301-10310.

Chapter 5

DISPLAY OF SOLID-STATE MATERIALS USING BIPOLAR ELECTROCHEMISTRY

5.1 Introduction:

Over the past 15 years, combinatorial and high throughput techniques have been adapted to the discovery of new solid-state materials[1]. Thin films with a spatially resolved variation of chemical composition can be deposited using vapor phase deposition (VPD) methods, although thermal and thickness gradients also can be used. Lithographic, printing, or microfluidic techniques can be employed to create one- or two-dimensional arrays in which each array element is chemically unique. A wide range of solid-state materials have been screened using these methods, including superconductors[2], dielectrics[3], ferromagnetics[4], luminescent materials[5], magnetoresistive compounds[6], polymers[7], and solid-state catalysts[8].

An electrically isolated conductor immersed in an electrolyte can act as a bipolar electrode, that is, as both an anode and a cathode, if a sufficiently large potential difference is applied across the solution using two "driving" electrodes. The applied voltage generates an interfacial potential difference that varies along the length of the conductor. If the electrolyte contains appropriate redox couples, faradaic reactions can occur at the electrode/ solution interface: reduction at the cathodic pole of the electrode and oxidation at the anodic pole.

Bipolar electrodes (BPEs) have been used for decades in industrial applications ranging from organic electrosynthesis to catalysis due to the reduced number of electrical connections and the lower power dissipation compared to conventional electrochemistry[9]. Recently, several novel applications of bipolar electrochemistry have been reported. Bjorefors and co-workers have studied the formation of chemically graded self-assembled organic monolayers on bipolar electrode surfaces[10]. In this work, a methoxy terminated SAM was selectively desorbed from the cathodic pole of a BPE and backfilled with a carboxyl terminated thiol to generate a chemical gradient. In 2001, Manz showed how a bipolar electrode could be used as an in situ wireless electrochemical detector in a lab-on-a-chip application[11]. Crooks and co-workers have adapted this concept as the basis of a novel biosensor platform for the detection of DNA[12]. Duval et al. have recently reported on the influence of bipolar faradaic depolarization on electrophoresis and electroosmosis in the context of electrokinetic measurements[13].In related work, Crooks and coworkers have studied the influence of a bipolar electrode on microfluidic separations[14].

Applications of bipolar electrochemistry in electrodeposition have also been reported. For instance, Bradley and co-workers demonstrated the growth of Cu wires between micrometer sized particles using bipolar electrochemistry[15]. These workers also studied the bipolar electrodeposition of palladium onto micrometer-scale particles, carbon nanotubes, and nanofibers[16].

Warakulwit et al. showed that asymmetric metal-modified carbon nanotubes could be generated in a capillary electrophoresis channel[17].

Herein, we report on the use of bipolar electrochemistry to generate a one-dimensional solid-state chemical composition gradient, using CdS as our paradigm case. Electrodeposited materials formed in this fashion were screened using Auger electron spectroscopy and confocal Raman microscopy. To our knowledge, reports of bipolar electrodeposition of compounds have not been previously published. However, in an experiment related to our own, Bohn and co-workers used unipolar electrochemistry to generate Cu gradients on very thin Au electrodes. The thin Au samples were immersed in a $CuSO_4$ containing electrolyte solution, and the two ends of the Au sample were connected to a bipotentiostat as the two working electrodes. The bipotentiostat was used to generate an in-plane potential gradient across the Au sample. A very abrupt Cu gradient was formed under these conditions[18].

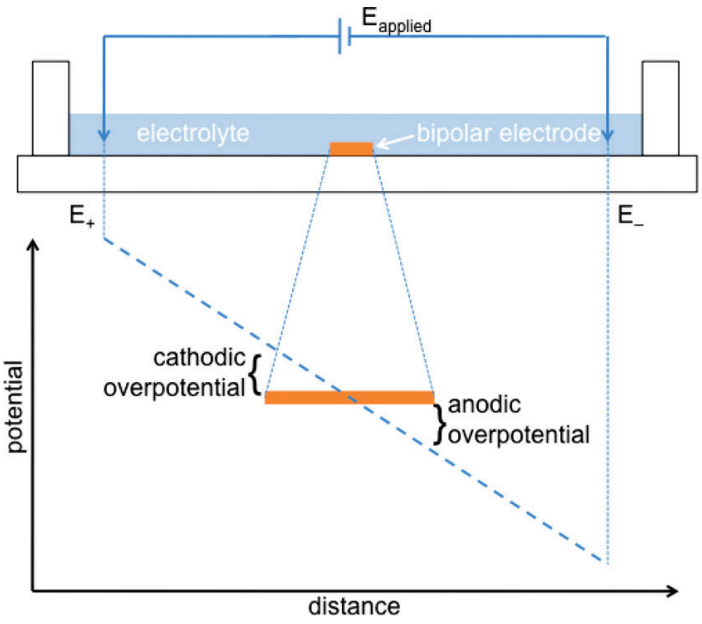

Scheme 5.1 Diagram of a Bipolar Electrochemical Cell, Showing the Electrode Geometry and the Origin of the Cathodic and Anodic Overpotentials.

A diagram of a bipolar electrochemical cell is shown in Scheme 5.1. In contrast to a conventional electrochemical cell, in which the potential of the working electrode is controlled relative to the potential of a reference half-cell using a potentiostat, the potential of a bipolar electrode is not controlled relative to a reference value and adjusts to the potential of the surrounding solution. Thus, the equilibrium potential of the BPE will lie somewhere between the anodic and cathodic limits of the solution as defined by the geometry of the driver electrodes and the potential applied between them. Levich described the potential distribution of a perfectly spherical bipolar particle immersed in an electrolyte in 1962[19]. In 1985, Pons et al.[20] treated the case of bipolar electrolysis of suspensions of spherical ultramicroelecrodes.

More recently, Duval et al.[21] provided a quantitative description of bipolar electrode behavior using a model based on mixed potentials and Butler-Volmer kinetics. According to this model, there will be a single position along the conductor where the potential of the bipolar electrode equals the potential of the solution (and where the driving force for reactions will equal zero). Everywhere else, there will be an overpotential due to the difference between the solution potential and the bipolar electrode potential. If the applied electric field is constant, there will be a variation of the overpotential along the length of the bipolar electrode. When anodic and cathodic processes occur, there will be a current flow through the bipolar electrode. The anodic and cathodic currents must be equal in magnitude because of conservation of charge. It will also be the case that the current will be larger at the ends of the BPE due to the larger value of the overpotential.

The electrodeposition of II-VI semiconductors is generally carried out at cathodic potentials, as exemplified by CdTe, which was first studied by Kroger and co-workers[22]. The II-VI semiconductors are a natural choice of materials system for our studies because the growth mechanism is well understood (in the case of unipolar electrodeposition) and has been found to be similar for most of the metal chalcogenides[23].

For the deposition of a single element, the current potential characteristic consists of a single wave whose amplitude is determined by the concentration of the elemental precursor in solution and the diffusion of this species to the electrode surface. Typically, the deposition of the chalcogenide, which in our experiments is S, occurs at much more positive potentials than the corresponding metal ion. The half-reaction for the deposition of S from thiosulfate solutions can be written formally as shown below. The expected current-voltage characteristic is shown in Scheme 5.2A.

$$5H^+ + HS_2O_3^- + 4e^- = 2S + 3H_2O \quad (E^\circ = +\ 0.45\ V) \quad (1)$$

The deposition of Cd from a solution of Cd^{2+} is given in Eqn. 2, and its electrochemical behavior is schematically illustrated in Scheme 5.2B.

$$Cd^{2+} + 2e^- = Cd \quad (E^\circ = -0.40\ V) \qquad (2)$$

When both the metal and chalcogenide precursors are present in the same solution, the electrochemical response is not simply the superposition of the two current voltage characteristics because the deposition of the semiconductor (i.e., CdS) can also take place according to the following reaction.

$$Cd^{2+} + 2e^- + S = CdS \qquad (3)$$

Under these experimental conditions, the Cd deposition potential will be shifted to more positive potentials by an amount proportional to the free energy of formation of

CdS ($\Delta E = \Delta G^0_f/2F$), which is 0.73 V[23]. Once an atom of S is deposited, the deposition of CdS in a 1:1 stoichiometric ratio is thermodynamically possible.

From these considerations, we expect that electrodeposition will occur in three distinct zones as the potential is made increasingly cathodic: deposition of elemental S, formation of CdS, and codeposition of Cd and CdS (see Scheme 5.2). In the case of bipolar electrodeposition, because of the distance-dependent variation of the interfacial potential difference, these three deposition zones should be directly displayed along the length of the BPE from the cathodic pole toward the center of the bipolar electrode.

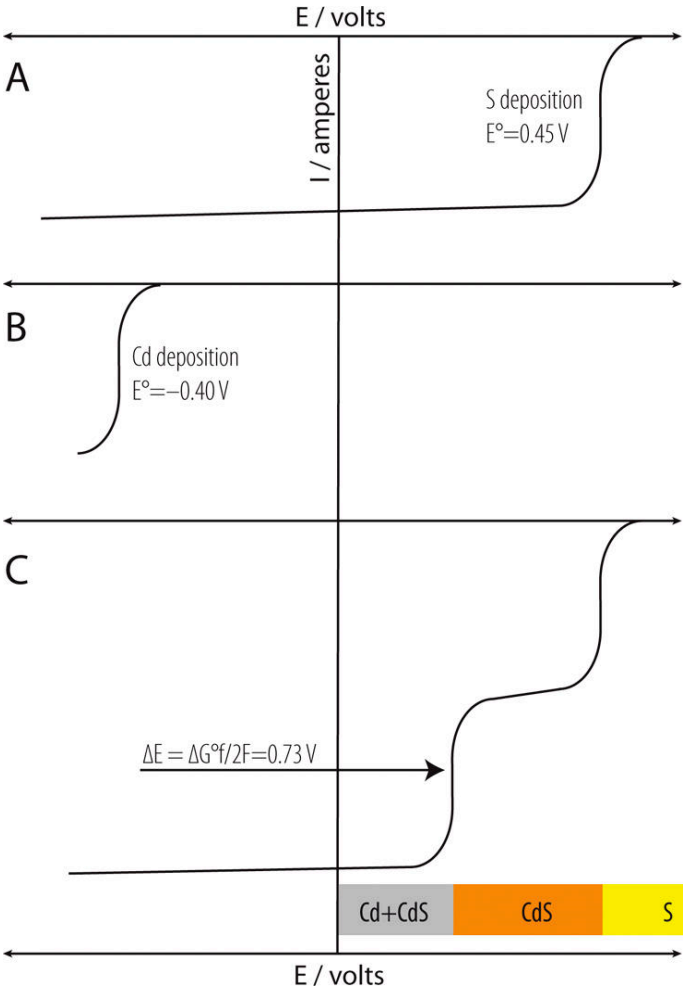

Scheme 5.2 (A) The expected current-potential response of a solution containing $S_2O_3^{2-}$. (B) The expected current-potential response of a solution containing Cd^{2+} . (C) The expected current-potential response of a solution containing a mixture of $S_2O_3^{2-}$ and Cd^{2+} showing conditions under which CdS can deposit. The predicted variation of chemical composition with applied potential is shown in the lower right portion of the frame.

5.2 Experimental Section:

Materials:

KNO_3, $CdSO_4$ (99%, Sigma-Aldrich), $Na_2S_2O_3$ (99%, Sigma-Aldrich), H_2O_2 (Fisher), and concentrated H_2SO_4 (Fisher) were used as received. Glassy carbon rods (6 mm diameter, SPI Supplies, Inc.) were used to fabricate the driver electrodes used for bipolar electrochemistry. The Au wire (1.0 mm diameter, 99.999% purity) used to make all bipolar electrodes was obtained from Alfa, Inc. Millipore-Q purified deionized (DI) water (18.2 MΩ.cm) was used to make up all solutions and to rinse electrodes.

Substrate Preparation:

Au wire electrodes were cleaned by rinsing sequentially with distilled water, absolute ethanol, piranha solution (1:3 v/v 30% H_2O_2, 18M H_2SO_4), and distilled water. After being dried in a stream of flowing nitrogen, the clean Au wire was placed into the electrochemical cell. Glassy carbon driver electrodes were prepared by rinsing sequentially with distilled water, absolute ethanol, and distilled water and were dried in a stream of flowing nitrogen.

Electrochemistry:

All bipolar electrochemistry experiments were performed in a home-built single compartment glass cell (ca. 15 mL total volume) using a Hewlett-Packard model 6010 regulated DC power supply to control the potential applied between two glassy carbon driver electrodes separated by 2.0 cm. The electrically floating Au bipolar electrode (BPE) was placed symmetrically between the two driver electrodes. After immersing the three electrodes in the electrodeposition solution, a voltage of 8.5 V (empirically determined to be optimum) was applied across the driver electrodes. This potential was

maintained for a few seconds, until visual inspection of the BPE indicated the formation of an electrodeposited film. The BPE was then rinsed with DI water, dried in a stream of flowing nitrogen, and placed in a covered container prior to analysis using Auger electron spectroscopy and Raman microscopy.

Auger Electron Spectroscopy (AES):

The AES system was a PHI 3017 Auger spectrometer equipped with a cylindrical mirror analyzer (CMA). Specimens were mounted into the AES system with no additional pretreatment or special handling. They were attached to the AES sample mount using double-sided C tape. Survey spectra on the as-received surfaces were then collected, without Ar^+ sputter cleaning.

Raman Microscopy:

Raman scattering was excited using the 514 nm output (ca. 20 mW) from an air-cooled argon ion laser (model 163-C42, Spectra-Physics Lasers, Inc.). Raman spectra were collected and analyzed using a Renishaw InVia Raman microscope system and associated software.

5.3 Results and Discussion:

To carry out the bipolar electrodeposition (BP-ED) of CdS, a glass cell ca. 3.0 cm long by ca. 1.5 cm wide was filled with approximately 10 mL of 0.10 M KNO_3 supporting electrolyte containing 0.02 M $CdSO_4$ and 0.05 M $S_2O_3^{2-}$. In all experiments, the pH of the electrolyte was adjusted to ca. 3.0 using sulfuric acid. Two glassy carbon driver electrodes were immersed in the electrolyte with a separation distance of 2.0 cm. Glassy carbon was used because hydrogen evolution from the acidic electrolyte was found to be less of a problem than when using a metal driver electrode such as Pt or Au.

A BPE consisting of a 1.7 cm long, 1.0 mm diameter Au wire was placed symmetrically between the two driver electrodes as schematically illustrated in Scheme 5.1. A wire was used instead of a foil to minimize edge effects caused by variations in the interfacial potential that are expected to arise at abrupt interfaces. Next, a voltage of 8.5 V was applied across the driver electrodes using a DC power supply. This potential was applied until visual inspection of the BPE indicated the formation of an electrodeposited film (typically a few seconds).

Three distinct regions of electrodeposition along the principal axis of the BPE were identified by visual inspection. The region of the BPE closest to the cathodic pole appeared silver/gray in color. In contrast, the part of the electrodeposit closest to the center of the BPE appeared pale yellow, suggesting a S-rich deposit in this region. The central region of the electrodeposit appeared orange, consistent with the formation of CdS. Scanning electron microscopy data show that the electrodeposit is conformal with the underlying polycrystalline Au BPE surface (see the Supporting Information). The chemical composition of the electrodeposit as a function of lateral position along the BPE was studied using Auger electron spectroscopy (AES) and confocal Raman microscopy.

The geometry used for the analysis locations is shown in Figure 5.1A. Seven Auger electron spectra were taken sequentially along the principal axis of the electrode, at positions 500 μm apart. In Figure 5.1B, we plot the AES atomic percentage of Cd and S as a function of lateral position along the BPE. Three electrodeposition zones are evident from this data. (i) Near the cathodic pole of the BPE, the CdS deposit is Cd-rich, consistent with the gray/silver appearance of the electrode in this region (point 1). (ii) At the anodic limit of the deposit, near the center of the BPE, the deposit consists

predominantly of elemental S, which is also consistent with the observed color of the deposit (point 7). (iii) Between these two limits, that is, near the center of the deposit, the material is nearly stoichiometric CdS, consistent with the observed orange color in this zone (points 2-6). It should be noted that Au was rarely observed in the AES data owing to good coverage of CdS.

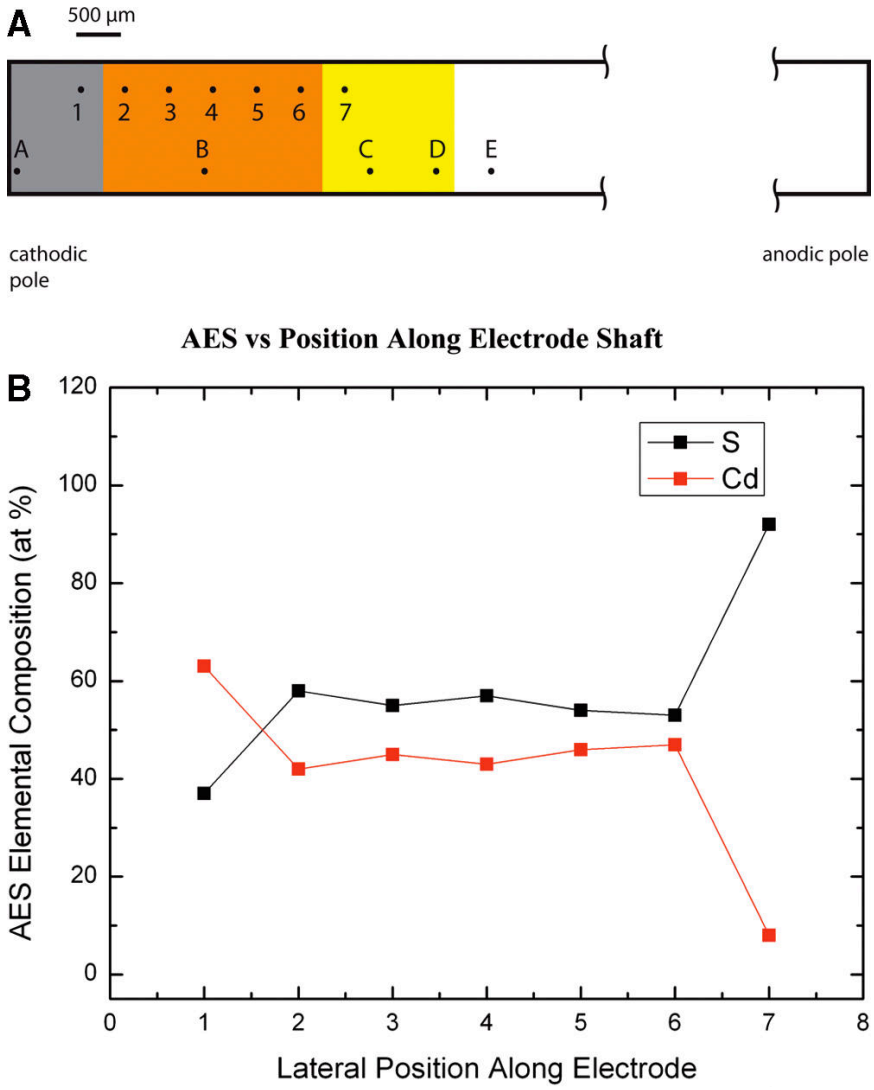

Figure 5.1 (A) Diagram of the geometry used for AES and Raman analysis. (B) Plot of the AES atomic percentage of Cd and S as a function of lateral position along the BPE.

Representative Raman spectra, collected using an excitation wavelength of 514 nm, are presented in Figure 5.2. The spectra consist of two main peaks, which are assigned as the CdS longitudinal optical (LO) phonon band at ca. 300 cm^{-1} and its overtone at ca. 600 cm^{-1}. As shown in spectrum E, no CdS Raman scattering is observed at the anodic limit of the deposited film, consistent with our AES measurements (i.e., point 7). Moving toward the cathodic pole, weak Raman scattering consistent with the formation of CdS can be observed (spectrum D). Closer to the cathodic pole of the BPE, where the Raman scattering is more intense, three distinct zones can clearly be identified. (i) In the vicinity of the cathodic pole, intense CdS phonon bands are clearly seen. Spectrum B is representative of the data collected in this region of the BPE. Additional spectra acquired from this region showed less than 5% variation of the LO phonon intensity from point-to-point (data not shown). The nearly constant LO phonon intensity in this deposition zone is consistent with the formation of stoichiometric CdS. (ii) Near the physical edge of the cathodic pole (spectrum A), the intensity of the Raman bands drops precipitously. We suspect that this is due to a second faradaic process, such as hydrogen evolution, occurring in parallel with the CdS electrodeposition reaction owing to the higher overpotential at this location. (iii) Raman spectra obtained at points closer to the center of the BPE are characterized by weaker CdS Raman scattering as well as by the appearance of a broad spectroscopic feature centered at about 420 cm^{-1} (spectrum C). The origin of this feature has been assigned by previous researchers as photoluminescence (PL) originating from defects within the electrodeposited CdS film[24]. These workers attributed the observed PL to the recombination of an electron trapped in a sulfur vacancy with a hole in the CdS valence band. Furthermore, the PL intensity was

found to be a function of the S/Cd molar ratio. Taken together, the qualitative observations regarding the apparent color of the films as well as quantitative AES spectroscopy and Raman microscopy measurements all support the predictions made earlier on the basis of simple thermochemical arguments regarding the display of CdS deposition zones along the length of the BPE owing to the variation of interfacial potential along its length under an applied electric field.

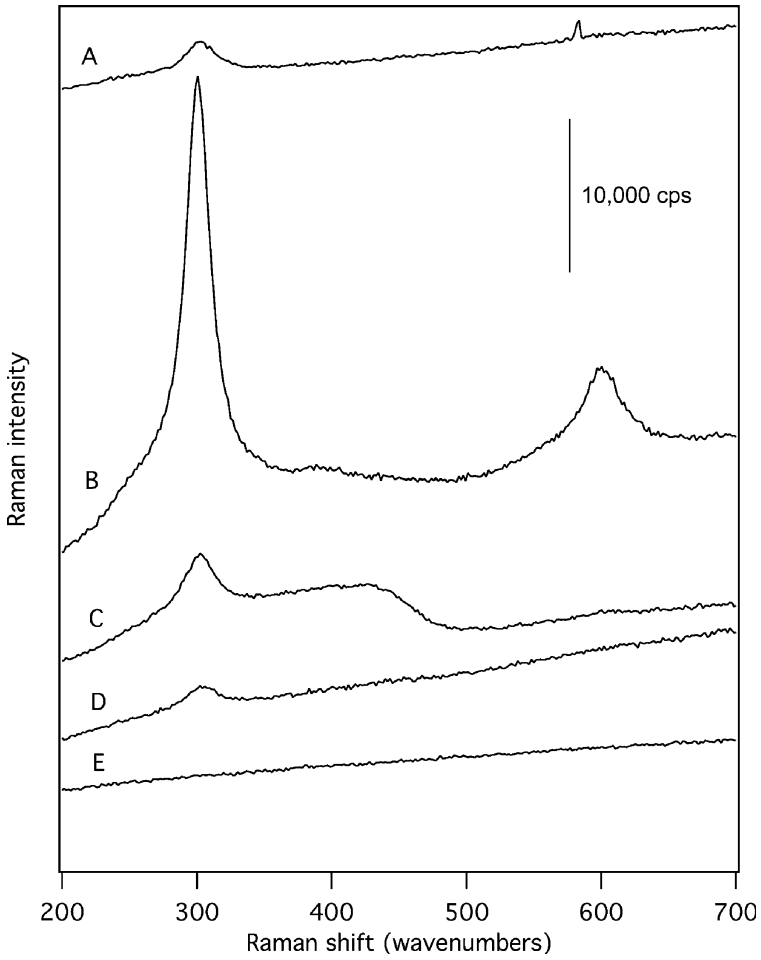

Figure 5.2 Representative resonance Raman spectra collected at various points along the bipolar electrode using a confocal microscope. The geometry of the analysis locations (for spectra A-E) is shown in Figure 5.1A.

As a further test of this hypothesis, we decided to perform a bipolar electrodeposition experiment in which the growth of CdS was kinetically controlled. To this end, we used a 10-fold higher concentration of Cd^{2+} (0.2 M) in the deposition electrolyte. An increase in $[Cd^{2+}]$ is expected to shift the Cd/Cd^{2+} formal potential ($E^{0'}$) anodically by about 30 mV. Since the predicted CdS deposition window is only on the order of about 100mV, the potential window for the deposition of stoichiometric CdS should dramatically narrow

under these experimental conditions. In addition, since mass transport of Cd^{2+} to the surface is the rate determining step at high overpotentials, increasing the concentration of Cd^{2+} is expected to increase the overall rate of electrodeposition[23]. Thus, CdS films formed at high [Cd^{2+}] should be less crystalline and contain more defects than films formed at lower Cd^{2+} concentrations. A decrease in the crystallinity of the electrodeposited CdS is expected to lead to broad phonon bands in the corresponding Raman spectra, while an increase in defect density is expected to lead to an increase in PL intensity at 420 cm^{-1}. Our hypothesis is clearly borne out by Raman/PL data collected on films grown under these conditions (Figure 5.3), as evidenced by both the broad LO phonon bands and the intense PL component in the spectra. In addition, the relative intensity of the PL feature increases at less cathodic overpotentials which favor the formation of a S-rich deposit.

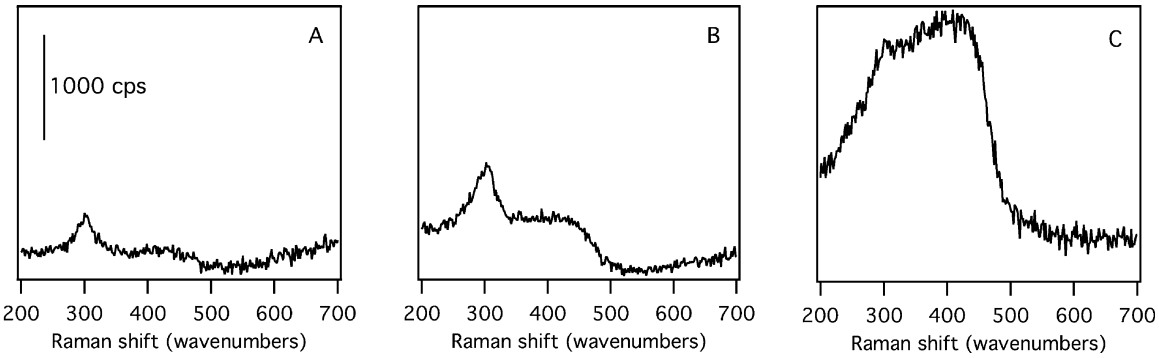

Figure 5.3 Representative resonance Raman spectra of CdS thin films deposited using bipolar electrochemistry when [Cd^{2+}] = 0.2 M. (A) Raman spectrum obtained near the cathodic pole of the BPE. (B) Spectrum obtained at the approximate center of the electrodeposit (between points A and C). (C) Raman spectrum obtained near the anodic limit of the electrodeposit. The large PL feature is characteristic of defects arising from a stoichiometric excess of S (see text for details).

5.4 Conclusions:

Bipolar electrodeposition of CdS chemical gradients has been demonstrated to occur in accordance with simple thermochemical principles. The variation of interfacial potential difference along the length of a conducting BPE allows the potential-dependent composition of electrodeposited CdS films to be displayed and screened using surface analytical techniques such as Raman microscopy and AES. In conclusion, using bipolar electrochemistry, solid-state material libraries can be deposited rapidly using extremely simple instrumentation. In addition, direct electrical contact with the substrate is not required. The exact nature of the faradaic half-reaction occurring at the anodic pole of the BPE is uncertain at this time. Investigations into this process are ongoing and will be reported in the near future.

References:

(1) Rajan, K. *Annu. Rev. Mater. Res.* **2008**, *38*, 299–322.

(2) Xiang, X. D.; Sun, X. D.; Briceno, G.; Lou, Y. L.; Wang, K. A.; Chang, H. Y.; Wallace-Freedman, W. G.; Chen, S. W.; Schultz, P. G. *Science* **1995**, *268*, 1738–1740.

(3) van Dover, R. B.; Schneemeyer, L. F.; Fleming, R. M. *Nature* **1998**, *392*, 162–164.

(4) Matsumoto, Y.; Murakami, M.; Shono, T.; Hasegawa, T.; Fukumura, T.; Kawasaki, M.; Ahmet, P.; Chikyow, T.; Koshihara, S.; Koinuma, H. *Science* **2001**, *291*, 854–856.

(5) Danielson, E.; Devenney, M.; Giaquinta, D. M.; Golden, J. H.; Haushalter, R. C.; McFarland, E. W.; Poojary, D. M.; Reaves, C. M.; Weinberg, W. H.; Wu, X. D. *Science* **1998**, *279*, 837–839.

(6) Briceno, G.; Chang, H.; Sun, X.; Schultz, P. G.; Xiang, X.-D. *Science* **1995**, *270*, 273–275.

(7) Brocchini, S.; James, K.; Tangpasuthadol, V.; Kohn, J. *J. Am. Chem. Soc.* **1997**, *119*, 4553–4554.

(8) Reddington, E.; Sapienza, A.; Gurau, B.; Viswanathan, R.; Sarangapani, S.; Smotkin, E. S.; Mallouk, T. E. *Science* **1998**, *280*, 1735–1737.

(9) Picket, J. D. Electrochemical Reactor Design, 2nd ed.; Elsevier Scientific Publishing Co.: New York, **1979**; p 34.

(10) Ulrich, C.; Andersson, O.; Nyholm, L.; Bjorefors, F. *Anal. Chem.* **2009**, *81*, 453–459.

(11) Arora, A.; Eijkel, J. C. T.; Morf, W. E.; Manz, A. *Anal. Chem.* **2001**, *73*, 3282–3288.

(12) Chow, K.-F.; Mavr_e, F.; Crooks, R. M. *J. Am. Chem. Soc.* **2008**, *130*, 7544–7545.

(13) Duval, J. F. L.; van Leeuwen, H. P.; Cecilia, J.; Galceran, J. *J. Phys. Chem. B* **2003**, *107*, 6782–6800.

(14) Dhopeshwarkar, R.; Hlushkou, D.; Nguyen, M.; Tallarek, U.; Crooks, R. M. *J. Am. Chem. Soc.* **2008**, *130*, 10480–10481.

(15) Bradley, J.-C.; Chen, H.-M.; Crawford, J.; Eckert, J.; Ernazarova, K.; Kurzeja, T.; Lin, M.; McGee, M.; Nadler, W.; Stephens, S. G. *Nature* **1997**, *389* (6648), 268–271.

(16) Bradley, J.; Babu, S.; Ndungu, P. *Fullerenes, Nanotubes, Carbon Nanostruct.* **2005**, *13*, 227–237.

(17) Warakulwit, C.; Nguyen, T.; Majimel, J.; Delville, M.; Lapeyre, V.; Garrigue, P.; Ravaine, V.; Limtrakul, J.; Kuhn, A. *Nano Lett.* **2008**, *8*, 500–504.

(18) Coleman, B. D.; Finnegan, N.; Bohn, P. W. *Thin Solid Films* **2004**, *467*, 121–126.

(19) Levich, V. G. *Physicochemical Hydrodynamics*; Prentice-Hall: Englewood Cliffs, NJ, **1962**, p 507.

(20) Fleischmann, M.; Ghoroghchian, J.; Pons, S. *J. Phys. Chem.* **1985**, *89*, 5530–5536.

(21) Duval, J.; Mieke-Kleijn, J.; van Leeuwen, H. P. *J. Electroanal. Chem.* **2001**, *505*, 1–11.

(22) Panicker, M. P. R.; Knaster, M.; Kroger, F. A. *J. Electrochem. Soc.* **1978**, *125*, 566–572.

(23) Lincot, D. *Thin Solid Films* **2005**, *487*, 40–48.

(24) Xiao, Q.; Xiao, C. *Appl. Surf. Sci.* **2009**, *255*, 7111–7114.

Chapter 6

SUMMARY OF DISSERTATION

Dawson type polyoxometalates (POMs), excellent multi-electron, proton, and oxygen conducting nanometer scale stable inorganic molecules, were synthesized according to established procedures, characterized and applied for an oxygen reduction reaction (ORR). Results show that the redox properties and the substituted transition metals determine the electrocatalytic activity of the compounds towards oxygen reduction reaction.

As the next step, these transition metal substituted Dawson type POMs were adapted as part of a bimetallic catalyst system in which these POMs, dissolved in an acidic solution, get adsorbed onto a noble metal electrode surface which helps for O=O bond cleavage, the primary step in ORR, making the ORR process facile. The noble metal electrode will be good at the second step in ORR, which is reduction of cleaved oxygen atoms to water. Further studies in this field were directed towards immobilization of POMs along with noble metal nanoparticles on a substrate and testing their ORR kinetics for real world application.

Next the ORR activity of the AT-MWNT-Co-Dawson adduct were studied. 12 hr sonication treatment of AT-MWNT with Co-Dawson has doubled the kinetic current of the AT-MWNT, though Co-Dawson decomposed during the sonication with AT-MWNT.

Further studies are required to study the nature of the electrocatalyst formed during the sonication.

We have created a combinatorial material library on a single substrate by establishing a lateral potential gradient using a bipolar technique. In this technique, a required voltage is applied between two driver electrodes kept in an electrolyte of specified ionic strength where the applied voltage makes a gradual change in the solution potential with respect to the position between the driver electrodes. This helps to generate an electrode potential gradient on a floating conducting body between the two driver electrodes. This lateral potential gradient can be utilized to deposit materials with varying properties depending upon the deposition potential. We illustrated this concept using a CdS binary system. Application of bipolar in material library synthesis can be extended to ternary systems. Not only semiconductors, but also alloys, can be deposited on a single bipolar electrode with varying composition using the lateral potential gradient. The bipolar concept has also been applied in sensors. A detailed study on the potential distribution on the bipolar electrode as a function of various operating conditions such as applied voltage between the driver electrodes, distance between the driver electrodes, and ionic strength of the electrolyte would provide a better understanding of the bipolar electrode processes. It will lead to efficient and effective utilization of bipolar concept for material library synthesis and sensor applications.